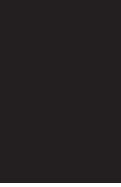


Millimeter-Wave Wireless Communication Systems: Theory and Applications

Guest Editors: Chia-Chin Chong, Kiyoshi Hamaguchi,
Peter F. M. Smulders, and Su-Khiong Yong





Millimeter-Wave Wireless Communication Systems: Theory and Applications

EURASIP Journal on
Wireless Communications and Networking

Millimeter-Wave Wireless Communication Systems: Theory and Applications

Guest Editors: Chia-Chin Chong, Kiyoshi Hamaguchi,
Peter F. M. Smulders, and Su-Khiong Yong



Copyright © 2007 Hindawi Publishing Corporation. All rights reserved.

This is a special issue published in volume 2007 of "EURASIP Journal on Wireless Communications and Networking." All articles are open access articles distributed under the Creative Commons Attribution License, which permits unrestricted use, distribution, and reproduction in any medium, provided the original work is properly cited.

Editor-in-Chief

Phillip Regalia, Institut National des Télécommunications, France

Associate Editors

Thushara Abhayapala, Australia
Mohamed H. Ahmed, Canada
Farid Ahmed, USA
Alagan Anpalagan, Canada
Anthony Boucouvalas, Greece
Lin Cai, Canada
Biao Chen, USA
Pascal Chevalier, France
Chia-Chin Chong, USA
Huaiyu Dai, USA
Soura Dasgupta, USA
Ibrahim Develi, Turkey
Petar Djuric, USA
Mischa Dohler, France
Abraham O. Fapojuwo, Canada
Michael Gastpar, USA
Alex Gershman, Germany
Wolfgang Gerstacker, Germany
David Gesbert, France

Fary Z. Ghassemlooy, UK
Christian Hartmann, Germany
Stefan Kaiser, Germany
G. K. Karagiannidis, Greece
Hyung-Myung Kim, Korea
C. C. Ko, Singapore
Visa Koivunen, Finland
Richard Kozick, USA
Bhaskar Krishnamachari, USA
S. Lambotharan, UK
Vincent Lau, Hong Kong
David I. Laurenson, UK
Tho Le-Ngoc, Canada
Wei Li, USA
Yonghui Li, Australia
Tongtong Li, USA
Zhiqiang Liu, USA
Stephen McLaughlin, UK
Sudip Misra, Canada

Marc Moonen, Belgium
Eric Moulines, France
Sayandev Mukherjee, USA
A. Nallanathan, Singapore
Kameswara Rao Namuduri, USA
A. Pandharipande, The Netherlands
Athina Petropulu, USA
Brian Sadler, USA
Ivan Stojmenovic, Canada
Lee Swindlehurst, USA
Sergios Theodoridis, Greece
Lang Tong, USA
Luc Vandendorpe, Belgium
Athanasios V. Vasilakos, Greece
Yang Xiao, USA
Xueshi Yang, USA
Lawrence Yeung, Hong Kong
Dongmei Zhao, Canada
Weihua Zhuang, Canada

Contents

Millimeter-Wave Wireless Communication Systems: Theory and Applications, Chia-Chin Chong, Kiyoshi Hamaguchi, Peter F. M. Smulders, and Su-Khiong Yong
Volume 2007, Article ID 72831, 2 pages

An Overview of Multigigabit Wireless through Millimeter Wave Technology: Potentials and Technical Challenges, Su Khiong Yong and Chia-Chin Chong
Volume 2007, Article ID 78907, 10 pages

60-GHz Millimeter-Wave Radio: Principle, Technology, and New Results, Nan Guo, Robert C. Qiu, Shaomin S. Mo, and Kazuaki Takahashi
Volume 2007, Article ID 68253, 8 pages

60 GHz Indoor Propagation Studies for Wireless Communications Based on a Ray-Tracing Method, C.-P. Lim, M. Lee, R. J. Burkholder, J. L. Volakis, and R. J. Marhefka
Volume 2007, Article ID 73928, 6 pages

Channel Characteristics and Transmission Performance for Various Channel Configurations at 60 GHz, Haibing Yang, Peter F. M. Smulders, and Matti H. A. J. Herben
Volume 2007, Article ID 19613, 15 pages

Rain Attenuation at 58 GHz: Prediction versus Long-Term Trial Results, Vaclav Kvicera and Martin Grabner
Volume 2007, Article ID 46083, 7 pages

Rain-Induced Bistatic Scattering at 60 GHz, Henry T. van der Zanden, Robert J. Watson, and Matti H. A. J. Herben
Volume 2007, Article ID 53203, 5 pages

Comparison of OQPSK and CPM for Communications at 60 GHz with a Nonideal Front End, Jimmy Nsenga, Wim Van Thillo, François Horlin, André Bourdoux, and Rudy Lauwereins
Volume 2007, Article ID 86206, 14 pages

Direct Conversion EHM Transceivers Design for Millimeter-Wave Wireless Applications, Abbas Mohammadi, Farnaz Shayegh, Abdolali Abdipour, and Rashid Mirzavand
Volume 2007, Article ID 32807, 9 pages

V-Band Multiport Heterodyne Receiver for High-Speed Communication Systems, Serioja O. Tatu and Emilia Moldovan
Volume 2007, Article ID 34358, 7 pages

Editorial

Millimeter-Wave Wireless Communication Systems: Theory and Applications

Chia-Chin Chong,¹ Kiyoshi Hamaguchi,² Peter F. M. Smulders,³ and Su-Khiong Yong⁴

¹DoCoMo USA Labs, 3240 Hillview Avenue, Palo Alto, CA 94304, USA

²National Institute of Information and Communications Technology (NICT), Yokosuka-shi 239-0847, Japan

³Eindhoven University of Technology, P.O. Box 513, 5600 MB Eindhoven, The Netherlands

⁴Savi Technology, A Lockheed Martin Company, 351 E. Evelyn Avenue, Mountain View, CA 94041, USA

Received 5 April 2007; Accepted 5 April 2007

Copyright © 2007 Chia-Chin Chong et al. This is an open access article distributed under the Creative Commons Attribution License, which permits unrestricted use, distribution, and reproduction in any medium, provided the original work is properly cited.

Recently, millimeter-wave radio has attracted a great deal of interest from academia, industry, and global standardization bodies due to a number of attractive features of millimeter-wave to provide multi-gigabit transmission rate. This enables many new applications such as high definition multimedia interface (HDMI) cable replacement for uncompressed video or audio streaming and multi-gigabit file transferring, all of which intended to provide better quality and user experience. Despite of unique capability of millimeter-wave technology to offer such a high data rate demand, a number of technical challenges need to be overcome or well understood before its full deployment. This special issue is aimed to provide a more thorough understanding of millimeter-wave technology and can be divided into three parts. The first part presents the recent status and development of millimeter-wave technology and the second part discusses various types of propagation channel models. Finally, the last part of this special issue presents some technical challenges with respect to suitable millimeter-wave air interface and highlights some related implementation issues.

In the first paper by S.-K. Yong and C.-C. Chong, the authors provide a generic overview of the current status of the millimeter wave radio technology. In particular, the potential and limitations of this new technology in order to support the multi-gigabit wireless application are discussed. The authors envisioned that the 60 GHz radio will be one of the important candidates for the next generation wireless systems. This paper also included a link budget study that highlights the crucial role of antennas in establishing a reliable communication link.

The second paper by N. Guo et al. extends the overview discussion of the first paper by summarizing some recent

works in the area of 60 GHz radio system design. Some new simulation results are being reported which shown the impact of the phase noise on the bit-error rate (BER). The authors concluded that phase noise is a very important factor when considering multi-gigabit wireless transmission and has to be taken into account seriously.

In the third paper by C.-P. Lim et al. the authors propose a 60 GHz indoor propagation channel model based on the ray-tracing method. The model is validated with measurements conducted in indoor environment. Important parameters such as root mean square (RMS) delay spread and the fading statistics in order to characterize the behavior of the millimeter-wave multipath propagation channel are extracted from the measurement database. This ray-tracing model is particularly important in characterizing the multipath channel behavior of various types of indoor environments, which are the typical application scenarios for 60 GHz technology.

The fourth paper by H. Yang et al. uses a different modeling approaches in characterizing the 60 GHz propagation channel. In this paper, a statistical-based channel model is proposed based on the extensive measurements campaign conducted in indoor office environment. Based on this, a single-cluster power delay profile (PDP) is found to best characterize the channel statistics in which the PDP can be parameterized by K-factor, RMS delay spread, and shape parameter under both line-of-sight (LOS) and non-LOS (NLOS) conditions. Various types of antenna beam patterns such as omnidirectional, fan-beam and pencil-beam, and their directivities are being investigated at both the transmitter and receiver sides. Finally, in order to analyze the effect of multipath channel on system design, an OFDM-based

system is used to compare the BER performance of both measured and modeled channels. The authors conclude that the directive configurations can provide additional link margins and improved BER performance for multi-gigabit transmissions using the 60 GHz radio technology.

The fifth paper by V. Kvicera and M. Grabner investigated the effect of rain attenuation at 58 GHz based on the large measurement results collected over a 5-year period. The measurement results obtained were analyzed and compared to the ITU-R recommendations which are valid for estimating long-term statistics of rain attenuation for frequency up to 40 GHz. The results reported are important as an extension to the ITU-R recommendations for realistic link-level analysis especially for point-to-point fixed system up to 60 GHz.

In the context of the wide deployment of 60 GHz links, the sixth paper by H. T. van der Zanden et al. addresses the modeling and prediction of rain-induced bistatic scattering at 60 GHz. This factor is important as it could cause link interference between nearby 60 GHz links when rain falls. The paper shows that despite of the high oxygen attenuation, coupling between adjacent links caused by bistatic scattering could be significant even in light rain.

The seventh paper by J. Nsenga et al. is related to the baseband system design in which two new modulation schemes, firstly, offset quadrature phase shift keying (OQPSK) with frequency domain equalization (FDE), and secondly, constant phase modulation (CPM) with time domain equalization. Both techniques are targeted for low-cost and low-power 60 GHz communications systems and are evaluated and compared by considering the effects of front end non-ideality. The authors found that OQPSK with FDE and non-fractional sampling minimum mean square error (MMSE) receiver yields best tradeoffs between BER performance and system complexity study in terms of analog-digital-converter (ADC) clipping and quantization effect, phase noise effect, as well as power amplifier nonlinearity effect.

In the eighth paper, by A. Mohammadi et al. a direct conversion modulator-demodulator for fixed wireless applications is proposed. The circuits consist of even harmonic mixers (EHMs) realized with antiparallel diode pairs (APDPs), where self-biased APDP is used in order to flatten the conversion loss of the system versus local oscillator (LO) power. The impacts of I/Q imbalances and DC offsets on BER performance of the system is also being considered. A communication link is built with the proposed modulator-demodulator and the experimental results shown that such a system can be a low-cost and high-performance 16-QAM transceiver especially for the local multipoint distribution system (LMDS) applications.

The last paper by S. O. Tatu and E. Moldovan proposed a practical circuit for the 60 GHz radio. In this paper, a V-band receiver using an MHMIC multipoint circuit is proposed. It was demonstrated that the combination of multipoint circuit with power detectors and two differential amplifiers can replace the conventional mixer in a low-cost heterodyne or homodyne architecture. The operating principle of the proposed heterodyne receiver and demodulation results of

high-speed MPSK/QAM signals are also discussed. Simulation results in the paper shown that an improved overall gain can be obtained. The authors concluded that such a multipoint heterodyne architecture can enable the compact and low-cost millimeter-wave receivers for the future wireless communications systems such as the IEEE 802.15.3c wireless personal area networks (WPAN) applications.

Chia-Chin Chong
Kiyoshi Hamaguchi
Peter F. M. Smulders
Su-Khiong Yong

Research Article

An Overview of Multigigabit Wireless through Millimeter Wave Technology: Potentials and Technical Challenges

Su Khiong Yong¹ and Chia-Chin Chong²

¹ *Communication and Wireless Connectivity Laboratory, Samsung Advanced Institute of Technology, P.O. Box 111, Suwon 440-600, South Korea*

² *NTT DoCoMo USA Labs, 3240 Hillview Avenue, Palo Alto, CA 94304, USA*

Received 14 June 2006; Revised 11 September 2006; Accepted 14 September 2006

Recommended by Peter F. M. Smulders

This paper presents an overview of 60 GHz technology and its potentials to provide next generation multigigabit wireless communications systems. We begin by reviewing the state-of-art of the 60 GHz radio. Then, the current status of worldwide regulatory efforts and standardization activities for 60 GHz band is summarized. As a result of the worldwide unlicensed 60 GHz band allocation, a number of key applications can be identified using millimeter-wave technology. Despite of its huge potentials to achieve multigigabit wireless communications, 60 GHz radio presents a series of technical challenges that needs to be resolved before its full deployment. Specifically, we will focus on the link budget analysis from the 60 GHz radio propagation standpoint and highlight the roles of antennas in establishing a reliable 60 GHz radio.

Copyright © 2007 S. K. Yong and C.-C. Chong. This is an open access article distributed under the Creative Commons Attribution License, which permits unrestricted use, distribution, and reproduction in any medium, provided the original work is properly cited.

1. INTRODUCTION

Despite millimeter wave (mmWave) technology has been known for many decades, the mmWave systems have mainly been deployed for military applications. With the advances of process technologies and low-cost integration solutions, mmWave technology has started to gain a great deal of momentum from academia, industry, and standardization body. In a very broad term, mmWave can be classified as electromagnetic spectrum that spans between 30 GHz to 300 GHz, which corresponds to wavelengths from 10 mm to 1 mm [1]. In this paper, however, we will focus specifically on 60 GHz radio (unless otherwise specified, the terms 60 GHz and mmWave can be used interchangeably), which has emerged as one of the most promising candidates for multigigabit wireless indoor communication systems [2]. 60 GHz technology offers various advantages over current or existing communications systems [3]. One of the deciding factors that makes 60 GHz technology gaining significant interest recently is due to the huge unlicensed bandwidth (up to 7 GHz) available worldwide. While this is comparable to the unlicensed bandwidth allocated for ultra wideband (UWB) purposes [4], 60 GHz bandwidth is continuous and less restricted in terms of power limits. This is due to the fact

that UWB system is an overlay system and thus subject to very strict and different regulations [5]. The large bandwidth at 60 GHz band is one of the largest unlicensed bandwidths being allocated in history. This huge bandwidth represents high potentials in terms of capacity and flexibility that makes 60 GHz technology particularly attractive for gigabit wireless applications. Furthermore, 60 GHz regulation allows much higher transmit power compared to other existing wireless local area networks (WLANs) and wireless personal area networks (WPANs) systems. The higher transmit power is necessary to overcome the higher path loss at 60 GHz. While the high path loss seems to be disadvantage at 60 GHz, it however confines the 60 GHz operation to within a room in an indoor environment. Hence, the effective interference levels for 60 GHz are less severe than those systems located in the congested 2–2.5 GHz and 5–5.8 GHz regions. In addition, higher frequency reuse can also be achieved per indoor environment thus allowing a very high throughput network. The compact size of the 60 GHz radio also permits multiple antennas solutions at the user terminal that are otherwise difficult, if not impossible, at lower frequencies. Comparing to 5 GHz system, the form factor of mmWave systems is approximately 140 times smaller and can be conveniently integrated into consumer electronic products.

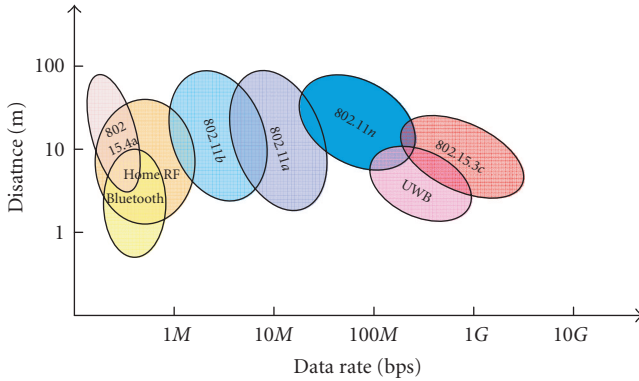


FIGURE 1: Data rates and range requirements for WLAN and WPAN standards and applications. Millimeter wave technology, that is, IEEE 802.15.3c is aiming for very high data rates.

Despite the various advantages offered, mmWave based communications suffer a number of critical problems that must be resolved. Figure 1 shows the data rates and range requirements for number of WLAN and WPAN systems. Since there is a need to distinguish between different standards for broader market exploitation, the IEEE 802.15.3c is positioned to provide gigabit rates and longer operating range. At these rate and range, it will be a nontrivial task for mmWave systems to provide sufficient power margin to ensure reliable communication link. Furthermore, delay spread of the channel under study is another limiting factor for high speed transmissions. Large delay spread values can easily increase the complexity of the system beyond the practical limit for equalization.

The remainder of the paper is organized as follows: Section 2 describes the worldwide regulatory efforts and standardization activities; Section 3 presents a number of application scenarios and highlights the requirements for a specific application namely uncompressed high definition video streaming; Section 4 analyses the achievable data rate in both additive white Gaussian noise (AWGN) and fading channel based on the application requirements described in Section 3 and the roles of antenna in 60 GHz communications are also discussed; Section 5 describes the technical challenges that need to be resolved ahead for the full deployment of 60 GHz radio; finally, in Section 6 appropriate conclusions wrap up this paper.

2. WORLDWIDE REGULATIONS AND STANDARDIZATION

This section discusses the current status of worldwide regulation and standardization efforts for 60 GHz band. Regulatory body in United States, Japan, Canada, and Australia have already set frequency bands and regulations for 60 GHz operation while in Korea and Europe intense efforts are currently underway. A summary for the issued and proposed frequency allocations and main specifications for radio regulation in a number of countries is given in Table 1.

2.1. 60 GHz regulations in North America

In 2001, the United States Federal Communication Commissions (FCC) allocated 7 GHz in the 54–66 GHz band for unlicensed use [6]. In terms of the power limits, FCC rules allow emission with average power density of $9 \mu\text{W}/\text{cm}^2$ at 3 meters and maximum power density of $18 \mu\text{W}/\text{cm}^2$ at 3 meters, from the radiating source. These figures translate to average equivalent isotropic radiated power (EIRP) and maximum EIRP of 40 dBm and 43 dBm, respectively. FCC also specified the total maximum transmit power of 500 mW for an emission bandwidth greater than 100 MHz.

The devices must also comply with the radio frequency (RF) radiation exposure requirements specified in [6, Sections 1.307(b), 2.1091, and 2.1093]. After taking the RF safety issues into account, the maximum transmit power is limited to 10 dBm. Furthermore, each transmitter must transmit at least one transmitter identification within one-second interval of the signal transmission. It is important to note that the 60 GHz regulation in Canada, which is regulated by Industry Canada Spectrum Management and Telecommunications (IC-SMT) [7], is harmonized with the US.

2.2. 60 GHz regulations in Japan

In year 2000, the Ministry of Public Management, Home Affairs, Posts, and Telecommunications (MPHPT) of Japan issued 60 GHz radio regulations for unlicensed utilization in the 59–66 GHz band [8]. The 54.25–59 GHz band is however allocated for licensed use. The maximum transmit power for the unlicensed use is limited to 10 dBm with maximum allowable antenna gain of 47 dBi. Unlike in North America, Japanese regulations specified that the maximum transmission bandwidth must not exceed 2.5 GHz. There is no specification for RF radiation exposure and transmitter identification requirements.

2.3. 60 GHz regulation in Australia

Following the release of regulations in Japan and North America, the Australian Communications and Media Authority (ACMA) has taken a similar step to regulate 60 GHz band [9]. However, only 3.5 GHz bandwidth is allocated for unlicensed use, that is, from 59.4–62.9 GHz. The maximum transmit power and maximum EIRP are limited to 10 dBm and 51.7 dBm, respectively. The data communication transmitters that operate in this frequency band are limited to land and maritime deployments.

2.4. 60 GHz regulation in Korea

In June 2005, mmWave Frequency Study Group (MFSG) was formed under the Korean Radio Promotion Association [12]. The MFSG has recommended a 7 GHz unlicensed spectrum from 57–64 GHz without limitation on the types of application to be used. The maximum transmit power is the same as in Japan and Australia, that is, 10 dBm but the maximum allowable antenna gain is still under discussion. Currently, the

TABLE 1: Frequency band plan and limits on transmit power, EIRP, and antenna gain for various countries.

Region	Unlicensed bandwidth (GHz)	Tx Power	EIRP	Max. Antenna gain	Ref	Comment
USA	7 GHz (57–64)	500 mW (max)*	40 dBm (ave)* 43 dBm (max)#	NS	[6]	* For bandwidth > 100 MHz + Translate from average PD of 9 uW/cm ² at 3 m # Translate from average PD of 18 uW/cm ² at 3 m
Canada	7 GHz (57–64)	500 mW (max)*	40 dBm (ave)* 43 dBm (max)#	NS	[7]	* For bandwidth > 100 MHz + Translate from average PD of 9 uW/cm ² at 3 m # Translate from average PD of 18 uW/cm ² at 3 m
Japan	7 GHz (59–66), max 2.5 GHz	10 mW (max)	NS	47 dBi	[8]	
Australia	3.5 GHz (59.4–62.9)	10 mW (max)	150 W (max)	NS	[9]	Limited to land and maritime deployment
Korea	7 GHz (57–64)	10 mW (max)	TBD	TBD	[10]	Frequency allocation expected in Jun, 06 Radio regulation expected by End of 06
Europe	9 GHz (57–66), min 500 MHz	20 mW (max)	57 dBm (max)	37 dBi	[11]	Recommendation by ETSI

60 GHz regulation efforts in Korea are in the final stage of public hearing forum [10] in which the frequency band allocation is expected to take place in June 2006. The final radio regulation is scheduled to be completed by December 2006.

2.5. 60 GHz regulation in Europe

The European Telecommunications Standards Institute (ETSI) and European Conference of Postal and Telecommunications Administrations (CEPT) have been working closely to establish a legal framework for the deployment of unlicensed 60 GHz devices. In general, 59–66 GHz band has been allocated for mobile services without specific decision on the regulations. The CEPT Recommendation T/R 22–03 has provisionally recommended the use of 54.25–66 GHz band for terrestrial and fixed mobile systems [13]. However, this provisional allocation has been recently withdrawn.

The European Radiocommunication Committee (ERC) considered the use of 57–59 GHz band for fixed services without requiring frequency planning [14]. Later, the Electronic Communications Committee (ECC) within CEPT recommended the use of point-to-point fixed services in the 64–66 GHz band [15]. In the most recent development, ETSI proposed 60 GHz regulations to be considered by ECC for WPAN applications [11]. Under this proposal, 9 GHz unlicensed spectrum is allocated for 60 GHz operation. This band represents the union of the bands currently

approved and under proposed as described from Section 2.1 to Section 2.4. In addition, a minimum spectrum of 500 MHz is required for the transmitted signal with maximum EIRP of 57 dBm. No specification is given for the maximum transmit power and maximum antenna gain. This proposal is expected to be submitted to ECC by September 2006 and ETSI would request ECC to finalize the new deliverable proposal by the end of 2006.

2.6. Industrial standardization efforts

The first international industry standard that covers 60 GHz band is the IEEE 802.16 Standard for local and metropolitan area networks [16]. However, this is a licensed band and is used for line-of-sight (LOS) outdoor communications for last mile connectivity. In Japan, two standards related to 60 GHz band were issued by Association of Radio Industries and Business (ARIB), that is, the ARIB-STD T69 [17] and ARIB-STD T74 [18]. The former is the standard for mmWave video transmission equipment for specified low-power radio station (point-to-point system), while the latter is the standard for mmWave ultra high-speed WLAN for specified low-power radio station (point-to-multipoint). Both standards cover the 59–66 GHz band defined in Japan.

The interest in 60 GHz radio continued to grow with the formation on mmWave Interest Group and Study Group within the IEEE 802.15 Working Group for WPAN. In March

2005, the IEEE 802.15.3c Task Group (TG3c) was formed to develop an mmWave-based alternative physical layer (PHY) for the existing IEEE 802.15.3 WPAN Standard 802.15.3-2003 [2]. The developed PHY is aimed to support minimum data rate of 2 Gbps over few meters with optional data rates in excess of 3 Gbps. This is the first standard that addresses multigigabit wireless systems and will form the key solutions to many data rates starving applications especially related wireless multimedia distribution.

In other development, WiMedia Alliance has recently announced the formation of WiMedia 60 GHz Study Group with the aim to provide recommendations to the WiMedia Board of Directors on the feasibility issues related to 60 GHz technology. Decision will be taken in the near future about WiMedia direction and involvement in 60 GHz market [19].

3. APPLICATION SCENARIOS

With the allocated bandwidth of 7 GHz in most countries, mmWave radio has become the technology enabler for many gigabit transmission applications that are technically constrained at lower frequency. Due to the higher path loss and oxygen absorption of 15 dB/km around 60 GHz band, 60 GHz radio is thus limited for indoor applications. A number of applications are envisioned such as high definition multimedia interface (HDMI) cable replacement/uncompressed high definition (HD) video streaming, mobile distributed computing, wireless docking station, wireless gigabit Ethernet, fast bulky file transfer, wireless gaming, and so forth. However, as shown in the IEEE 802.15.3c meeting in Jacksonville, FL, USA, TG3c envisaged the wireless HD streaming is the most attractive application among the others [20]. We will therefore concentrate on this particular application scenario and describe the technical requirements for its operation.

Depending on the progressive scan resolution and number of pixels per line, the data rates required varies from several hundreds Mbps to few Gbps. The latest commercially available high definition television (HDTV) resolution is 1920×1080 with refresh rate of 60 Hz. Considering RGB video formats with 8 bits per channel per pixel, the required data rates turns out to be approximately 3 Gbps. In the future, a higher number of bits per channel as well as higher refresh rates are expected to improve the quality of next generation HDTV. This easily scales the data rate to well beyond 5 Gbps. Table 2 summarizes data rates requirements for some current and future HDTV specifications. Furthermore, uncompressed HD streaming is an asymmetry transmission with significantly different data flow in both uplink and downlink directions. This application also requires very low latency of tens of microseconds and very low error probability down to 10^{-12} to ensure high quality video. Table 3 recapitulates the key requirements for uncompressed HD video streaming as well as outlines the large scale parameters for home environment and conference room within an office environment [21], which this application is mainly deployed.

TABLE 2: Data rate requirements for different resolutions, frame rates, and numbers of bits per channel per pixel for HDTV standard.

Pixels per line	Active lines per picture	Frame rate	# of bits per channel per pixel	Data rate (Gbps)
1280	720	24	24	0.531
1280	720	30	24	0.664
1440	480	60	24	0.995
1280	720	50	24	1.106
1280	720	60	24	1.327
1920	1080	50	24	2.488
1920	1080	60	24	2.986
1920	1080	60	30	3.732
1920	1080	60	36	4.479
1920	1080	60	42	5.225
1920	1080	90	24	4.479
1920	1080	90	30	5.599

4. FEASIBILITY STUDY

In this section, we perform a basic feasibility study on the 60 GHz radio technology. The study is based on the application scenarios described in Section 3 for the uncompressed HD video streaming. We begin by analyzing the achievable Shannon capacity for an omni-directional antenna at both sides of the transmitter (Tx) and receiver (Rx). Then, we determine what is the minimum gain required in order to operate under certain environment and target specifications. The analysis also considers the effect of multipath and investigates the role of antenna to provide sufficient power margin for 60 GHz wireless communications. Unless otherwise specified, the parameters in Table 4 are assumed in our analysis.

4.1. Power margin

Using the above parameters, one can compute the ratio of signal power to noise power at the Rx as given by

$$\text{SNR} = P_T + G_T + G_R - PL_0 - PL(d) - I_L - (KT + 10 \log_{10}(B) - NF), \quad (1)$$

where G_T and G_R denote the transmit and received antenna gain, respectively. Inserting (1) into the well-known Shannon capacity formula, that is, $C = B \log_2(\text{SNR} + 1)$, the maximum achievable capacity in AWGN can be computed. Figure 2 shows the Shannon capacity limit for indoor office in LOS and non-LOS (NLOS) case using omni-omni antenna setup. It can be observed that for LOS condition, a 5 Gbps data rates is impossible at any distance. On the other hand, the operating distance for NLOS condition is limited to below 3 m though the capacity for NLOS decreases more drastically as a function of distance. To improve the capacity for a given operating distance, one can either increase the bandwidth or signal-to-noise ratio (SNR) or both. It can also be seen from Figure 2 that increasing the bandwidth used by more than 4 times only significantly improves the capacity for distance below 5 m. Beyond this distance, the capacity for the 7 GHz case only slightly above the case of 1.5 GHz bandwidth, since

TABLE 3: Key requirements for uncompressed HD video streaming application and the large scale fading parameters for conference room and home environment, respectively.

Applications	Data Rate	BER	Data type	Environment	n	Shadowing	Ref
Uncompressed HD video streaming	0.05–5.5 Gbps	1.00E-12	Isochronous	Home 5–10 m (LOS/NLOS)	1.55/2.44	1.5/6.2	[22]
				Conf. room 20 m (LOS/NLOS)	1.77/3.83	6/7.6	[23]

TABLE 4: Parameters used in the analysis.

Tx Power, P_T	10 dBm
Center frequency, f_c	60 GHz
Noise figure, NF	6 dB
Implementation loss, IL	6 dB
Thermal noise, N	174 dBm/MHz
Bandwidth, B	1.5 GHz
Distance	20 m
Path loss at 1 m, PL_0	57.5 dB

the SNR at the Rx is reduced considerably at longer distance due to higher path loss. On the other hand, the overall capacity over the considered distance increases notably if a 10 dBi transmit antenna gain is employed as compared to the omnidirectional antenna for both 1.5 GHz and 7 GHz bandwidths. This clearly shows the importance of antenna gain in providing a very high data application at 60 GHz which is not possible to be provided with omnidirectional antenna configuration. But the question remains, how much gain is required?

To answer that question, the capacity as a function of combined Tx and Rx gain for operating distance at 20 m is plotted as depicted in Figure 3. To achieve 5 Gbps at 20 m, a combined gain of 25 dBi and 37 dBi are required for LOS and NLOS, respectively. This seems to be practical value since it is a combined Tx and Rx gain. However, to achieve the same data rates in multipath channel, higher gain is needed to overcome the fading margin. Now consider what additional gains are required in a more realistic scenario where the propagation channel is corrupted by multipath fading instead of AWGN. To ease the analysis, we use the closed-form bit error probability (BEP) results for the noncoherent binary frequency-shift keying (BFSK) [22]. Specifically, we use

$$P_b = \frac{1 + K}{2 + 2K + \bar{\gamma}_b} \exp\left(-\frac{K\bar{\gamma}_b}{2 + 2K + \bar{\gamma}_b}\right), \quad (2)$$

where K and $\bar{\gamma}_b$ are the Ricean K -factor and the average energy-per-bit-to-noise ratio, respectively. Equation (2) can be reduced to the case of Rayleigh fading when $K = 0$ and simultaneously approximates the AWGN case when $K \rightarrow \infty$.

Clearly from Figure 4, one can see that for uncoded system, the required additional combined Tx-Rx gain becomes prohibitively impractical in order to achieve BEP of 10^{-12} in Ricean and Rayleigh fading channels, respectively, over the AWGN case. Thus, coded systems, diversity systems or/and

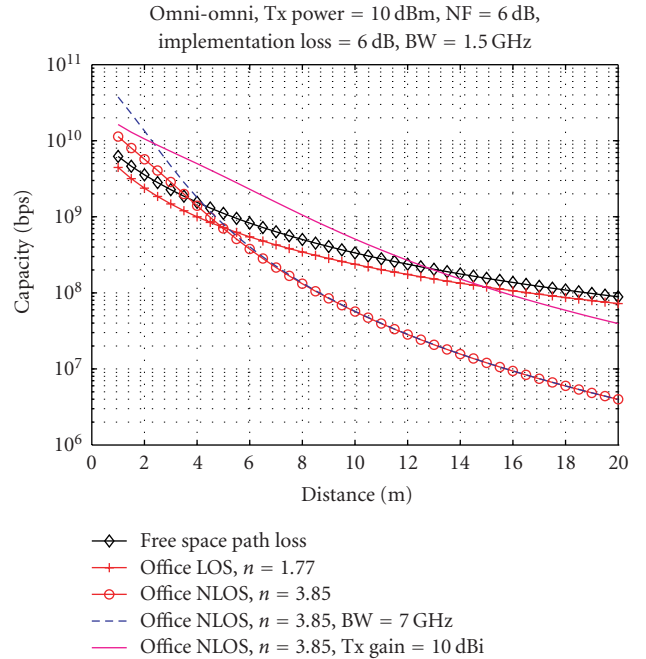


FIGURE 2: Shannon capacity limits for the case of indoor office using omnidirectional antenna setup.

high gain antenna systems have to be used in order to reduce the fading margin associated with the multipath channel. For diversity technique employing maximum ratio combining in a flat Rayleigh fading channel, the BEP for uncoded BFSK can be expressed as [22]

$$P_b = \left[\frac{1}{2}(1 - \mu)\right]^L \sum_{k=0}^{L-1} \binom{L-1+k}{k} \left[\frac{1}{2}(1 + \mu)\right]^k, \quad (3)$$

where L is the number of diversity channels that are assumed to be statistically independent Rayleigh fading and μ is given as

$$\mu = \frac{\bar{\gamma}_c}{\bar{\gamma}_c + 2}, \quad (4)$$

where $\bar{\gamma}_c$ is the average SNR per channel. As shown in Figure 4, the use of diversity technique for the case of two and four channels provides diversity gain of approximately 65 dB to 80 dB over the single channel at BEP of 10^{-12} . However, in

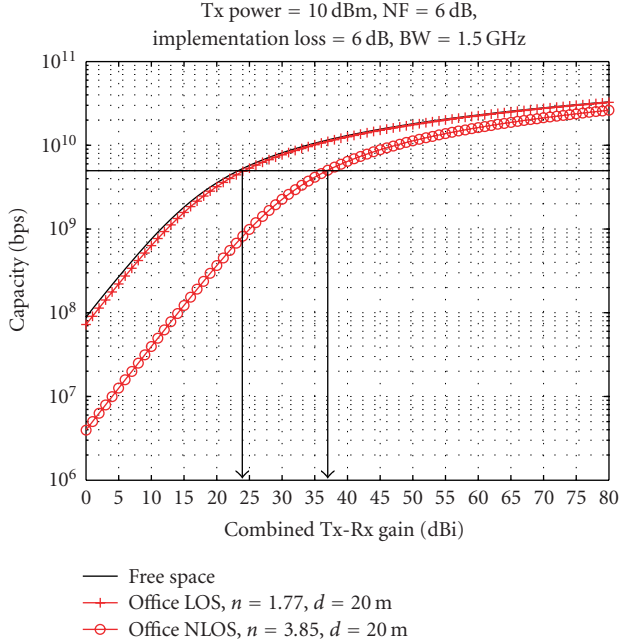


FIGURE 3: The required combined Tx-Rx antenna gain to achieve a target capacity.

practice these gains are expected to be much lower as channel is not independent and identical distributed and subject to fading correlation. Similarly, the use of channel coding can improve the BEP significantly over the uncoded case. In our example, the use of Golay (24,12) code (with Hamming distance $d_{\min} = 8$) is shown to have coding gain of approximately 92 dB over the single channel Rayleigh fading case.

For the cases discussed above, to achieve 5 Gbps data rate at BEP of 10^{-12} , in the case of Rayleigh fading channel and assuming that bandwidth is equal to the data rate, one can compute the power margin as the difference between the received E_b/N_0 over the required E_b/N_0 to achieve the target BEP. The power margin for the case of Rayleigh channel with coding and diversity as well as AWGN can be shown to be given by

$$\begin{aligned} M_{\text{Ray_Coded}} &= G_T + G_R - 61, \\ M_{\text{Ray_Div}} &= G_T + G_R - 73, \\ M_{\text{AWGN}} &= G_T + G_R - 37. \end{aligned} \quad (5)$$

For high quality video transmission link at 60 GHz, a sufficiently large link margin is required due to the highly variable shadowing and human blockage effects. Experiments show that the shadowing effect is log-normally distributed with zero mean and standard deviation as high as 7–10 dB [23, 24]. On the other hand, the effect of human blockage varies between 18–36 dB [25, 26]. Assuming a margin of 10 dB is required, then the required combined Tx-Rx gain for the three cases given in (5) are 71 dB, 83 dB, and 47 dB, respectively. From the regulatory standpoint, we see that the maximum transmit antenna gain that is allowed for a Tx

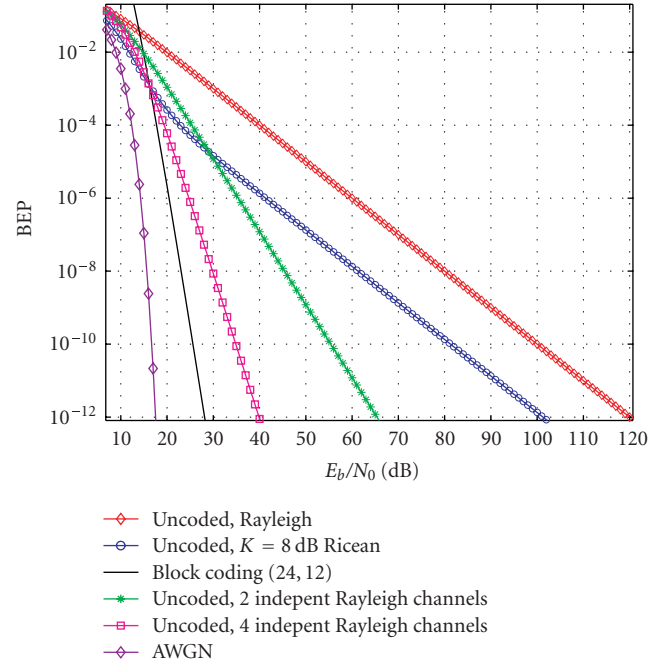


FIGURE 4: The BEP for the case of uncoded, coded, and diversity systems in Rayleigh fading channel.

power of 10 dBm is 33 dBi. This sets the Rx gain to be very high, namely, 38 dBi, 50 dBi, and 14 dBi, respectively, for the three cases considered above.

4.2. The role of antenna

For a single antenna element with antenna gain more than 30 dBi with half power beamwidth (HPBW) of approximately 6.5° , a reliable communication link is difficult to establish even in LOS condition at 60 GHz. This is due to the human blockage which can easily block and attenuate such a narrowbeam signal. To overcome this problem, a switched beam antenna array or adaptive antenna array is required to search and beamform to the available signal path. The array is subsequently required to track the signal path periodically. One might be interested to know how many antenna elements are required to achieve the intended antenna gain. This is different from the array gain which referred to the performance improvement in terms of SNR over single antenna. On the other hand, the gain of the antenna array can be described by the product of the directivity of the array with the efficiency of the antenna array. The directivity of the linear array is given by [27]

$$D = \frac{4\pi}{\iint |F_n(\phi, \theta)|^2 \sin \theta d\theta}, \quad (6)$$

where $F_n(\phi, \theta)$ is the normalized field pattern which can be expressed as a product of normalized element pattern and normalized array factor. The variables ϕ and θ denote the azimuth and elevation angle, respectively. For uniform linear

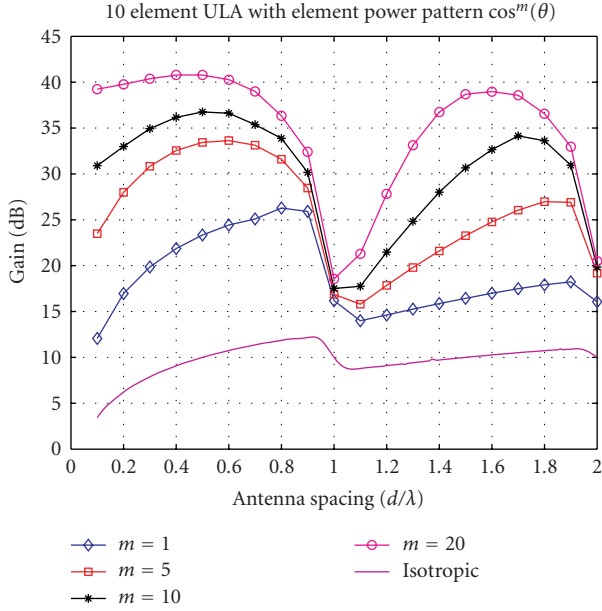


FIGURE 5: The antenna array gain as a function of antenna spacing for 10 elements ULA with different element gains.

array (ULA), the normalized array factor can be expressed as

$$f_n(\phi, \theta) = \frac{\sin((N/2)(kd \cos \theta + \beta))}{N \sin((1/2)(kd \cos \theta + \beta)}, \quad (7)$$

where N , d , and β are the number of antenna elements, antenna spacing between two adjacent elements, and phase shift, respectively. For omni-directional antenna, it can be shown that up to 100 elements are required to achieve only 23 dBi gain which is far from the required specification shown previously. Hence a more directive element is required to improve the overall gain of the array. As shown in Figure 5, to achieve a 40 dBi gain, 10 elements ULA with 16 dBi element spaced around $\lambda/2$ is required.

5. TECHNICAL CHALLENGES

Despite many advantages offered and high potentials applications envisaged in 60 GHz, there are number of technical challenges and open issues that must be solved prior to the successful deployment of this technology. These challenges can be broadly classified into channel propagation issues, antenna technology, RF solution, and choice of modulation.

Channel propagation

Although many channel measurements and modeling effort have been reported in the literature for various frequency range such as the 5 GHz WLAN band [28–30] and 3–10 GHz UWB band [31–39], there are still lack of channel measurements and modeling effort for the frequency range at 60 GHz. In general, the path loss at 60 GHz is significantly higher than those at lower frequencies. This is also true for transmission loss at 60 GHz for many materials

[23, 24, 40, 41]. The higher path loss and transmission loss at 60 GHz effectively limits the operation to one room. In order to have wider coverage, relays or regenerative repeaters are required. Furthermore, as described in Section 4, the use of high gain antenna is necessary to compensate the high path loss incurred, and the use of this single high gain antenna is only feasible if clear LOS condition is always guaranteed. In scenario where clear LOS is not guaranteed due to, for example, a movement of human, the antenna arrays solution becomes highly desirable. Unfortunately, there is no specific channel model at 60 GHz that sufficiently addresses the spatial properties and effect of human movement. Recent contributions which measured the angle of arrival of the received signal using antenna array [42] and rotational of directive antenna [43] show that an angle spread of approximately 14° in corridor and desktop environment, respectively. However, more measurements are required to further characterize and validate these results.

Furthermore, all of the channel models available are *radio channel* which are antenna dependent and are only valid for the particular antenna setups used in the measurement. To overcome this limitation, a *propagation channel* is required which excludes the effects of antenna [44] and allows the investigation of the effects of different type of antenna setups with different gain/beamwidth on the 60 GHz system performance. This is very important as measurements and ray tracings have shown that the use of high gain antenna can significantly reduce the delay spread of the radio channel when the Tx and Rx antennas are aligned [45]. However, a detrimental effect would be resulted for a slight pointing error of the main lobe of the antenna off the direction of arrival of the signal [46, 47]. In addition, measurements also demonstrated the effects of multipath suppression using circular polarization over linear polarization [48], but more extensive measurements are needed to affirm these results and to what extent this suppression occurs at 60 GHz.

Antenna technology

Many types of antenna structures are considered not suitable for 60 GHz WPAN/WLAN applications due to the requirements for low cost, small size, light weight, and high gain. In addition, 60 GHz antennas also require to be operated with approximately constant gain and high efficiency over the broad frequency range (57–66 GHz). The importance of beamforming at 60 GHz has been discussed in Section 4, which can be achieved by either switched beam arrays or phase arrays. Switched beam arrays have multiple fixed beams that can be selected to cover a given service area. It can be implemented much easier compared to the phase arrays which required the capability of continuously varying the progressive phase shift between the elements. The complexity of phase arrays at 60 GHz typically limits the number of elements. In [49], a 2×2 beam steering antenna with circular polarization at 61 GHz is developed. The gain is approximately 14 dBi with 20° HPBW. Similarly in [50], another 60 GHz integrated 4-element planar array is developed with average conversion loss of less than 10.6 dB for the four

channels. The implementation of larger phase array, however, presents some technical challenges such as requirement for higher feed network loss, more complex phase control network, stronger coupling between antennas as well as feed-lines, and so forth. These challenges make the design and fabrication of the larger phase arrays become more complex and expensive. Hence, more research are required to develop a low cost, small size, light weigh, and high gain steerable antenna array that can be integrated into the RF front end electronics.

Integrated circuit technology

The choice of integrated circuit (IC) technology depends on the implementation aspects and system requirements. The former is related to the issues such as power consumption, efficiency, dynamic range, linearity requirements, integration level, and so forth, while the later is related to the transmission rate, cost and size, modulation scheme, transmit power, bandwidth, and so forth. At mmWave, there are three competing IC technologies, namely: (1) group III and IV semiconductor technology such as Gallium Arsenide (GaAs) and Indium Phosphide (InP); (2) Silicon Germanium (SiGe) technology such as HBT and BiCMOS; and (3) Silicon technology such as CMOS and BiCMOS. There is no single technology that can simultaneously meet all the objectives defined in the technical challenges and system requirements. For example, GaAs technology allows fast, high gain, and low noise implementation but suffers poor integration and expensive implementation. On the other hand, SiGe technology is a cheaper alternative to the GaAs with comparable performance. In [51], the first mmWave fully antenna integrated SiGe chip has been demonstrated.

Typically, as have been witnessed in the past, for broad market exploitation and mass deployment, the size and cost are the key factors that drive to the success of a particular technology. In this regard, CMOS technology appears to be the leading candidate as it provides low-cost and high-integration solutions compared to the others at the expense of performance degradation such as low gain, linearity constraint, poor noise, lower transit frequency, and lower maximum oscillation frequency. Recent advances in CMOS technology [52] have demonstrated the feasibility of bulk CMOS process at 130 nm for 60 GHz RF building blocks, active and passive elements. More future research and investigations in developing a fully integrated CMOS chip solution have to be performed. Future technology should also aim at 90 nm and 65 nm CMOS processes in order to further improve the gain and lower power consumption of the devices.

Modulation schemes

The choice of modulation schemes for 60 GHz radio will be highly dependent on the propagation channel, the use of high gain antenna/antenna array, and the limitations imposed by the RF technology. For instance, if the delay spread of the underlying propagation channel is high, then an orthogonal frequency division multiplexing (OFDM) is an obvious

choice of modulation since OFDM can effectively turn the frequency selective channel into flat fading channel by dividing the high-rate stream into a set of parallel lower rate sub-streams. This simplifies the equalization technique for multi gigabit wireless system. On the other hand, high gain or circular polarized antenna systems can be used to significantly reduce the effect of multipath and therefore will favor simple modulation such as single carrier to save power consumption and cost.

Typically, in CMOS circuit implementation, the 60 GHz power amplifier has lower power and higher linearity requirement. This implies that the use of simple modulation than the OFDM system which suffers large peak-to-average ratio (PAPR) and can greatly reduce the efficiency of the power amplifier. Furthermore, the poor phase noise characteristic of 60 GHz CMOS also restricts the use of higher order modulation for quadrature amplitude modulation (QAM), phase shift keying (PSK), and frequency shift keying (FSK) to less than 16 QAM/16 PSK/16 FSK. The use of lower order modulation is also motivated by the huge unlicensed bandwidth available at 60 GHz. Hence, the choice of modulation is clearly a tradeoff of a number of issues which need to be well understood and characterized before a robust modulation scheme can be sought.

6. CONCLUSION

In this paper, an overview of the 60 GHz technology is presented. The huge unlicensed bandwidth coupled with higher allowable transmit power, small form factor, and advances in integrated circuit technology have made 60 GHz a very promising candidate for multigigabit applications. Intense efforts are underway to expedite the commercialization of this fascinating technology from standardization activities, industrial alliances and regulatory bodies. A simple feasibility study on wireless uncompressed video streaming on HDTV using realistic parameters revealed the roles of antenna in establishing a reliable 60 GHz communication link. The importance of antenna system are to provide sufficient power margin through array gain as well as to beam-form the signal to other significant paths in case of human blockage of the main path. Despite the clear advantages of 60 GHz system, a number of open issues and technical challenges have yet to be fully addressed. The propagation and implementation issues are the two aspects that require further optimization and research in order to obtain a truly efficient and low cost 60 GHz communication system.

REFERENCES

- [1] A. D. Oliver, "Millimeter wave systems - past, present and future," *IEE Proceedings*, vol. 136, no. 1, pp. 35–52, 1989.
- [2] <http://www.ieee802.org/15/pub/TG3c.html>.
- [3] S. K. Yong, "Multi gigabit wireless through millimeter wave in 60 GHz band," in *Proceedings of Wireless Conference Asia*, Singapore, November 2005.
- [4] FCC, "First Report and Order," February 2002, http://hraunfoss.fcc.gov/edocs_public/.

- [5] C.-C. Chong, F. Watanabe, and H. Inamura, "Potential of UWB technology for the next generation wireless communications," in *Proceedings of IEEE 9th International Symposium on Spread Spectrum Techniques and Applications (ISSSTA '06)*, pp. 422–429, Manaus, Amazon, Brazil, August 2006.
- [6] FCC, "Code of Federal Regulation, title 47 Telecommunication, chapter 1, part 15.255," October 2004.
- [7] Spectrum Management Telecommunications, "Radio Standard Specification-210, Issue 6, Low-Power Licensed-Exempt Radio Communication Devices (All Frequency Bands): Category 1 Equipment," September 2005.
- [8] Regulations for enforcement of the radio law 6-4-2 specified low power radio station (11) 59-66GHz band.
- [9] ACMA, "Radiocommunications (Low Interference Potential Devices) Class License Variation 2005 (no. 1)," August 2005.
- [10] Ministry of Information Communication of Korea, "Frequency Allocation Comment of 60 GHz Band," April 2006.
- [11] ETSI DTR/ERM-RM-049, "Electromagnetic compatibility and Radio spectrum Matters (ERM); System Reference Document; Technical Characteristics of Multiple Gigabit Wireless Systems in the 60 GHz Range," March 2006.
- [12] *Korean Frequency Policy & Technology Workshop, Session 7*, pp. 13–32, November 2005.
- [13] CEPT Recommendation T/R 22-03, "Provisional recommended use of the frequency range 54.25-66 GHz by terrestrial fixed and mobile systems," in *Proceedings of European Postal and Telecommunications Administration Collection (CEPT '90)*, pp. 1–3, Athens, Greece, January 1990, <http://www.ero.dk/documentation/>.
- [14] ERC Recommendation 12-09, "Radio Frequency Channel Arrangement for Fixed Service Systems Operating in the Band 57.0 - 59.0 GHz Which Do Not Require Frequency Planning, The Hague 1998 revised Stockholm," October 2004.
- [15] ECC Recommendation (05)02, "Use of the 64-66 GHz Frequency Band for Fixed Services," June 2005.
- [16] IEEE Standard 802.16 2001, "IEEE Standard for Local and Metropolitan Area Networks—Part 16 - Air Interface for Fixed Broadband Wireless Access Systems," 2001.
- [17] ARIB STD-T69, "Millimeter-Wave Video Transmission Equipment for Specified Low Power Radio Station," July 2004.
- [18] ARIB STD-T69, "Millimeter-Wave Data Transmission Equipment for Specified Low Power Radio Station (Ultra High Speed Wireless LAN System)," May 2001.
- [19] R. Roberts, "WiMedia 60 GHz Study Group," IEEE 802.15-05-0248-00-003c, Jacksonville, Fla, USA, May 2006.
- [20] A. Sadri, "802.15.3c Usage Model Document," IEEE 802.15-06-0055-14-003c, Jacksonville, Fla, USA, May 2006.
- [21] S. K. Yong, "TG3c Channel Modeling Sub-Committee Final Report (Draft)," IEEE 802.15-06-0195-02-003c, Jacksonville, Fla, USA, May 2006.
- [22] M. K. Simon and M. S. Alouini, *Digital Communication over Fading Channels*, Wiley-IEEE Press, New York, NY, USA, 2nd edition, 2004.
- [23] M. Fiacco and S. Saunders, "Final report for OFCOM - indoor propagation factors at 17 GHz and 60 GHz," August 1998.
- [24] C. R. Anderson and T. S. Rappaport, "In-building wideband partition loss measurements at 2.5 and 60 GHz," *IEEE Transactions on Wireless Communications*, vol. 3, no. 3, pp. 922–928, 2004.
- [25] S. Collonge, G. Zaharia, and G. E. Zein, "Influence of the human activity on wide-band characteristics of the 60 GHz indoor radio channel," *IEEE Transactions on Wireless Communications*, vol. 3, no. 6, pp. 2396–2406, 2004.
- [26] P. F. M. Smulders, *Broadband wireless LANs: a feasibility study*, Ph.D. thesis, Eindhoven University of Technology, Eindhoven, The Netherlands, 1995.
- [27] C. A. Balanis, *Antenna Theory: Analysis and Design*, John Wiley & Sons, New York, NY, USA, 2nd edition, 1997.
- [28] C.-C. Chong, C.-M. Tan, D. I. Laurenson, S. McLaughlin, M. A. Beach, and A. R. Nix, "A new statistical wideband spatio-temporal channel model for 5-GHz band WLAN systems," *IEEE Journal on Selected Areas in Communications*, vol. 21, no. 2, pp. 139–150, 2003.
- [29] C.-C. Chong, D. I. Laurenson, and S. McLaughlin, "Spatio-temporal correlation properties for the 5.2-GHz indoor propagation environments," *IEEE Antennas and Wireless Propagation Letters*, vol. 2, no. 1, pp. 114–117, 2003.
- [30] C.-C. Chong, C.-M. Tan, D. I. Laurenson, S. McLaughlin, and M. A. Beach, "A novel wideband dynamic directional indoor channel model based on a Markov process," *IEEE Transactions on Wireless Communications*, vol. 4, no. 4, pp. 1539–1552, 2005.
- [31] M. Z. Win and R. A. Scholtz, "On the robustness of ultra-wide bandwidth signals in dense multipath environments," *IEEE Communications Letters*, vol. 2, no. 2, pp. 51–53, 1998.
- [32] M. Z. Win and R. A. Scholtz, "On the energy capture of ultra-wide bandwidth signals in dense multipath environments," *IEEE Communication Letters*, vol. 2, no. 9, pp. 245–247, 1998.
- [33] R. J. Cramer, R. A. Scholtz, and M. Z. Win, "An evaluation of the ultra-wideband propagation channel," *IEEE Transactions on Antennas and Propagation*, vol. 50, no. 5, pp. 561–570, 2002.
- [34] D. Cassioli, M. Z. Win, and A. F. Molisch, "The ultra-wide bandwidth indoor channel: from statistical model to simulations," *IEEE Journal on Selected Areas in Communications*, vol. 20, no. 6, pp. 1247–1257, 2002.
- [35] M. Z. Win and R. A. Scholtz, "Characterization of ultra-wide bandwidth wireless indoor channels: a communication-theoretic view," *IEEE Journal on Selected Areas in Communications*, vol. 20, no. 9, pp. 1613–1627, 2002.
- [36] C.-C. Chong and S. K. Yong, "A generic statistical-based UWB channel model for high-rise apartments," *IEEE Transactions on Antennas and Propagation*, vol. 53, no. 8, pp. 2389–2399, 2005.
- [37] C.-C. Chong, Y.-E. Kim, S. K. Yong, and S.-S. Lee, "Statistical characterization of the UWB propagation channel in indoor residential environment," *Wireless Communications and Mobile Computing*, vol. 5, no. 5, pp. 503–512, 2005.
- [38] C.-C. Chong, "UWB channel modeling and impact of wide-band channel on system design," in *UWB Wireless Communications*, H. Arslan and Z. N. Chen, Eds., chapter 8, John Wiley & Sons, New York, NY, USA, 2006.
- [39] A. F. Molisch, D. Cassioli, C.-C. Chong, et al., "A comprehensive standardized model for ultrawideband propagation channels," *IEEE Transactions on Antennas and Propagation*, vol. 54, no. 11, pp. 3151–3166, 2006.
- [40] E. J. Violette, R. H. Espeland, R. O. DeBolt, and F. K. Schwering, "Millimeter-wave propagation at street level in an urban environment," *IEEE Transactions on Geoscience and Remote Sensing*, vol. 26, no. 3, pp. 368–380, 1988.
- [41] B. Langen, G. Lober, and W. Herzig, "Reflection and transmission behaviour of building materials at 60GHz," in *Proceedings of the 5th IEEE International Symposium on Personal, Indoor and Mobile Radio Communications (PIMRC '94)*, vol. 2, pp. 505–509, The Hague, Netherlands, September 1994.
- [42] M.-S. Choi, G. Grosskopf, and D. Rohde, "Statistical characteristics of 60 GHz wideband indoor propagation channel," in *Proceedings of the 16th International Symposium on Personal*

- Indoor and Mobile Radio Communications (PIMRC '05)*, vol. 1, pp. 599–603, Berlin, Germany, September 2005.
- [43] C. S. Liu, et al., “NICTA Indoor 60 GHz Channel Measurements and Analysis update,” IEEE 802.15-06-222-00-003c, Jacksonville, Fla, May 2006.
- [44] M. Steinbauer, A. F. Molisch, and E. Bonek, “The double-directional radio channel,” *IEEE Antennas and Propagation Magazine*, vol. 43, no. 4, pp. 51–63, 2001.
- [45] H. Yang, P. F. M. Smulders, and M. H. A. J. Herben, “Frequency selectivity of 60 GHz LOS and NLOS indoor radio channels,” in *Proceedings of IEEE Vehicular Technology Conference (VTC '06)*, Melbourne, Australia, May 2006.
- [46] M. R. Williamson, G. E. Athanasiadou, and A. R. Nix, “Investigating the effects of antenna directivity on wireless indoor communication at 60GHz,” in *Proceedings of IEEE International Symposium on Personal, Indoor and Mobile Radio Communications (PIMRC '97)*, vol. 2, pp. 635–639, Helsinki, Finland, September 1997.
- [47] T. Manabe, Y. Miura, and T. Ihara, “Effects of antenna directivity and polarization on indoor multipath propagation characteristics at 60 GHz,” *IEEE Journal on Selected Areas in Communications*, vol. 14, no. 3, pp. 441–448, 1996.
- [48] T. Manabe, K. Sato, H. Masuzawa, et al., “Polarization dependence of multipath propagation and high-speed transmission characteristics of indoor millimeter-wave channel at 60 GHz,” *IEEE Transactions on Vehicular Technology*, vol. 44, no. 2, pp. 268–274, 1995.
- [49] K.-C. Huang and Z. Wang, “Millimeter-wave circular polarized beam-steering antenna array for gigabit wireless communications,” *IEEE Transactions on Antennas and Propagation*, vol. 54, no. 2, part 2, pp. 743–746, 2006.
- [50] J.-Y. Park, Y. Wang, and T. Itoh, “A 60 GHz integrated antenna array for high-speed digital beamforming applications,” in *Proceedings of IEEE MTT-S International Microwave Symposium Digest*, vol. 3, pp. 1677–1680, Philadelphia, Pa, USA, June 2003.
- [51] B. Gaucher, “Completely Integrated 60 GHz ISM Band Front End Chip Set and Test Results,” IEEE 802.15-15-06-0003-00-003c, Big Island, Hawaii, USA, January 2006.
- [52] C. H. Doan, S. Emami, A. M. Niknejad, and R. W. Broderson, “Millimeter-wave CMOS design,” *IEEE Journal of Solid-State Circuits*, vol. 40, no. 1, pp. 144–155, 2005.

Research Article

60-GHz Millimeter-Wave Radio: Principle, Technology, and New Results

Nan Guo,¹ Robert C. Qiu,^{1,2} Shaomin S. Mo,³ and Kazuaki Takahashi⁴

¹ Center for Manufacturing Research, Tennessee Technological University (TTU), Cookeville, TN 38505, USA

² Department of Electrical and Computer Engineering, Tennessee Technological University (TTU), Cookeville, TN 38505, USA

³ Panasonic Princeton Laboratory (PPRL), Panasonic R&D Company of America, 2 Research Way, Princeton, NJ 08540, USA

⁴ Network Development Center, Matsushita Electric Industrial Co., Ltd., 4-12-4 Higashi-shinagawa, Shinagawa-ku, Tokyo 140-8587, Japan

Received 15 June 2006; Revised 13 September 2006; Accepted 14 September 2006

Recommended by Peter F. M. Smulders

The worldwide opening of a massive amount of unlicensed spectra around 60 GHz has triggered great interest in developing affordable 60-GHz radios. This interest has been catalyzed by recent advance of 60-GHz front-end technologies. This paper briefly reports recent work in the 60-GHz radio. Aspects addressed in this paper include global regulatory and standardization, justification of using the 60-GHz bands, 60-GHz consumer electronics applications, radio system concept, 60-GHz propagation and antennas, and key issues in system design. Some new simulation results are also given. Potentials and problems are explained in detail.

Copyright © 2007 Nan Guo et al. This is an open access article distributed under the Creative Commons Attribution License, which permits unrestricted use, distribution, and reproduction in any medium, provided the original work is properly cited.

1. INTRODUCTION

During the past few years, substantial knowledge about the 60-GHz millimeter-wave (MMW) channel has been accumulated and a great deal of work has been done toward developing MMW communication systems for commercial applications [1–16]. In 2001, the Federal Communications Commission (FCC) allocated 7 GHz in the 57–64 GHz band for unlicensed use. The opening of that big chunk of free spectrum, combined with advances in wireless communications technologies, has rekindled interest in this portion of spectrum once perceived for expensive point-to-point (P2P) links. The immediately seen opportunities in this particular region of spectrum include next-generation wireless personal area networks (WPANs). Now a question raises: do we really need to use the 60-GHz band? The answer is yes and in the next section we will explain this in detail. The bands around 60 GHz are worldwide available and the most recent global 60-GHz regulatory results are summarized in Figure 1 and Table 1.

The high frequencies are associated with both advantages and disadvantages. High propagation attenuation at 60 GHz (following the classic Friis formula) actually classifies a set of short-range applications, but it also means dense frequency

reuse patterns. Higher frequencies lead to smaller sizes of RF components including antennas. At MMW frequencies, not only are the antennas very small, but also they can be quite directional (coming with high antenna gain), which is highly desired. The cost concern is mainly related to the transceiver RF front ends. Traditionally, the expensive III–V semiconductors such as gallium arsenide are required for MMW radios [3–5, 12]. In the past few years, alternative semiconductor technologies have been explored [6–10, 13]. According to the reports about recent progress in developing the 60-GHz front-end chip sets [15], IBM engineers have demonstrated the first experimental 60-GHz transmitter and receiver chips using a high-speed alloy of silicon and germanium (SiGe); meanwhile researchers from UCLA, UC Berkeley Wireless Research Center (BWRC), and other universities or institutes are using a widely available and inexpensive complementary metal oxide semiconductor (CMOS) technology to build 60-GHz transceiver components. Each of the two technologies has advantages and disadvantages. But it was claimed by IBM that its SiGe circuit models worked surprisingly well at 60 GHz. It is no doubt that the SiGe versus CMOS debate will continue.

Two organizations that drive the 60-GHz radios are the IEEE standard body [17] and WiMedia alliance, an industrial

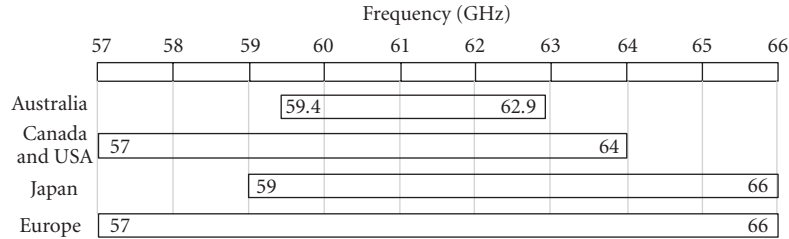


FIGURE 1: Spectra available around 60 GHz.

TABLE 1: Emission power requirements.

Region	Output power	Other considerations
Australia	10 mW into antenna	150 W peak EIRP
Canada and USA	500 mW peak	min. BW = 100 MHz
Japan	10 mW into antenna +50, -70% power change OT and TTR	47 dBi max. ant. Gain
Europe	+57 dBm EIRP	min. BW = 500 MHz

association [18]. The IEEE 802.15.3 Task Group 3c (IEEE 802.15.3c) is developing an MMW-based alternative physical layer (PHY) for the existing 802.15.3 WPAN Standard IEEE-Std-802.15.3-2003. With merging of former multiband OFDM alliance (MBOA), the WiMedia alliance is pushing a 60-GHz WPAN industrial standard, likely based on orthogonal frequency division multiplexing (OFDM) technology. The shooting data rate is 2 Gb/s or higher. Among a large number of proposals, the majority of them can be categorized to either multicarrier (meaning OFDM) or single-carrier types, where the former is expected to support extremely high data rates (say, up to 10 Gb/s; see Section 6.1 for explanation).

The rest of this paper is organized as follows. Section 2 explains why the 60-GHz radio is necessary. Potential applications of the 60-GHz radio are introduced in Section 3. Radio system concept is discussed in Section 4. Section 5 reports recent work on the 60-GHz channel modeling, and identifies an issue of the directional antenna impact on the medium access control (MAC) sublayer. In Section 6, a list of system design issues is discussed, followed by conclusions given in Section 7.

2. WHY IS THE 60-GHZ BAND ATTRACTIVE?

The answer is multifold. First of all, data rates or bandwidths are never enough, while the wireless multimedia distribution market is ever growing. Let us take a look at the microwave ultra-wideband (UWB) impulse radio [19–24]. UWB is a revolutionary power-limited technology for its unprecedented system bandwidth in the unlicensed band of 3.1–10.6 GHz allocated by FCC. The low emission and impulsive nature of the UWB radio leads to enhanced security in communications. Through-wall penetration capability makes UWB systems suitable for hostile indoor environments. The UWB impulse radio can be potentially imple-

mented with low-cost and low-power consumption (battery driven) components. UWB is able to deliver high-speed multimedia wirelessly and it is suitable for WPANs. However, one of the most challenging issues for UWB is that international coordination regarding the operating spectrum is difficult to achieve among major countries. In addition, the IEEE standards are not accepted worldwide. This spectral difficulty will deeply shape the landscape of WPANs in the future. Spectrum allocation, however, seems not to be an issue for 60-GHz WPANs. This is one of the reasons for the popularity of 60-GHz MMW.

Inter-system interference is another concern. The UWB band is overlaid over the 2.4- and 5-GHz unlicensed bands used for increasingly deployed WLANs, thus the mutual interferences would be getting worse and worse. This inter-system interference problem exists in Europe and Japan too. In order to protect the existing wireless systems operating in different regions, regulatory bodies in these regions are working on their own requirements for UWB implementation. Worldwide harmonization around 60 GHz is possible, but it is almost impossible for a regional UWB radio to work in another region. Figure 2 shows two spectral masks that set emission power limits in US and Japan. Unlicensed use in Japan is permitted at the 3.4–4.8 GHz and 7.25–10.25 GHz wireless spectra, the latter of which is reserved for indoor products only. Products using the lower 3.4–4.8 GHz spectrum will be required to implement detection and avoidance (DAA) technologies to avoid interference with other services operating at the same frequencies. When spectrum conflict is detected, the UWB signal strength has to be dropped.

Data-rate limitation is also a concern. Currently, the multiband OFDM (MB-OFDM) UWB systems can provide maximum data rate of 480 MB/s. This data rate can only support compressed video. Data rate for uncompressed video for high definition TV, such as high-definition multimedia interface (HDMI), can easily go over 2 Gb/s. Although the

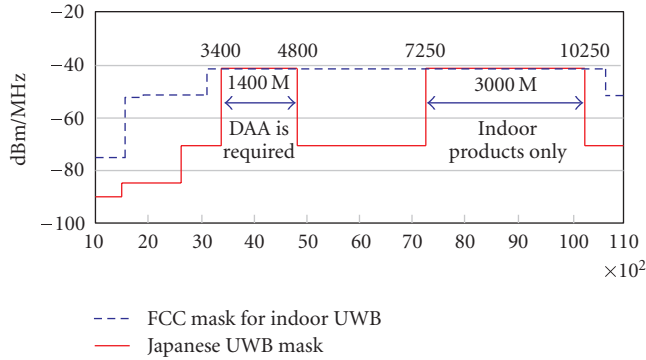


FIGURE 2: Emission power limits in US and Japan.

TABLE 2: Relationship between center frequencies and coverage range.

Band group	Center frequency (MHz)	Range (meter)
1	3,960	10.0
2	5,544	5.10
3	7,128	3.09
4	8,712	2.07
5	10,032	1.56

MB-OFDM UWB can be enhanced to support 2 Gb/s, the complexity, power consumption, and cost will increase accordingly.

Finally, variation of received signal strength over a given spectrum can be a bothering factor. For the MB-OFDM UWB systems, there are 5 band groups covering a frequency range from 3.1 GHz to 10.6 GHz. According to the Friis propagation rule, given the same transmitted power, propagation attenuation is inversely proportional to the square of a group center frequency. If band group 1 can cover 10 meters, coverage range for band group 5 is only 1.56 meters (see Table 2). On the other hand, because of relatively smaller change in frequency, coverage range does not change dynamically for the 60-GHz radio.

Therefore, the 60-GHz band is indeed an underexploited waterfront.

3. POTENTIAL CONSUMER ELECTRONICS APPLICATIONS AT 60 GHZ

Similar to the microwave UWB radio, the 60-GHz radio is suitable for high-data-rate and short-distance applications, but it suffers from less chance of inter-system interference than the UWB. People believe that the 60-GHz radio can find numerous applications in residential areas, offices, conference rooms, corridors, and libraries. It is suitable for in-home applications such as audio/video transmission, desktop connection, and support of portable devices. Judging by the interest shown by many leading CE and PC companies, applications can be divided into the following categories:

- (i) high definition video streaming,
- (ii) file transfer,

- (iii) wireless Gigabit Ethernet,
- (iv) wireless docking station and desktop point to multi-point connections,
- (v) wireless backhaul,
- (vi) wireless ad hoc networks.

The first three, that is, high definition video streaming, file transfer, and wireless Gigabit Ethernet, are considered as top applications. In each category, there are different use cases based on (1) whether they are used in residential area or office, (2) distance between the transmitters and receivers, (3) line-of-sight (LOS) or non-line-of-sight (NLOS) connection, (4) position of the transceivers, and (5) mobility of the devices. In [25], 17 use cases have been defined.

High-definition video streaming includes uncompressed video streaming for residential use. Uncompressed HDTV video/audio stream is sent from a DVD player to an HDTV. Typical distance between them is 5 to 10 meters with either LOS or NLOS connection. The high-definition streams can also come out from portable devices such as laptop computer, personal data assistant (PDA), or portable media player (PMP) that are placed somewhere in the same room with an HDTV. In this setting, coverage range might be 3 to 5 meters with either LOS or NLOS connection. NLOS results from that the direct propagation path is temporarily blocked by human bodies or objects. Uncompressed video streaming can also be used for a laptop-to-projector connection in conference room where people can share the same projector and easily connect to the projector without switching cables as in the case of cable connection.

File transfer has more use cases. In offices and residential areas it can happen between a PC and its peripherals including printers, digital cameras, camcorders, and so forth. It may also happen between portable devices such as PDA and PMP. A possible application may be seen in a kiosk in a store that sells audio/video contents. Except for connections between fixed devices, such as a PC and its peripherals, where NLOS may be encountered temporarily, most use cases involving portable devices should be able to have LOS connections because these devices can be moved to adjust aiming.

4. SYSTEM CONCEPT OF 60-GHZ RADIO

The system can be described in different ways. The system core is built mainly on physical layer and MAC sublayer. Typical MAC functions include multiple access, radio resource management, rate adaptation, optimization of transmission parameters, and quality of service (QoS), and so forth. When antenna arrays are employed, the MAC needs to support additional functions like probing, link set up, and maintenance.

The physical layer part of a transceiver contains an RF front end and a baseband back end. What should be highlighted in the front end is the multistage signal conversion. Taking an example from IBM's report [16], illustrated in Figure 3 is an MMW receiver front-end architecture with two-stage down conversion, where " $\times 3$ " is a frequency tripler (a type of frequency multiplier) and " $\div 2$ " is a frequency divider with factor 2. The phase lock loop (PLL) with voltage

controlled oscillator (VCO) generates a frequency higher than that of the reference source. The multiplier increases the frequency further. The RF signal is converted from RF to intermediate frequency (IF) and then to baseband. The resulted IF signal after the first down conversion has a lower center frequency thus is easy to handle. The second-stage conversion is quadrature down conversion leading to a pair of baseband outputs. In the transmitter front end, up conversion is achieved in a reversed procedure. Multistage signal conversion is an implementation approach which is associated with insertion loss contributed by multiple mixers. In addition, conversion between baseband and 60 GHz introduces an increased phase noise. If desired frequency at the input of the mixer is f and the original frequency from the reference source is f_0 , then the final phase noise will be $20 \log_{10}(f/f_0)$ dB stronger than the original level, without taking into account additional phase noise contributed by circuits. This is why phase noise enlargement could be a problem to the 60-GHz radio.

An antenna array technique called phased array [26–30] has been considered feasible for the 60-GHz radio. The phased array relies on RF phase rotators to achieve beam steering. One benefit of using antenna array is that the requirements for power amplifiers (PAs) can be reduced. According to reports from BWRC, CMOS amplifier gain at 60 GHz is below 12 dB [2], which raises a concern about limited transmitted power. Note that the transmitter-side antenna array automatically achieves spatial power combining [2]. Figure 4 is a transmitter configuration with a phased array and a bank of PAs, where each branch contains a phase rotator, a PA, and an antenna element. If each branch can emit a certain amount of power, an M -branch transmitter can provide roughly $20 \log_{10} M$ dB more power at the receiver, compared to the case of a single-antenna transmitter.

To see some quantitative results, a set of simulations have been conducted considering the following setting:

- (i) center frequency: 60 GHz,
- (ii) modulation: OQPSK,
- (iii) symbol duration: 1 nanosecond (bit rate 2 Gb/s),
- (iv) shaping filter: square-root raised cosine (SR-RC) with roll-off factor 0.3,
- (v) PA: Rapp model with gain = 12, smooth factor = 2, and 1 dB compression input power = 7 dBm (assuming 50 ohm input impedance),
- (vi) antenna type: single-directional antenna at both Tx and Rx with 7 dBi gain,
- (vii) channel model: LOS channel with no multipath,
- (viii) transmit power (EIRP): 8.85 dBm,
- (ix) low-noise amplifier gain: 12 dB,
- (x) receiver noise figure: 10 dB,
- (xi) detection method: matched filter.

This setting meets the emission power requirements in all regions. To isolate phase noise issue, it is intentionally to use the one-path channel model and to prevent the signal from being clipped by the PA. The PA's input power is about -10.15 dBm which is far below the assumed 1 dB compression power (7 dBm), implying that the PA's nonlinearity

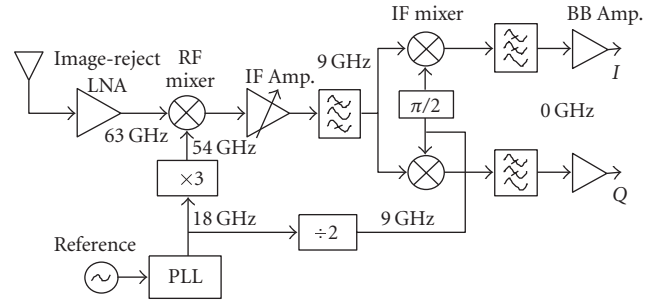


FIGURE 3: A proposed RF front-end architecture [16].

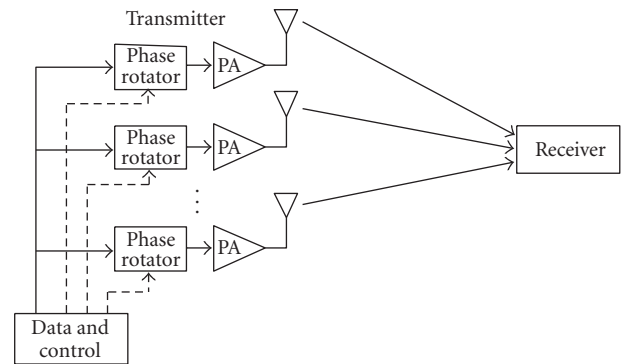


FIGURE 4: BER versus distance for different levels of phase noise.

would be negligible for this specific setting. The impact of phase noise on bit-error rate (BER) can be seen in Figure 5, where the abscissa represents the transmission distance between the transmitter and receiver. Basically, when phase-noise level is above -85 dBc at 1 MHz, it is not able to support a bit rate of 2 Gbps using OQPSK (or QPSK). It can be imaged that higher-order phase modulation or quadrature modulation would be more sensitive to phase noise. These results suggest that phase noise is a big obstacle to increasing data rate or extending distance.

5. PROPAGATION AND ANTENNA EFFECT

60-GHz channel characteristics have been well studied in the past. References [31–40] are some of most recent experimental work in uncovering the behavior of the channels. It has been noted that the channels around 60 GHz do not exhibit rich multipath, and the non-line-of-sight (NLOS) components suffer from tremendous attenuation. These channel characteristics are in favor of reducing multipath effect, but makes communications difficult in NLOS environments. With a plenty of measurement contributions, the IEEE 802.15.3c is currently working to set the statistical description of a 60-GHz S-V channel model based upon contributed empirical measurements. Shown in Table 3 is a summary of measured data [40]. Proposed by NICT (Yokosuka, Japan) is an enhanced S-V channel model called TSV model, and in the case of LOS it contains two paths. A set

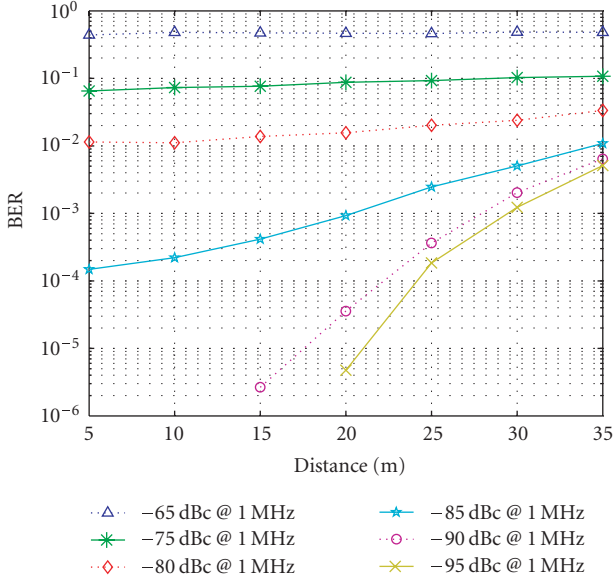


FIGURE 5: BER versus distance for different levels of phase noise.

TABLE 3: Summary of measured data.

Source	Measured environments		AoA
NICTA	Office desktop	(N)LOS ¹	Yes
	Office corridor	(N)LOS ¹	
	Closed office	(N)LOS ¹	
NICT Japan	Empty residential	(N)LOS ¹	Yes
	Open-plan office	NLOS	
University of Massachusetts	Office cubicles	LOS, NLOS	Yes
	Office corridor		
	Closed office		
	Homes		
IMST	Library	LOS, NLOS	Virtual ²
France Telecom	Cluttered residential	LOS, NLOS	Virtual ²
	Open-plan office	LOS, NLOS	
	Conference room	LOS, NLOS	
IBM	Library	LOS, NLOS	No
	Office cubicles	LOS, NLOS	
	Cluttered residential	LOS, NLOS	

¹Inherent NLOS component due to directionality of the antenna.²Data measured over linear and grid arrays.

of 10-channel models have been proposed and the mappings between environments and channel models are listed in Table 4 [25].

At 60 GHz, the antennas are in centimeter or sub-centimeter size, and achieving 10 dBi antenna gain is practical, which encourages us to use directional antennas since a high antenna gain (equivalently, narrow antenna pattern or high directivity) is desired to improve the signal-to-noise ratio (SNR) and reduce inter-user interference. However, the 60-GHz radio is sensitive to shadowing due to high attenuation of NLOS propagation, and the directional antennas can

TABLE 4: Mapping of environment to channel model.

Channel model	Scenario	Environment name
CM1	LOS	Office
CM2	NLOS	
CM3	LOS	Desktop
CM4	LOS	Residential
CM5	NLOS	
CM6	LOS	Conference room
CM7	NLOS	
CM8	LOS	Corridor
CM9	LOS	Library
CM10	NLOS	

make it more problematic when the LOS path is blocked and in the scenarios that require mobility without aiming. In order to cover all directions of interest while providing certain antenna gain, two beam steering solutions, antenna switching/selection (simple beam steering method) [41] and phase-array antennas [2, 26–30], have been suggested. To cooperate with beam forming or steering, traditional MAC designed for omni-directional antennas is no longer optimal [42, 43]. One open research topic is cross-layer optimization considering the impact of antenna directivity on the MAC.

6. SYSTEM DESIGN ISSUES

This section does not discuss system design systematically, but goes through some issues involved in the system design.

6.1. Single carrier versus multicarrier

Here by multicarrier we mean OFDM. OFDM is an effective means to mitigate multipath effect, although it has disadvantages of high peak-to-average power ratio, higher sensitivity to the phase noise [44], and relatively high power consumption at the transmitter. According to some 60-GHz channel measurement reports, the NLOS components suffer from much higher losses than the LOS component. LOS connection appears in many suggested application scenarios. In addition, directional antennas and beam steering are highly recommended for the 60-GHz radio. All these facts suggest that at 60 GHz, mitigation of multipath effect is not the number-one issue, and the single-carrier approach should be comparable to its multicarrier counterpart in terms of spectral efficiency. However, the multicarrier approach indeed has some advantages from implementation point of view: the transceiver can be efficiently implemented using IFFT/FFT, and frequency-domain equalization is rather easy and flexible. At this point, the single-carrier approach is considered for low-end applications. For example, single-carrier transmission with on-off keying (OOK) modulation should have no problem to support data rates up to 2 Gb/s over an LOS link of 2-GHz bandwidth, and it can be chosen to build low-cost wireless devices. Higher data rate can be expected if wider bandwidth or multiband is utilized. If both single

carrier and multicarrier solutions are accepted, compatibility between them is an issue.

6.2. Selection of modulation schemes

The following factors need to be considered in selecting modulation scheme: spectral efficiency, linearity of power amplifier (PA), phase-noise level, and scalability, and so forth. Plotted in Figure 6 are spectra of several modulation signals with different pulse shaping, where “SR-RC” stands for “square-root raised cosine,” T_S is the symbol duration and each symbol contains two bits, and the Gaussian filter for GMSK has a 3-dB bandwidth of $0.3/T_S$. Among the modulation schemes considered in Figure 6, only GMSK and OQPSK/QPSK with SR-RC shaping can provide fast spectral roll off. If B is one-sided bandwidth of modulated signal, the bandwidth efficiency is equal to $1/(T_S B)$ symbols/s/Hz. Obviously, none of GMSK and OQPSK/QPSK with SR-RC shaping can achieve a 2-bits/s/Hz (or 1-symbol/s/Hz) bandwidth efficiency. Illustrated in Figure 7 is the trajectory of a segment of OQPSK signal with roll-off factor 0.3. It can be seen in Figure 7 that the trajectory is no longer a square (OQPSK with rectangular shaping has a square trajectory). The shaping filter for bandwidth efficiency actually makes the amplitude more fluctuating (a purely constant-envelope modulation scheme, such as MSK, has a circle trajectory). QPSK is convenient to be down scaled to BPSK or up scaled to 8 PSK. Because of relatively high-phase noise at 60 GHz (due to limited Q-value, the achievable phase noise is around -85 dBc/Hz at 1 MHz frequency offset [2]), higher order modulation schemes such as 16 QAM would be too challenging.

Though OOK is not a bandwidth-efficient modulation, it is a very good candidate for low-cost devices since OOK-modulated signal can be noncoherently demodulated using cheap circuit. In addition, OOK does not require linear PA, so that large power back off is not necessary and the PA would be very efficient in terms of power consumption. GMSK is a constant-envelope modulation scheme with fast roll-off property, and it is the best choice for using maximally the PA (assuming single carrier), but its theoretical bandwidth efficiency is around 1.33 bits/s/Hz. Also, at the bit rate of a few Gigabits/s, it is not clear at present whether or not the Viterbi algorithm (for GMSK demodulation) can be implemented at acceptable price.

6.3. Other issues

It is desired to reuse IEEE 802.15.3 MAC for the 60-GHz radio. Potential impacts on the MAC come from high-data rate, high-antenna directivity, shadowing, and maybe compatibility between single carrier and multicarrier. Chance of signal blocking is good in indoor LOS-dominated environments, especially when beam forming or steering are employed. In other words, fast acquiring and maintaining a reliable link is critical to the 60-GHz radio. Effectively implementing these functions is very challenging and it needs involvement of both PHY and MAC. Dual-band (microwave and MMW) operation was proposed as a mea-

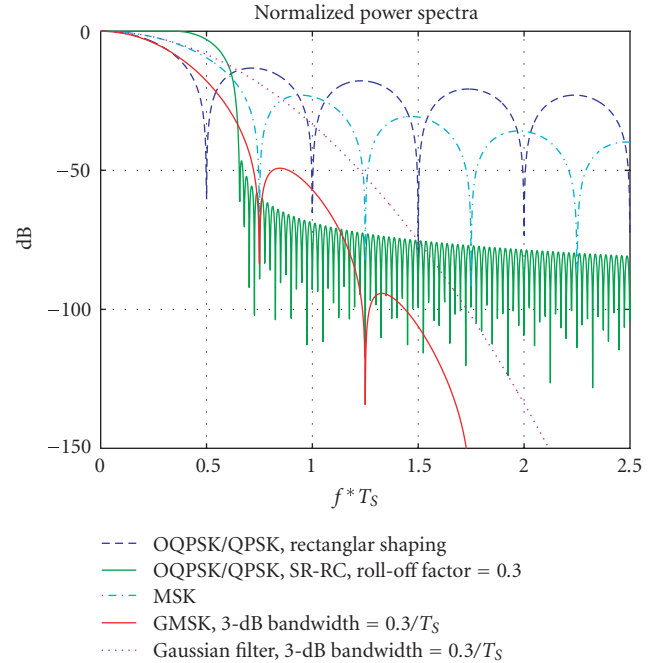


FIGURE 6: Spectra of different modulation schemes.

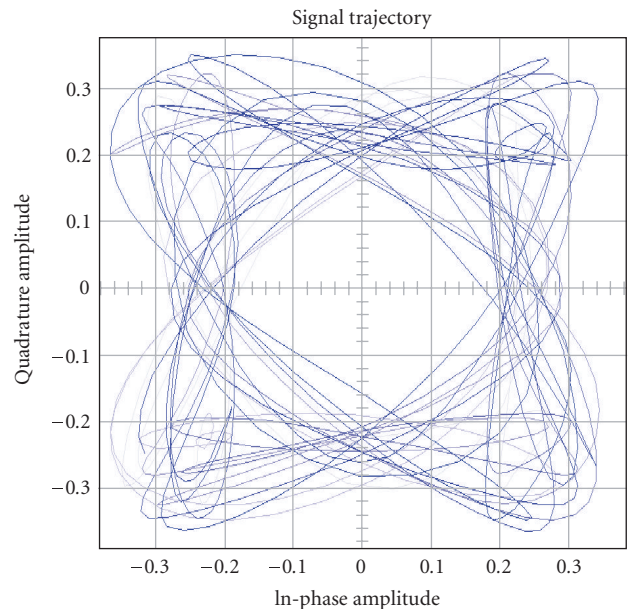


FIGURE 7: Trajectory of OQPSK with square-root raised cosine shaping (roll-off factor = 0.3; based on a simulation of 100 random symbols).

sure against both coverage limitation and severe shadowing [1]. Possible dual-band combinations include WiFi/MMW and UWB/MMW. Obviously, dual-band operation would increase complexity at both PHY and MAC, implying a higher-cost solution. When pulse-based low-duty-cycle signaling is employed, some uncoordinated multiple-access methods can be more efficient than CSMA/CA. Such multiple-access

methods include rate-division multiple access (RDMA) [45] and delay-capture-based multiple access [46–48]. All of these pose challenges for optimal design of MAC.

7. CONCLUSIONS

The 60-GHz radio has been discussed in different aspects. Positive moves can be seen in standardization and front-end development. Though potential is clear, there are many problems. Technically, success of the 60-GHz radio will largely depend on the advance of 60-GHz front-end technology. The SiGe versus CMOS debate will continue and it is not clear when we will see high-speed front ends with acceptable price. There are many questions to answer in designing PHY and MAC. Here are some examples: single carrier or multicarrier, or both? what kind of modulation? how to optimally control antennas from MAC? Breakthroughs in beam forming or steering and low-phase-noise local oscillator (LO) are expected. It will be very likely that the future market of the 60-GHz radio will be a mixture of varieties covering a full range of applications from low end to high end.

ACKNOWLEDGMENT

This work was supported in part by Panasonic R&D Company of America, Panasonic Princeton Laboratory (PPRL).

REFERENCES

- [1] P. Smulders, "Exploiting the 60 GHz band for local wireless multimedia access: prospects and future directions," *IEEE Communications Magazine*, vol. 40, no. 1, pp. 140–147, 2002.
- [2] C. H. Doan, S. Emami, D. A. Sobel, A. M. Niknejad, and R. W. Brodersen, "Design considerations for 60 GHz CMOS radios," *IEEE Communications Magazine*, vol. 42, no. 12, pp. 132–140, 2004.
- [3] H. Daembkes, B. Adelseck, L. P. Schmidt, and J. Schroth, "GaAs MMIC based components and frontends for millimeterwave communication and sensor systems," in *Proceedings of IEEE Microwave Systems Conference (NTC '95)*, pp. 83–86, Orlando, Fla, USA, May 1995.
- [4] R. L. Van Tuyl, "Unlicensed millimeter wave communications a new opportunity for MMIC technology at 60 GHz," in *Proceedings of the 18th Annual IEEE Gallium Arsenide Integrated Circuit Symposium*, pp. 3–5, Orlando, Fla, USA, November 1996.
- [5] M. Siddiqui, M. Quijije, A. Lawrence, et al., "GaAs components for 60 GHz wireless communication applications," in *Proceedings of GaAs Mantech Conference*, San Diego, Calif, USA, April 2002.
- [6] S. Reynolds, B. Floyd, U. Pfeiffer, and T. Zwick, "60 GHz transceiver circuits in SiGe bipolar technology," in *IEEE International Solid-State Circuits Conference. Digest of Technical Papers (ISSCC '04)*, vol. 1, pp. 442–538, San Francisco, Calif, USA, February 2004.
- [7] C. H. Doan, S. Emami, A. M. Niknejad, and R. W. Brodersen, "Design of CMOS for 60 GHz applications," in *IEEE International Solid-State Circuits Conference. Digest of Technical Papers (ISSCC '04)*, vol. 1, pp. 440–538, San Francisco, Calif, USA, February 2004.
- [8] W. Winkler, J. Borngräber, H. Gustat, and F. Korndörfer, "60 GHz transceiver circuits in SiGe:C BiCMOS technology," in *Proceedings of the 30th European Solid-State Circuits Conference (ESSCIRC '04)*, pp. 83–86, Leuven, Belgium, September 2004.
- [9] S. K. Reynolds, "A 60-GHz superheterodyne downconversion mixer in Silicon-Germanium bipolar technology," *IEEE Journal of Solid-State Circuits*, vol. 39, no. 11, pp. 2065–2068, 2004.
- [10] B. A. Floyd, S. K. Reynolds, U. R. Pfeiffer, T. Zwick, T. Beukema, and B. Gaucher, "SiGe bipolar transceiver circuits operating at 60 GHz," *IEEE Journal of Solid-State Circuits*, vol. 40, no. 1, pp. 156–167, 2005.
- [11] N. Deparis, A. Bendjabballah, A. Boe, et al., "Transposition of a baseband UWB signal at 60 GHz for high data rate indoor WLAN," *IEEE Microwave and Wireless Components Letters*, vol. 15, no. 10, pp. 609–611, 2005.
- [12] S. E. Gunnarsson, C. Kärnfelt, H. Zirath, et al., "Highly integrated 60 GHz transmitter and receiver MMICs in a GaAs pHEMT technology," *IEEE Journal of Solid-State Circuits*, vol. 40, no. 11, pp. 2174–2185, 2005.
- [13] S. Pinel, C.-H. Lee, S. Sarkar, et al., "Low cost 60 GHz Gb/s radio development," in *Progress in Electromagnetics Research Symposium*, pp. 483–484, Cambridge, Mass, USA, March 2006.
- [14] S. Sarkar, P. Sen, S. Pinel, C. H. Lee, and J. Laskar, "Si-based 60GHz 2X subharmonic mixer for multi-Gigabit wireless personal area network application," in *Proceedings of IEEE MTT-S International Microwave Symposium*, San Francisco, Calif, USA, June 2006.
- [15] S. K. Moore, "Cheap chips for next wireless frontier," *IEEE Spectrum*, vol. 43, pp. 12–13, 2006.
- [16] B. Gaucher, "Completely integrated 60 GHz ISM band front end chip set and test results," IEEE 802.15 TG3c document: 15-06-0003-00-003c, January 2006.
- [17] IEEE 802.15 Working Group for WPAN, <http://www.ieee802.org/15/>.
- [18] WiMedia alliance, <http://www.wimedia.org/>.
- [19] R. Scholtz, "Multiple access with time-hopping impulse modulation," in *Proceedings of IEEE Military Communications Conference (MILCOM '93)*, vol. 2, pp. 447–450, Boston, Mass, USA, October 1993.
- [20] M. Z. Win and R. A. Scholtz, "Ultra-wide bandwidth time-hopping spread-spectrum impulse radio for wireless multiple-access communications," *IEEE Transactions on Communications*, vol. 48, no. 4, pp. 679–689, 2000.
- [21] R. C. Qiu, H. Liu, and X. Shen, "Ultra-wideband for multiple access communications," *IEEE Communications Magazine*, vol. 43, no. 2, pp. 80–87, 2005.
- [22] R. C. Qiu, R. A. Scholtz, and X. Shen, "Guest editorial special section on ultra-wideband wireless communications—a new horizon," *IEEE Transactions on Vehicular Technology*, vol. 54, no. 5, pp. 1525–1527, 2005.
- [23] X. Shen, M. Guizani, H.-H. Chen, R. C. Qiu, A. F. Molisch, and L. B. Milstein, "Guest editorial ultra-wideband wireless communications—theory and applications," *IEEE Journal on Selected Areas in Communications*, vol. 24, no. 4, pp. 713–716, 2006, editorial on special issue on UWB.
- [24] R. C. Qiu, X. Shen, M. Guizani, and T. Le-Ngoc, "Introduction," in *UWB Wireless Communications*, X. Shen, M. Guizani, R. C. Qiu, and T. Le-Ngoc, Eds., John Wiley & Sons, New York, NY, USA, 2006.
- [25] A. Sadri, "802.15.3c Usage Model Document (UMD), Draft," IEEE 802.15 TG3c document: 15-06-0055-14-003c, January 2006.

- [26] J. Park, Y. Wang, and T. Itoh, "A 60 GHz integrated antenna array for high-speed digital beamforming applications," <http://www.mwlab.ee.ucla.edu/>.
- [27] A. Hajimiri, A. Komijani, A. Natarajan, R. Chunara, X. Guan, and H. Hashemi, "Phased array systems in silicon," *IEEE Communications Magazine*, vol. 42, no. 8, pp. 122–130, 2004.
- [28] X. Guan, H. Hashemi, and A. Hajimiri, "A fully integrated 24-GHz eight-element phased-array receiver in silicon," *IEEE Journal of Solid-State Circuits*, vol. 39, no. 12, pp. 2311–2320, 2004.
- [29] H. Hashemi, X. Guan, A. Komijani, and A. Hajimiri, "A 24-GHz SiGe phased-array receiver - LO phase-shifting approach," *IEEE Transactions on Microwave Theory and Techniques*, vol. 53, no. 2, pp. 614–626, 2005.
- [30] A. Natarajan, A. Komijani, and A. Hajimiri, "A fully integrated 24-GHz phased-array transmitter in CMOS," *IEEE Journal of Solid-State Circuits*, vol. 40, no. 12, pp. 2502–2514, 2005.
- [31] M. R. Williamson, G. E. Athanasiadou, and A. R. Nix, "Investigating the effects of antenna directivity on wireless indoor communication at 60 GHz," in *Proceedings of the 8th IEEE International Symposium on Personal, Indoor and Mobile Radio Communications (PIMRC '97)*, vol. 2, pp. 635–639, Helsinki, Finland, September 1997.
- [32] D. Dardari and V. Tralli, "High-speed indoor wireless communications at 60 GHz with coded OFDM," *IEEE Transactions on Communications*, vol. 47, no. 11, pp. 1709–1721, 1999.
- [33] H. Xu, V. Kukshya, and T. S. Rappaport, "Spatial and temporal characteristics of 60-GHz indoor channels," *IEEE Journal on Selected Areas in Communications*, vol. 20, no. 3, pp. 620–630, 2002.
- [34] A. G. Siamarou, "Broadband wireless local-area networks at millimeter waves around 60 GHz," *IEEE Antennas and Propagation Magazine*, vol. 45, no. 1, pp. 177–181, 2003.
- [35] C. R. Anderson and T. S. Rappaport, "In-building wideband partition loss measurements at 2.5 and 60 GHz," *IEEE Transactions on Wireless Communications*, vol. 3, no. 3, pp. 922–928, 2004.
- [36] F. Aryanfar and K. Sarabandi, "A millimeter-wave scaled measurement system for wireless channel characterization," *IEEE Transactions on Microwave Theory and Techniques*, vol. 52, no. 6, pp. 1663–1670, 2004.
- [37] S. Collonge, G. Zaharia, and G. El Zein, "Influence of the human activity on wide-band characteristics of the 60 GHz indoor radio channel," *IEEE Transactions on Wireless Communications*, vol. 3, no. 6, pp. 2396–2406, 2004.
- [38] N. Moraitis and P. Constantinou, "Indoor channel measurements and characterization at 60 GHz for wireless local area network applications," *IEEE Transactions on Antennas and Propagation*, vol. 52, no. 12, pp. 3180–3189, 2004.
- [39] T. Zwick, T. J. Beukema, and H. Nam, "Wideband channel sounder with measurements and model for the 60 GHz indoor radio channel," *IEEE Transactions on Vehicular Technology*, vol. 54, no. 4, pp. 1266–1277, 2005.
- [40] A. Mathew, "Channel model status report," IEEE 802.15 TG3c document: IEEE 802.15-06/0037r2, May 2006.
- [41] P. F. M. Smulders, M. H. A. J. Herben, and J. George, "Application of five-sector beam antenna for 60 GHz wireless LAN," <http://www.brabantbreedband.nl/>.
- [42] R. Ramanathan, J. Redi, C. Santivanez, D. Wiggins, and S. Polit, "Ad hoc networking with directional antennas: a complete system solution," *IEEE Journal on Selected Areas in Communications*, vol. 23, no. 3, pp. 496–506, 2005.
- [43] F. Dai and J. Wu, "Efficient broadcasting in ad hoc wireless networks using directional antennas," *IEEE Transactions on Parallel and Distributed Systems*, vol. 17, no. 4, pp. 335–347, 2006.
- [44] T. Pollet, M. Van Bladel, and M. Moeneclaey, "BER sensitivity of OFDM systems to carrier frequency offset and Wiener phase noise," *IEEE Transactions on Communications*, vol. 43, no. 234, pp. 191–193, 1995.
- [45] M. Weisenhorn and W. Hirt, "Uncoordinated rate-division multiple-access scheme for pulsed UWB signals," *IEEE Transactions on Vehicular Technology*, vol. 54, no. 5, pp. 1646–1662, 2005.
- [46] D. H. Davis and S. A. Gronemeyer, "Performance of slotted ALOHA random access with delay capture and randomized time of arrival," *IEEE Transactions on Communications Systems*, vol. 28, no. 5, pp. 703–710, 1980.
- [47] K. Cheun, "Optimum arrival-time distribution for delay capture in spread-spectrum packet radio networks," *IEEE Transactions on Vehicular Technology*, vol. 46, no. 4, pp. 981–991, 1997.
- [48] N. Guo, R. C. Qiu, and B. M. Sadler, "A UWB radio network using multiple delay capture enabled by time reversal," in *Proceedings of Military Communications Conference (MILCOM '06)*, Washington, DC, USA, October 2006.

Research Article

60 GHz Indoor Propagation Studies for Wireless Communications Based on a Ray-Tracing Method

C.-P. Lim, M. Lee, R. J. Burkholder, J. L. Volakis, and R. J. Marhefka

*ElectroScience Laboratory, Department of Electrical and Computer Engineering, Ohio State University,
1320 Kinnear Road, Columbus, OH 43212, USA*

Received 28 April 2006; Revised 13 November 2006; Accepted 13 November 2006

Recommended by Chia-Chin Chong

This paper demonstrates a ray-tracing method for modeling indoor propagation channels at 60 GHz. A validation of the ray-tracing model with our in-house measurement is also presented. Based on the validated model, the multipath channel parameter such as root mean square (RMS) delay spread and the fading statistics at millimeter wave frequencies are easily extracted. As such, the proposed ray-tracing method can provide vital information pertaining to the fading condition in a site-specific indoor environment.

Copyright © 2007 C.-P. Lim et al. This is an open access article distributed under the Creative Commons Attribution License, which permits unrestricted use, distribution, and reproduction in any medium, provided the original work is properly cited.

1. INTRODUCTION

Increasing demand of real-time high-speed applications calls for wireless local area network (LAN) operating in the 60 GHz band as part of the 4th generation (4G) system. The 60 GHz band has spiked great interest [1–7] because of its large bandwidth (7 GHz) allocated for future dense wireless local communications, particularly as relates to large wireless LAN bridges, and wireless high-quality video-conferencing. To establish such links, wireless systems which exploit time, frequency, and spatial multiplexing may be required. Design of these communication systems involves space-time coding, adaptive antennas, and rake reception which rely strongly on the characterization of the propagation channel. Previous work in channel characterizations at these millimeter (mm) wave frequencies have depended on measurements [2, 8–11]. However, measurements can be expensive (especially in the mm-wave band) as compared to electromagnetic (EM) modeling approaches. Since rigorous numerical methods are ruled out due to the very short wavelength at mm waves, we consider high-frequency asymptotic approaches such as ray-tracing (RT) method for modeling the channels. RT methods have the capability to solve electrically large problems relatively fast and, as such, they become an obvious candidate for the extraction of channel parameters. In this paper, we compare the channel parameters based on the RT model with in-house collected measurements, and measurements obtained from [8]. Subsequently, we provide results

for the fading statistics of the received power in two typical indoor propagation channels, namely, within a room and in a hallway.

The paper is organized as follows. The next section presents the validation of the ray-tracing model using measurements in the 2–3 GHz band. Section 3 describes the EM modeling of the room and hallway, and the simulation setup. Extraction of the channel parameters and modeling of the fading statistics are presented in Section 4. Section 5 concludes the paper.

2. VALIDATION OF THE RAY-TRACING MODEL WITH MEASUREMENTS

The numerical electromagnetic code-basic scattering code (NEC-BSC) [12], which is based on 3-dimensional (3D) ray-tracing technique, utilizes the uniform asymptotic concepts formulated in terms of the uniform geometrical theory of diffraction (UTD) [13, 14]. As such, UTD is ideal for understanding the high-frequency response of signal in a complex environment whereby the basic structural features (that are crucial for accuracy) of that complex environment are necessary for modeling. In doing so, this allows for the use of ray optical techniques for obtaining the incident, reflected, and diffracted rays, contributed from these various basic structures. As a result, the reflected and diffraction fields are subsequently determined using the UTD solutions

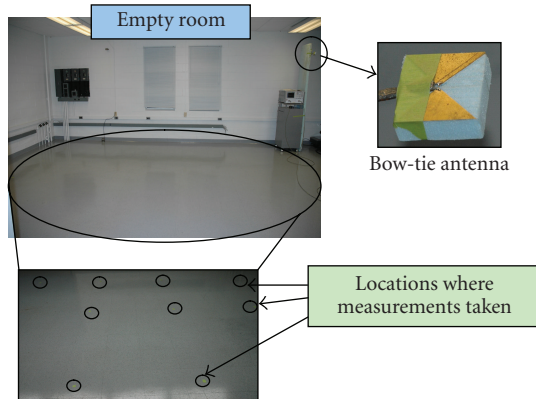


FIGURE 1: Photograph of the empty room where the measurements were conducted. The inset shows some of the measuring locations.

which consist of the individual rays that are summed with the geometrical optics in the far zone of the scatterer. As we know, the rays from a given scatterer tend to interact with other nearby objects, resulting into higher-order rays. As such, NEC-BSC was built to take care of all these high-order interactions, but not all high-order contributions are significant. Therefore, one can also choose to include only dominant contributions in NEC-BSC. Given all these, NEC-BSC is appropriate in this 60 GHz propagation study and it is employed to obtain power delay profiles (PDPs) for the indoor propagation channel. As a first step, we proceed to validate the ray-tracing model with measurements for the indoor propagation channel considered in this paper.

2.1. Measurement setup

The measurement setup consisted of a network analyzer (i.e., Agilent E8362B), a pair of 180° hybrid couplers, and a pair of identical bow-tie antennas (denoted as Antenna 1 and Antenna 2). The bow-tie antennas were designed to have a center frequency of 2.5 GHz, with fanning angle 45° and 1 GHz bandwidth sufficient for this measurement. An empty room was chosen (see Figure 1) whose dimensions are depicted in Figure 2. Specifically, the room is of length 7.72 m, width 5.84 m, and height 2.82 m. Antenna 1, operating as a transmitter, was positioned at (0.94 m, 0.76 m) and at a height of 2.24 m. Antenna 2, serving as a receiver, was placed at 18 different locations inside the room (standing at the height of 1.12 m) for measurements. The detailed position of these 18 locations is depicted in Figure 2. For consistency, four measurements were taken at each of these locations and the average of these four measurements was used as the result. For each measurement, a total of 1601 frequency points (i.e., S_{21}) between 2 GHz and 3 GHz was used, resulting in a frequency step of 0.625 MHz. This frequency resolution implied a maximum excess delay of about 1600 ns and a temporal resolution of 1 ns (because of the 1 GHz bandwidth). We remark that a signal-to-noise ratio (SNR) of at least 20 dB was maintained

throughout all measurements (via averaging during data sampling).

2.2. Simulations

For our simulations, the NEC-BSC was used. We computed the response at the same 1601 continuous wave (CW) tones evenly spaced between 2 GHz and 3 GHz as done with the measurements. For these calculations, the direct and reflected rays up to tenth order (from the walls, ceiling, and floor) were included. The walls, floor, and ceiling were characterized by relative dielectric constant $\epsilon_r = 4.22 - j0.02$ whereas the walls were of thickness 14.5 cm. The relative dielectric constant was taken from the detailed study of material characterization (based on measurements) documented in [15]. Both the transmitting and receiving antennas (i.e., Antenna 1 and Antenna 2) were modeled in NEC-BSC as having a donut antenna pattern as shown in Figure 3. The figure shows the antenna pattern obtained from Ansoft HFSS simulation. These antennas (with the same dimensions) were built and used in our in-house measurements. As such, one would expect the antenna pattern in the measurements to be identical to the one obtained in HFSS simulation (refer to Figure 3). For the propagation study, the similar antenna pattern was employed in the NEC-BSC simulations. We remark that the simulation time of each location (based on NEC-BSC) was approximately 139 min using a 1.6 GHz central processing unit (CPU) machine.

2.3. Validation results

As is expected, one-to-one mapping of indoor propagation measurements to simulations is rarely achieved. As such, one can explore a stochastic way of validating the measurement and simulation data [16]. Specifically, we compared the time-domain multipath channel parameters such as mean excess delay and root mean square (RMS) delay spread [17]. These parameters are useful in describing the overall characteristics of the multipath profile and are essential in developing design guidelines for digital wireless communication systems. These channel parameters are easily extracted from the power delay profiles (PDPs). To obtain the PDP at a given receiver location, the 1601 CW tones are transformed to the time domain via an inverse fast Fourier transform (IFFT) procedure. Therefore, each of the 18 measuring locations (see Figure 2) is associated with a PDP and a set of multipath channel parameters. Of particular importance is the RMS delay spread (σ), which equals to the square root of the second moment of the PDP [17]. This is an indicator of the maximum data rate in the wireless channel and is also directly related to the performance degradation caused by intersymbol interference (ISI). Given the importance of RMS delay spread, we used this parameter for comparing the measured and calculated data. As 18 measuring locations were considered here, we built a cumulative distribution function (CDF) for the RMS delay spread values. Figure 4 shows the measured and simulated RMS delay spread CDFs. Clearly, there is a good agreement between

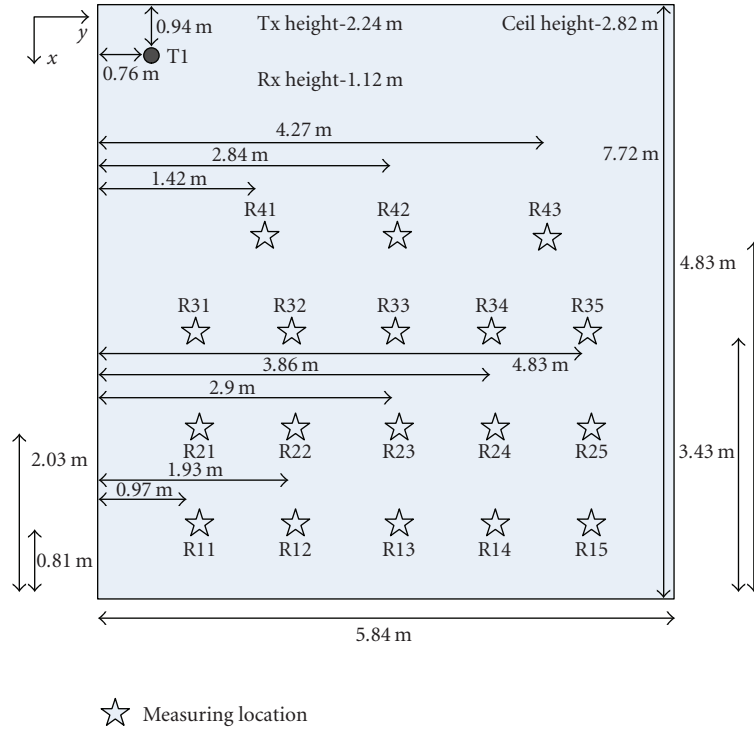


FIGURE 2: The positions of the 18 measuring locations and the transmitting location, all within the classroom of dimensions, length 7.72 m, width 5.84 m, and height 2.82 m.

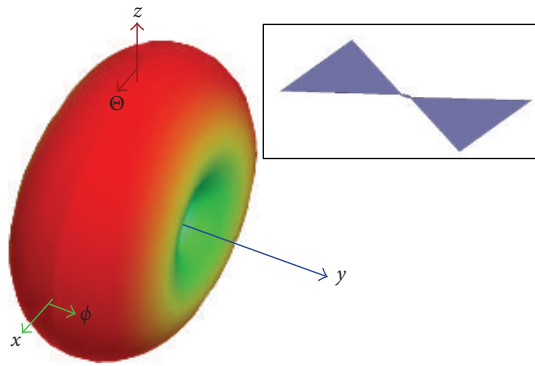


FIGURE 3: Ansoft HFSS simulation of the bow-tie antennas that were used for our in-house measurements; on the left is the antenna pattern and on the right is the bow-tie antenna HFSS model.

measurements and simulations, indicating that the NEC-BSC can be employed for predicting the multipath channel parameters. As we know, NEC-BSC was formulated based on UTD concepts which are particularly ideal for high-frequency simulations. As such, one would anticipate when the ray-tracing modeling was appropriate at 2-3 GHz, it would also be valid at 60 GHz propagation modeling (since NEC-BSC employs high-frequency asymptotic approximations). Next, we proceed with a study at 60 GHz based on the NEC-BSC.

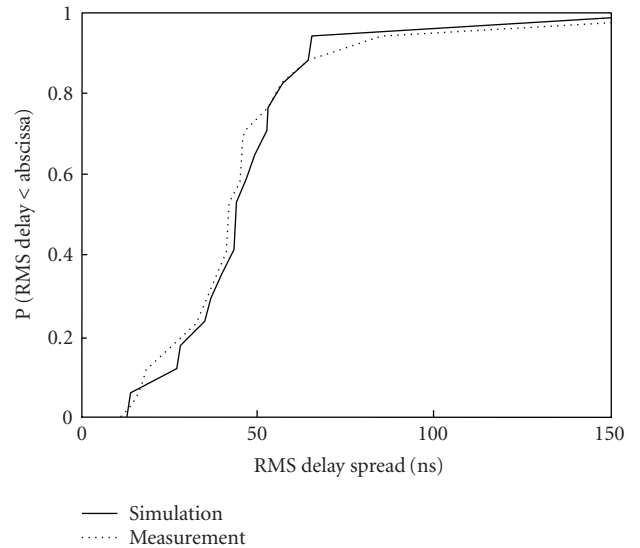


FIGURE 4: Comparison of measured and simulated RMS delay spread CDFs in the empty room; the solid line denotes the RMS delay spread obtained from our simulations; the dotted line represents the measured RMS delay spread.

3. MODELING OF ROOM AND HALLWAY

For our 60 GHz propagation studies, of particular interest was the effect of wall configuration on the channel parameters and the fading statistics. Thus, we considered two

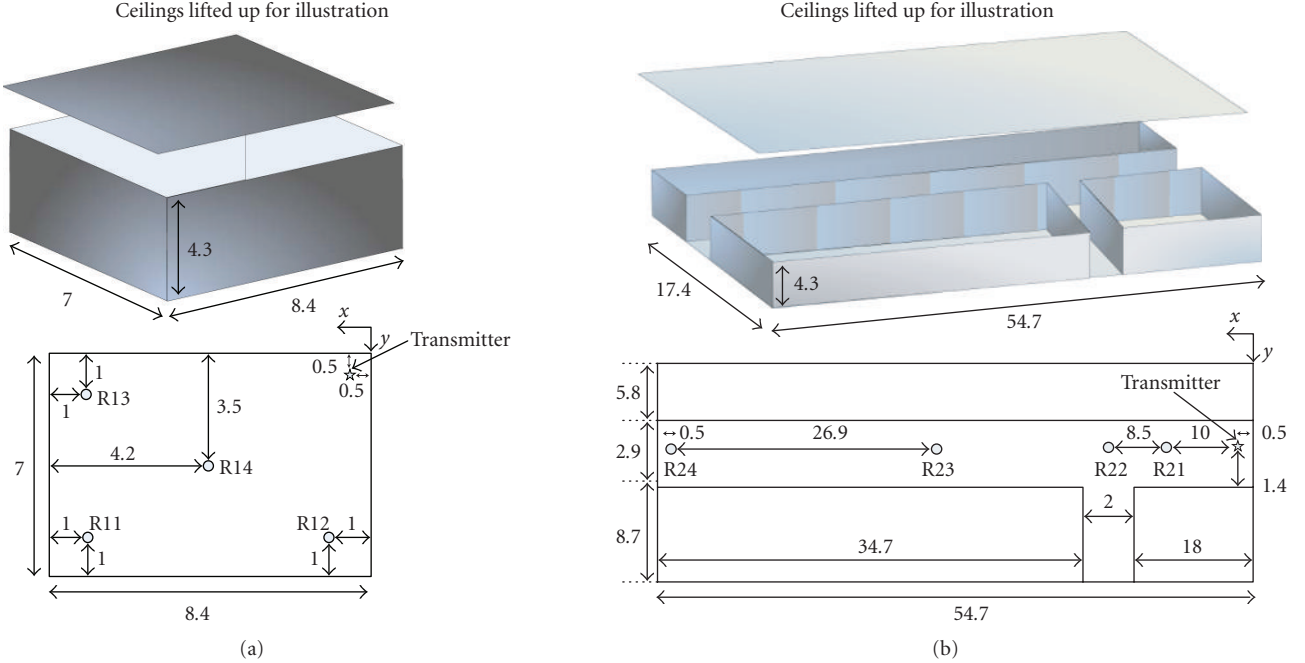


FIGURE 5: (a) 3D view of the room and its floorplan used for the 60 GHz simulations. (b) 3D view of the hallway and its floorplan. (All dimensions are in m.)

configurations: (1) a room and (2) a hallway. The dimensions of the room are depicted in Figure 5(a) and the dimensions of the hallway are depicted in Figure 5(b). The room has length 8.4 m, width 7.0 m, and height 4.3 m, whereas the hallway has length 54.7 m, width 2.9 m, and height 4.3 m. The walls, floor, and ceiling are 14.5 cm thick characterized by a relative dielectric $\epsilon_r = 4.22 - j0.02$. For propagation analysis, we chose a horn antenna as the transmitter with a theoretical half power beamwidths (HPBW) of 12° in azimuth and 9.5° in elevation. The receiving antennas were considered to have a donut antenna pattern (as shown in Figure 3). We remark that all receiver positions had a line-of-sight (LOS) path to the transmitter. Specifically, four receiving locations for both the room and hallway, namely, R11-R14 and R21-R24 were sampled (see Figure 5). At these locations, channel parameters and fading statistics were extracted as described in Section 4.

For the simulations, the NEC-BSC was set to analyze the propagation response using 1601 continuous wave (CW) tones evenly spaced between 59 GHz and 61 GHz, which results in a frequency sweep with 1.25 MHz steps. As a result, the frequency resolution had a maximum excess delay of about 166.66 ns and a temporal resolution of 500 ps (because of 2 GHz bandwidth). In the simulations, the direct and reflected rays up to tenth and seventh order from the walls, ceiling, and floor were included for the room and hallway, respectively. Here, our interest is the extraction of the multipath channel parameter (i.e., RMS delay spread). As such, the 1601 CW tones are transformed to time domain to obtain the channel response (i.e., PDP) at each receiver location. We note that the simulation times for each receiving location are approximately 67 min and 142 min for the

TABLE 1: RMS delay spread of room and hallway as shown in Figure 5.

Rx location	Room σ [ns]	Rx location	Hallway σ [ns]
R11-(7.4,6.0,1.6)	31.20	R21-(44.2,10.1,1.6)	58.15
R12-(1.0,6.0,1.6)	24.85	R22-(35.7,10.1,1.6)	65.32
R13-(7.4,1.0,1.6)	51.28	R23-(27.4,10.1,1.6)	51.88
R14-(4.2,3.5,1.6)	36.26	R24-(54.2,10.1,1.6)	57.44

room and hallway, respectively, using a 1.6 GHz CPU machine.

4. CHANNEL PARAMETERS AND FADING MODEL

Next, we proceed to extract the multipath channel parameter (i.e., RMS delay spread σ) at 60 GHz. Table 1 shows the RMS delay spread at the various receiving locations for both the room and the hallway. When the receiving antenna is placed at different locations, the delay spread ranges from 24.85 ns to 51.28 ns for the room and from 51.88 ns to 65.32 nsec for the hallway. The simulated delay spreads are in agreement with the measurement results in [8]. In the case of [8], the delay spreads for indoor 60 GHz channels range from 15 ns to 45 ns for small rooms and between 30 ns and 70 ns for large indoor environments. This also implies that the ray-tracing method can be used to predict the multipath channel parameters at the mm-wave frequencies.

As is well known, indoor propagation involves interactions among furniture, walls, or other objects. Because of

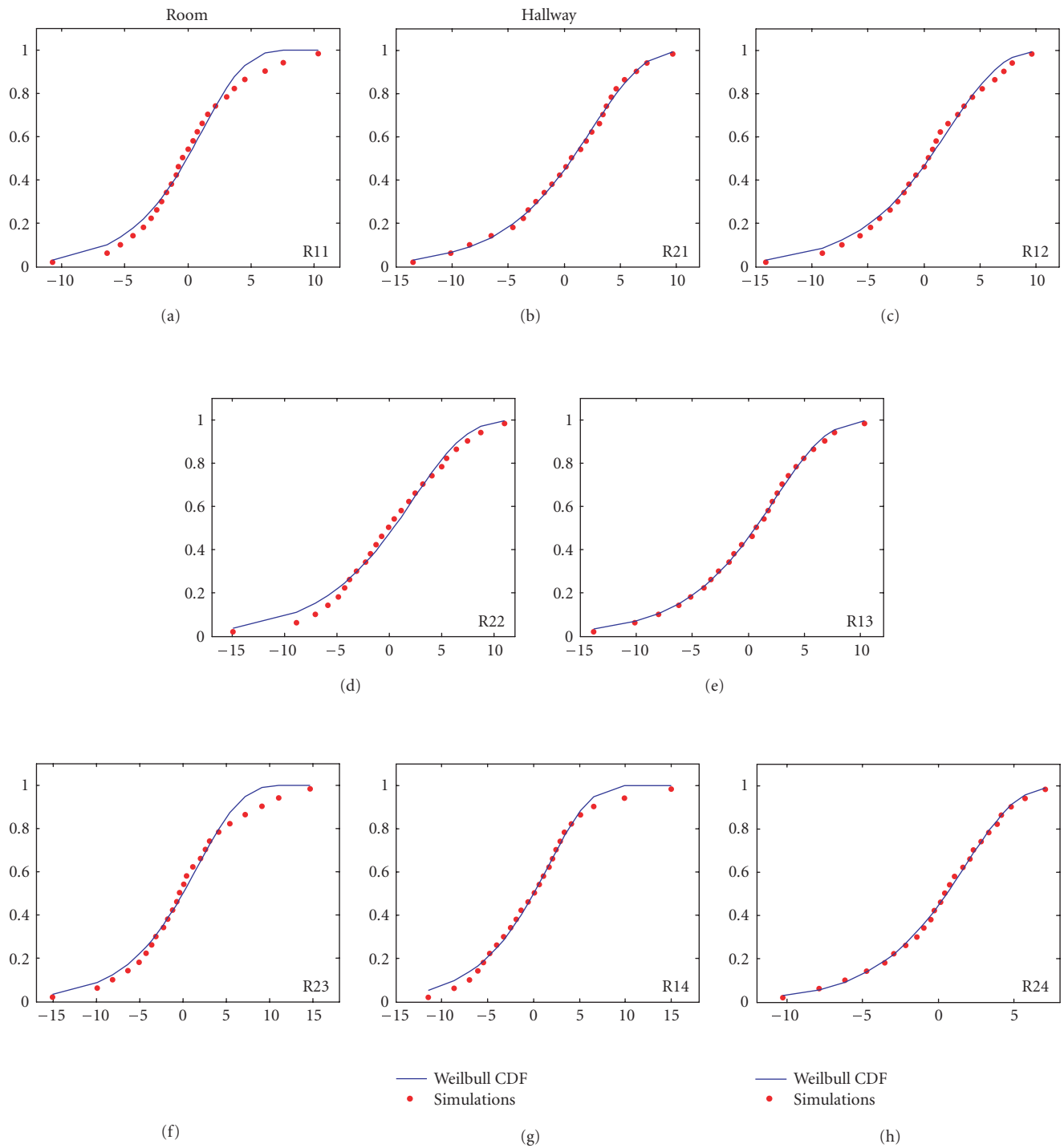


FIGURE 6: Cumulative distributive function (CDF) computed from the received power over mean power in Figure 5. The dots are CDF of the simulations of received power over mean power at R11-R14 and R21-24 and the depicted solid lines come from the best-fitted Weibull distribution.

these multipath, signals arrive at the receiver with different phases, causing fading. This fading can be obtained statistically from the PDPs by first developing a cumulative distributive function (CDF) based on the probability of receiving energies above a predetermined threshold level. Next, we

look for the best-fit distribution for the observed CDF (by means of maximum likelihood estimation). In this analysis, we chose the Weibull distribution (which has also been used for ultra-wideband indoor propagation [18]) for fitting the data. The Weibull probability density function can

be written as

$$p(r) = \begin{cases} ba^{-b}r^{b-1} \exp\left(-\frac{r}{a}\right)^b & \text{for } 0 \leq r \leq \infty \\ 0 & \text{for } r < 0, \end{cases} \quad (1)$$

where a and b , respectively, are the scale and the shape parameters chosen to fit the simulations.

To check the fitting of the observed and estimated Weibull data, we performed a null hypothesis testing, H_0 : (observed data = fitted Weibull) versus the alternative hypothesis H_A : (observed data \neq fitted Weibull) by using the Kolmogorov-Smirnov (KS) goodness-of-fit test. To ensure a good fit within a reasonable tolerance, the *significant level* was kept within 5%. In both the room and the hallway studies, it is clearly shown in Figure 6 that the CDFs at receiving locations (i.e., R11-R14 and R21-R24) have a good agreement with the Weibull distribution. We remark that the fitness of our simulations to other CDFs, specifically the Rayleigh CDF, can be found in [19, 20].

5. CONCLUSION

Based on the 3D ray-tracing method, we extracted statistical parameters (i.e., RMS delay spread) for indoor site-specific environments of different configurations. We found that the fading statistics of these indoor environments were characterized by a Weibull distribution. Accurate prediction of such statistics is vital in determining the channel capacity, and this has been shown in [21]. In conclusion, it has been demonstrated that the ray-tracing methods can be used for channel parameter extractions, particularly at 60 GHz band.

ACKNOWLEDGMENTS

The authors would like to thank the editor and the anonymous reviewers for their valuable comments and suggestions.

REFERENCES

- [1] P. Smulders, "Exploiting the 60 GHz band for local wireless multimedia access: prospects and future directions," *IEEE Communications Magazine*, vol. 40, no. 1, pp. 140–147, 2002.
- [2] H. Xu, V. Kukshya, and T. S. Rappaport, "Spatial and temporal characteristics of 60-GHz indoor channels," *IEEE Journal on Selected Areas in Communications*, vol. 20, no. 3, pp. 620–630, 2002.
- [3] T. Manabe, Y. Miura, and T. Ihara, "Effects of antenna directivity and polarization on indoor multipath propagation characteristics at 60 GHz," *IEEE Journal on Selected Areas in Communications*, vol. 14, no. 3, pp. 441–448, 1996.
- [4] A. M. Hammoudeh and G. Allen, "Millimetric wavelengths radiowave propagation for line-of-sight indoor microcellular mobile communications," *IEEE Transactions on Vehicular Technology*, vol. 44, no. 3, pp. 449–460, 1995.
- [5] S. Collonge, G. Zaharia, and G. El Zein, "Influence of the human activity on wide-band characteristics of the 60 GHz indoor radio channel," *IEEE Transactions on Wireless Communications*, vol. 3, no. 6, pp. 2396–2406, 2004.
- [6] F. Giannetti, M. Luise, and R. Reggiannini, "Mobile and personal communications in the 60 GHz band: a survey," *Wireless Personal Communications*, vol. 10, no. 2, pp. 207–243, 1999.
- [7] S. K. Yong and C. C. Chong, "An overview of multi-gigabit wireless through millimeter wave technology: potentials and technical challenges," to appear in *EURASIP Journal on Wireless Communications and Networking*.
- [8] P. F. M. Smulders and L. M. Correia, "Characterisation of propagation in 60 GHz radio channels," *Electronics and Communication Engineering Journal*, vol. 9, no. 2, pp. 73–80, 1997.
- [9] A. Hammoudeh, D. A. Scammell, and M. G. Sánchez, "Measurements and analysis of the indoor wideband millimeter wave wireless radio channel and frequency diversity characterization," *IEEE Transactions on Antennas and Propagation*, vol. 51, no. 10 II, pp. 2974–2986, 2003.
- [10] N. Moraitis and P. Constantinou, "Indoor channel measurements and characterization at 60 GHz for wireless local area network applications," *IEEE Transactions on Antennas and Propagation*, vol. 52, no. 12, pp. 3180–3189, 2004.
- [11] T. Zwick, T. J. Beukema, and H. Nam, "Wideband channel sounder with measurements and model for the 60 GHz indoor radio channel," *IEEE Transactions on Vehicular Technology*, vol. 54, no. 4, pp. 1266–1277, 2005.
- [12] R. J. Marhefka, "Numerical electromagnetics code - basic scattering code (NEC-BSC Version 4.2), User's Manual," Tech. Rep. (Preliminary), ElectroScience Laboratory, The Ohio State University, Columbus, Ohio, USA, October 2000.
- [13] R. G. Kouyoumjian and P. H. Pathak, "A uniform geometrical theory of diffraction for an edge in a perfectly conducting surface," *Proceedings of the IEEE*, vol. 62, no. 11, pp. 1448–1461, 1974.
- [14] P. H. Pathak, W. D. Burnside, and R. J. Marhefka, "A Uniform GTD analysis of the diffraction of electromagnetic waves by a smooth convex surface," *IEEE Transactions on Antennas and Propagation*, vol. 28, no. 5, pp. 631–642, 1980.
- [15] A. H. Muqaibel, "Characterization of ultra wideband communication channels," Ph.D. dissertation, Virginia Polytechnic Institute and State University, Blacksburg, Va, USA, 2003.
- [16] C.-C. Chong, Y.-E. Kim, S. K. Yong, and S.-S. Lee, "Statistical characterization of the UWB propagation channel in indoor residential environment," *Wireless Communications and Mobile Computing*, vol. 5, no. 5, pp. 503–512, 2005, special issue on Ultrawideband for Wireless Communications.
- [17] T. S. Rappaport, *Wireless Communications: Principles and Practice*, Prentice-Hall, Upper Saddle River, NJ, USA, 1996.
- [18] C.-C. Chong and S. K. Yong, "A generic statistical-based UWB channel model for high-rise apartments," *IEEE Transactions on Antennas and Propagation*, vol. 53, no. 8, part 1, pp. 2389–2399, 2005.
- [19] R. J.-M. Cramer, R. A. Scholtz, and M. Z. Win, "Evaluation of an ultra-wide-band propagation channel," *IEEE Transactions on Antennas and Propagation*, vol. 50, no. 5, pp. 561–570, 2002.
- [20] C.-P. Lim, R. J. Burkholder, J. L. Volakis, and R. J. Marhefka, "Propagation modeling of indoor wireless communications at 60GHz," in *Proceedings of IEEE AP-S International Symposium and USUC/URSI National Radio Science Meeting and AMEREM Meeting*, pp. 2149–2152, Albuquerque, NM, USA, July 2006.
- [21] C.-P. Lim, J. L. Volakis, K. Sertel, R. W. Kindt, and A. Anastasopoulos, "Indoor propagation models based on rigorous methods for site-specific multipath environments," *IEEE Transactions on Antennas and Propagation*, vol. 54, no. 6, pp. 1718–1725, 2006.

Research Article

Channel Characteristics and Transmission Performance for Various Channel Configurations at 60 GHz

Haibing Yang, Peter F. M. Smulders, and Matti H. A. J. Herben

Department of Electrical Engineering, Eindhoven University of Technology, P.O. Box 513, 5600 MB Eindhoven, The Netherlands

Received 13 June 2006; Accepted 20 March 2007

Recommended by Chia-Chin Chong

Extensive measurements are conducted in room environments at 60 GHz to analyze the channel characteristics for various channel configurations. Channel parameters retrieved from measurements are presented and analyzed based on generic channel models. Particularly, a simple single-cluster model is applied for the parameter retrieval and performance evaluation. By this model, power delay profiles are simply described by a K -factor, a root-mean-squared delay spread, and a shape parameter. The considered channels are configured with the combination of omnidirectional, fan-beam, and pencil-beam antennas at transmitter and receiver sides. Both line-of-sight (LOS) and non-LOS (NLOS) channels are considered. Further, to evaluate the transmission performance, we analyze the link budget in the considered environments, then design and simulate an OFDM system with a data rate of 2 Gbps to compare the bit-error-rate (BER) performance by using the measured and modeled channels. Both coded and uncoded OFDM systems are simulated. It is observed that the BER performance agrees well for the measured and modeled channels. In addition, directive configurations can provide sufficient link margins and BER performance for high data rate communications. To increase the coverage and performance in the NLOS area, it is preferable to apply directive antennas.

Copyright © 2007 Haibing Yang et al. This is an open access article distributed under the Creative Commons Attribution License, which permits unrestricted use, distribution, and reproduction in any medium, provided the original work is properly cited.

1. INTRODUCTION

In recent years, intensive efforts have been made worldwide for the application of high data rate wireless communication system in the frequency band of 60 GHz [1–5]. Special features of the radio propagation in this frequency band, namely high penetration loss of construction materials and severe oxygen absorption, and broadband spectrum (common bands of 59–62 GHz worldwide) make it suitable for the deployment of high data rate short-distance communications [3, 6]. Recently, the IEEE 802.15.3 Task Group 3c was formed to standardize the 60 GHz wireless personal area network (WPAN) systems, which will allow high data rate up to 3 Gbps [5]. Even higher data rate requirements would be expected in the future. The low-cost and low-complexity implementation of such systems requires a suitable channel model for the characteristics of the 60 GHz radio propagation, which can be used for the codesign of RF front-end and baseband processing. To this end, this paper will focus on channel modelling, model parameter retrieval, and system performance evaluation over 60 GHz channels.

One of the biggest challenges for designing a high data-rate 60 GHz system is the limited link budget due to high path loss during radio propagation [3, 5–7]. For a fixed separation between transmitter (TX) and receiver (RX), the propagation loss at 60 GHz is about 30 dB higher than at 2 GHz in free space. In this sense, it is preferable to employ high-gain directive antennas, especially for a fixed point-to-point application. Thanks to the relatively small dimensions of 60 GHz antennas, an alternative to high-gain antennas is to use highly flexible antenna arrays for adaptive beamforming. On the other hand, an omnidirectional antenna might be used in some applications where a full coverage is required.

For most 60 GHz applications, the transmitter and the receiver will keep stationary, and the time variation of the channel will be introduced by moving objects due to the Doppler effect. In particular, the movements of human bodies within the channel will cause significant temporal fading and shadowing effect, whose level depends on the moving speed, the number of persons, and the propagation environment [8–10]. The remaining significant impact on the system caused by the radio channel is the frequency selectivity due

to multipath effect, which induces intersymbol interference (ISI) in communication systems [11–14].

Multipath propagation in indoor environments is strongly affected by the dimensions of the environment and the density of furnishings. The influence of the environment on the channel can be noticed in the power delay profile (PDP), which describes the span of the received signal over time delay. In a local area within a range of tens of wavelength, cluster-wise arrival behavior of scattered waves has been observed from measurements and the average PDP is formulated by multicluster models [15–19]. In a global area such as a room environment, the average PDP is exponentially decaying over delay in addition to the direct path [20, 21]. In this single cluster model, a constant-level part might appear before the decaying part caused by the elevation dependence of antenna radiation patterns and the height difference between the transmit antenna and the receive antenna [21]. The impact of various PDP shapes on system performance has been considered in [12, 22, 23]. There they conclude that as long as the root-mean-squared (RMS) delay spread of the PDP is small compared with the symbol duration, the profile shape has a negligible impact on system performance, but the performance is strongly influenced by the RMS delay spread.

The purpose of this paper is to analyze the 60 GHz channel characteristics and to evaluate the system performance for various channel configurations. Due to the simplicity and the directness of the relationship between RMS delay spread (RDS) and PDP, the simple single-cluster model is applied to retrieve model parameters from measurements and used to evaluate the system performance. The structure of this paper is as follows. In Section 2, we give an overview of the generic theory for radio channels. In Section 3, channel measurements will be described in indoor environments for various antenna configurations. Then, channel parameters are retrieved and analyzed from the measured data. Particularly, the shape parameters of power delay profiles are retrieved to distinguish the channel characteristics of various configurations. Next in Section 4, we analyze the link budget and then simulate an equivalent baseband OFDM system for 60 GHz radio applications. The coded/uncoded BER performance is evaluated and compared for the measured and modeled channels. The BER performance for various channel configurations is also analyzed. Finally, conclusions are given in Section 5.

2. INDOOR CHANNEL THEORY

In a typical indoor radio environment, over a distance of as short as half a wavelength, the magnitude of the received signal will be subject to a rapid variation by as much as tens of dBs. This variation of the received signal is called channel fading and is caused by the propagation of multipath waves in addition to the line-of-sight (LOS) wave. For the 60 GHz radio applications in indoor environments, it is highly likely that the receiver can only be used within a single room, for example, an open office, where the transmitter is located, due to high penetration loss caused by its construction materials.

In this case, the multipath waves are mainly the reflected or scattered waves from main objects such as the walls, furniture, the floor, the ceiling. In a local area, the rapid variation of the received signal envelope is called small-scale fading and can be characterized by a Rician distribution [1, 13, 24]. When there is no contribution from a specular path such as the LOS path, the fading becomes Rayleigh distributed. The local mean of the received signal also varies over distance but much less rapidly. This slower variation is caused by the furnishing and the structure of the room environment. When measured over distances of several hundred wavelengths, the slow variation is called large-scale fading that is highly dependent on the distance. The large-scale variation can be empirically characterized by two multiplicative terms: an exponentially decaying term over distance and a log-normal distributed term with the standard deviation highly dependent on the environment [1, 13, 25].

For a wideband transmission system, the complex low-pass impulse response of a Rician channel is modeled as a direct or strong specular path plus N independent Rayleigh fading paths and can be expressed by¹

$$h(t, \tau) = \alpha_0 e^{j\phi_0(t)} \delta(\tau - \tau_0) + \sum_{n=1}^N \alpha_n e^{j\phi_n(t)} \delta(\tau - \tau_n), \quad (1)$$

where $\alpha_0 e^{j\phi_0(t)}$ is the response of the direct or strong specular path which stays stationary in a local area, $\{N, \alpha_n, \phi_n, \tau_n\}$ are randomly time-varying variables: the number of multiple paths, the amplitude, phase, and arrival-time of the n th path, respectively. The time dependency of the channel is introduced by arbitrary movements of the transmitter, the receiver or other objects. Since the path number, the amplitude and the arrival-time are relatively static in a local area, the time dependency is omitted here. A Rician K -factor is usually used to characterize the Rician fading channel and defined as the ratio between the powers contributed by the steady path and the scattered paths, that is,

$$K = \frac{E\{|\alpha_0|^2\}}{2\sigma^2}, \quad (2)$$

where $2\sigma^2$ is the mean power of the scattered paths.

For physical channels, it is reasonable to assume that the channel statistic is stationary or quasistatic, that is, wide-sense stationary (WSS), within the time duration of one transmitted symbol or one data package. Moreover, signals coming via different paths will experience uncorrelated attenuations, phase shifts, and time delays, which is referred to as uncorrelated scattering (US). The assumption of WSSUS for physical channels has been experimentally confirmed and widely accepted in literature [9, 13, 24, 27–29]. Under the WSSUS assumption, the autocorrelation of the complex

¹ The assumption of Rayleigh fading for the nonspecular paths is supported by the indoor channel measurements given in [24, 26].

impulse response $h(t, \tau)$ will be only dependent on the time difference and satisfies

$$\begin{aligned} \phi_h(\Delta t; \tau_1, \tau_2) &= \frac{E\{h^*(t, \tau_1)h(t + \Delta t, \tau_2)\}}{\sqrt{E\{|h^*(t, \tau_1)|^2\}E\{|h(t + \Delta t, \tau_2)|^2\}}} \\ &= \phi_h(\Delta t, \tau_1)\delta(\tau_2 - \tau_1). \end{aligned} \quad (3)$$

Furthermore, the average power delay profile of the channel is defined as the autocorrelation function when $\Delta t = 0$,

$$P(\tau) = E\{|h(t, \tau)|^2\} = \sum_{n=0}^N E\{|\alpha_n|^2\}\delta(\tau - \tau_n) \quad (4)$$

which is the average of instantaneous power delay profiles in a local area. From the average power delay profile, the RDS σ_s can be defined by

$$\sigma_s = \sqrt{\sum_{n=0}^N P(\tau_n)(\tau_n - \bar{\tau})^2} \quad (5)$$

with the mean excess delay $\bar{\tau} = \sum_{n=0}^N \tau_n P(\tau_n)$, where it is assumed that $\sum_{n=0}^N E\{|\alpha_n|^2\} = 1$. RDS is generally used to characterize the time dispersion of the channel.

The equivalent complex channel frequency response $H(t, f)$ is written as

$$H(t, f) = \sum_{n=0}^N \alpha_n e^{j(\phi_n(t) - 2\pi\tau_n f)} \quad (6)$$

which is the Fourier transform of (1) over τ . Under the WS-SUS assumption, it can be shown that the frequency autocorrelation function of $H(t, f)$ does not depend on the specific frequency and can be written as

$$\begin{aligned} \phi_H(\Delta t; f_1, f_2) &= \frac{E\{H^*(t, f_1)H(t + \Delta t, f_2)\}}{\sqrt{E\{|H^*(t, f_1)|^2\}E\{|H(t + \Delta t, f_2)|^2\}}} \\ &= \phi_H(\Delta t, \Delta f) \end{aligned} \quad (7)$$

with $\Delta f = f_2 - f_1$, where $\phi_H(\Delta t, f)$ is the Fourier transform of $\phi_h(\Delta t, \tau)$. For $\Delta t = 0$, the resulting $\phi_H(\Delta f) \doteq \phi_H(0, \Delta f)$ represents the channel coherence level over the frequency separation Δf . The coherence bandwidth B_c is defined as the largest frequency separation over which the correlation $|\phi_H(\Delta f)|$ is not smaller than a level, for example, 0.5 or 0.9. The coherence bandwidth is a statistical measure in characterizing the frequency selectivity of a channel.

The transmission channel can vary over time due to Doppler effect caused by moving objects or moving antennas at the transmitter or receiver side, which results in a spectrum broadening. Compared to the dramatic phase change caused by Doppler effect, the amplitude and the incident angles stay quasistationary. When the receiver is moving at speed v , the phase of the n th path is generally modeled by [30, 31]

$$\phi_n(t) = \bar{\phi}_n + 2\pi \frac{f_c v}{c} t \cos \theta_n, \quad (8)$$

where $\bar{\phi}_n$ is the phase when the channel is static, f_c the carrier frequency, c the speed of light, and θ_n the angle between the moving direction and the incident direction. When the angles of arrival of the multipath components are uniformly distributed in all the directions in a horizontal plane, a ‘‘U’’-shape Doppler spectrum, that is well known as the classic 2D Clarke’s model, will appear [30, 31]. When a specular path exists in the channel, a spike will appear in the Doppler spectrum. The 2D model can be further extended to 3D models [32, 33], which might be suitable for indoor wave propagations.

For most applications of indoor 60 GHz radio systems, the transmitter and receiver are stationary and the time variations of the channel are actually caused by moving objects. Then, the phase of the n th path reflected at a moving object with the speed v becomes [34]

$$\phi_n(t) = \bar{\phi}_n + 4\pi \frac{f_c v}{c} t \cos \theta_n \cos \varphi_n, \quad (9)$$

where θ_n is the reflection angle of the path at the moving object and φ_n the angle between the direction of movement and the direction orthogonal to the reflecting surface. In a similar way, the Doppler shift caused by multiple moving objects can be expressed. The resulting Doppler spectrum will show a ‘‘bell’’ shape, which has been observed from measurements [8, 9, 28].

Proportional to the carrier frequency, the Doppler effects at 60 GHz are relatively severe. For instance, a moving object at a speed of 2 m/s can lead to a Doppler spread as large as 1.6 kHz. For a fixed application, Doppler effects caused by moving objects can be significantly reduced by employing directive antennas or smart antenna technologies, as long as the signal path is not blocked by objects. But for directive configurations, once the direct path is blocked by moving objects, the communication link can be completely lost [8, 35].

3. CHANNEL MEASUREMENTS AND ANALYSIS

In this section, statistical channel parameters are retrieved from channel measurements conducted in room environments and analyzed for various antenna configurations.

3.1. Description of environment and measurements

An HP 8510C vector network analyzer was employed to measure complex channel frequency responses. During measurement, the step sweep mode was used and the sweep time of each measurement was about 20 seconds. Channel impulse responses were obtained by Fourier transforming the frequency responses into time domain after a Kaiser window was applied with a sidelobe level of -44 dB. Three types of vertical polarized antennas with different radiative patterns, that is, omnidirectional, fan-beam, and pencil-beam antennas, were applied in our measurements. Parameters of these antennas, half power beamwidth (HPBW), and antenna gain, are listed in Table 1.

Two groups of measurements were conducted in room A and B separately on the 11th floor of the PT-building at

TABLE 1: Antenna parameters.

Type of antennas	Half power beamwidth ($^\circ$)		Gain (dBi)
	E-plane	H-plane	
Fan beam	12.0	70.0	16.5
Pencil beam	8.3	8.3	24.4
Omnidirectional	9.0	Omnidirectional	6.5

Eindhoven University of Technology. The plan view of the rooms are given in Figure 1. The dimensions of the rooms are $11.2 \times 6.0 \times 3.2 \text{ m}^3$ and $7.2 \times 6.0 \times 3.2 \text{ m}^3$, respectively. Both rooms have a similar structure. The windows side consists of window glasses with a metallic frame one meter above the floor and a metallic heating radiator below the window. The concrete walls are smoothly plastered and the concrete floor is covered with linoleum. The ceiling consists of aluminium plates and light holders. Some large metallic objects, such as cabinets, were standing on the ground. Note that in room A, three aligned metallic cabinets are standing in the middle of the room and two metallic cable boxes with a height of 3.2 m are attached to the brick wall side 2. The space between cabinets and ceiling has been blocked by aluminum foil for the ease of the measurement analysis.

Table 2 lists the measurement system configurations and scenarios. In room A, at both the transmitter and the receiver side, we use the same type of omnidirectional antennas. Three height differences of TX-RX were considered, namely, 0.0, 0.5, and 1.0 m (denoted by $OO_{0.0}$, $OO_{0.5}$, and $OO_{1.0}$ for three cases, resp.). Both LOS and non-LOS (NLOS) channels were measured in room A. In room B, a sectoral horn antenna with fan-beam pattern was applied at the TX side and located in a corner of the room at the height of 2.5 m. At the RX side, we used three types of antennas with omnidirectional, fan-beam, and pencil-beam patterns at the height of 1.4 m. The three TX/RX combinations are denoted by FO, FF, and FP, respectively, in which of the latter two cases the TX/RX beams are directed towards each other. In addition, we measured the channels for the cases of FF and FP with TX/RX beams misaligned by $\pm 35^\circ$ (denoted by $FF_{\pm 35^\circ}$ and $FP_{\pm 35^\circ}$). In room B, only LOS channels were measured.

During measurement, the transmitter and receiver were kept stationary and there were no movement of persons in the rooms.

3.2. Received power

The received power from a transmitter at a separation distance d is related to the path loss and can be represented by

$$P_r(d) = P_t + G_t + G_r - \text{PL}(d) \quad (10)$$

in decibels, where P_t is the transmit power, G_t and G_r are the antenna gains at transmitter and receiver side respectively. The path loss is usually modeled over the log-distance in the following:

$$\text{PL}(d) = \text{PL}_0 + 10n \lg(d) + X_\Omega \text{ (dB)}, \quad (11)$$

TABLE 2: Measurement scenarios and configurations.

Room	Freq. range (GHz)	Antenna (TX/RX)			Denoted
		TX	RX	Height (m)	
A	57 ~ 59	Omn.	Omn.	1.4/1.4	$OO_{0.0}$
				1.9/1.4	$OO_{0.5}$
				2.4/1.4	$OO_{1.0}$
B	58 ~ 59	Fan.	Omn.	2.5/1.4	FO
			Fan.		$FF, FF_{\pm 35^\circ}$
			Pen.		$FP, FP_{\pm 35^\circ}$

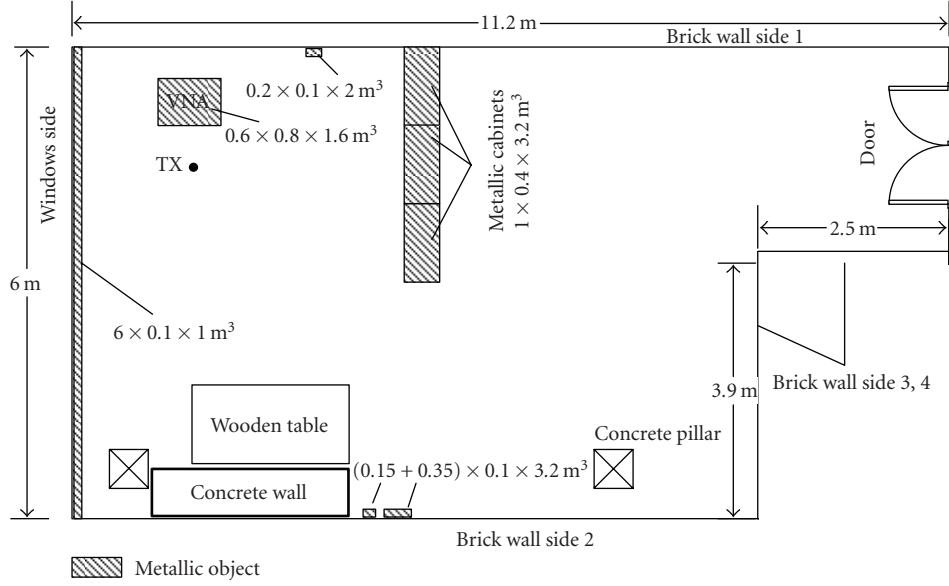
where PL_0 gives the reference path loss at $d = 1 \text{ m}$, n is the loss exponent, and X_Ω denotes a zero mean Gaussian distributed random variable with a standard deviation Ω . The standard deviation statistically describes the variation with respect to the mean path loss at a distance. Mostly, the model parameters in (11) are empirically derived by linearly fitting the measured path loss in dB over log-distance.

Figure 2 depicts the measured power level at the receiver for various antenna configurations when a unit power (0 dBm) is transmitted. The solid line shows the received power in free space.² Note that the abscissa axis is the travel distance of the first arrived wave, that is, the direct wave for the LOS case and the first reflected wave for the NLOS case. In this way, the scattered data can be better fitted by the log-distance model (11), since mostly the first arrived wave will have the most significant contribution to the received power. Apparently, the measured scattered data are widely scattered around the free-space curve for the omnidirectional configurations in Figure 2(a), due to the highly reflective environment. In contrast, for the directive antenna configurations in Figure 2(b), the power levels are much higher and the scattered points strongly follow the free space curve, except those points close to the transmitter that are very sensitive to the (unintentional) beam pointing errors.³ When the RX beams are misaligned intentionally by $\pm 35^\circ$ over the boresight, the received power by the Fan-Pen configuration will drop about 25 dB due to narrower antenna beam, compared to the 4 dB drop by the Fan-Fan one. Notice that the 35° -misalignment is about half the beamwidth of the fan-beam antenna and thus the direct path is still within the sight.

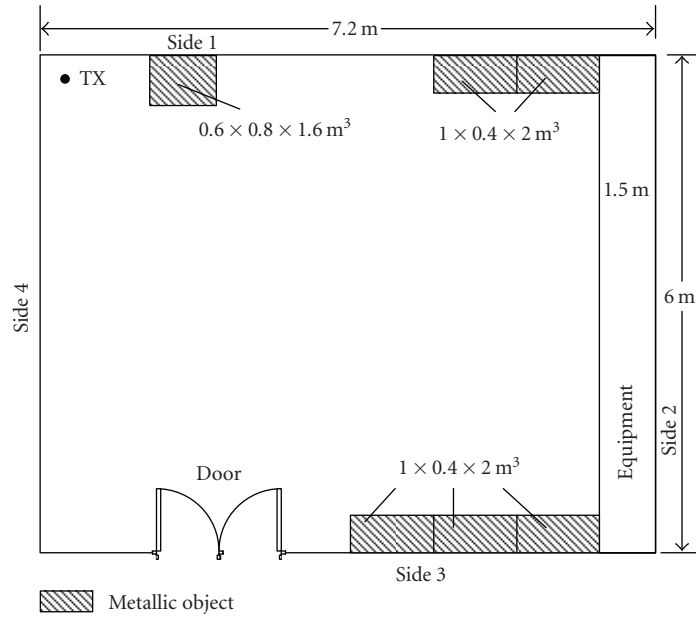
By fitting the measured data in Figure 2 to (11), we get the log-distance model parameters listed in Table 3. Here for the case of directive configurations in Figure 2(b), the scattered points within the distance of 2 to 3 meters are not considered during the fittings. It appears that the loss exponents are much smaller than the free-space exponent 2 for the Omn-Omn configurations, but approximately equal to 2 for the directive ones.

² The peak antenna gain is taken into account for the calculation of the received power in free space. For the NLOS scenario, the reflection loss over the wall is not taken into account for the calculation of the received power at the travel distance of the first reflected wave.

³ Notice that for the Fan-Omn case, when the transmitter and receiver are close to each other, the lower signal level is caused by the narrow beamwidth of the omnidirectional antenna in the vertical plane.



(a) Room A



(b) Room B

FIGURE 1: Plan view of the measured rooms.

3.3. K-factor, RDS, and coherence bandwidth

Figures 3 and 4 depict instantaneous *K*-factors and RMS delay spreads derived from the measured power delay profiles. Figure 4(c) shows a magnified version of Figure 4(b) so that the results can be well distinguished for directive configurations. In addition, we also estimated the coherence bandwidth $B_{c0.5}$ and $B_{c0.9}$ at the correlation level 0.5 and 0.9, respectively, as shown in Figure 5 for $B_{c0.5}$. The mean values of them are listed in Table 3 for each configuration. When calculating a *K*-factor, the power contributed by the

dominant path is derived by adding up the powers within the resolution bin of the dominant path. The RDS is calculated from the delay profile with a dynamic range fixed at 30 dB.

For the directive configurations of Fan-Fan and Fan-Pen, as the result of the significant suppression of multipath waves, it is observed that most of the channel parameters are in the region of $K > 10$, $\sigma_\tau < 1.5$ ns, $B_{c0.5} > 400$ MHz, and $B_{c0.9} > 40$ MHz, respectively. When the TX/RX beams are not pointing to each other, the beam-pointing errors, for example, the 35°-misalignment for the Fan-Pen configuration, can seriously worsen the channel condition in terms of

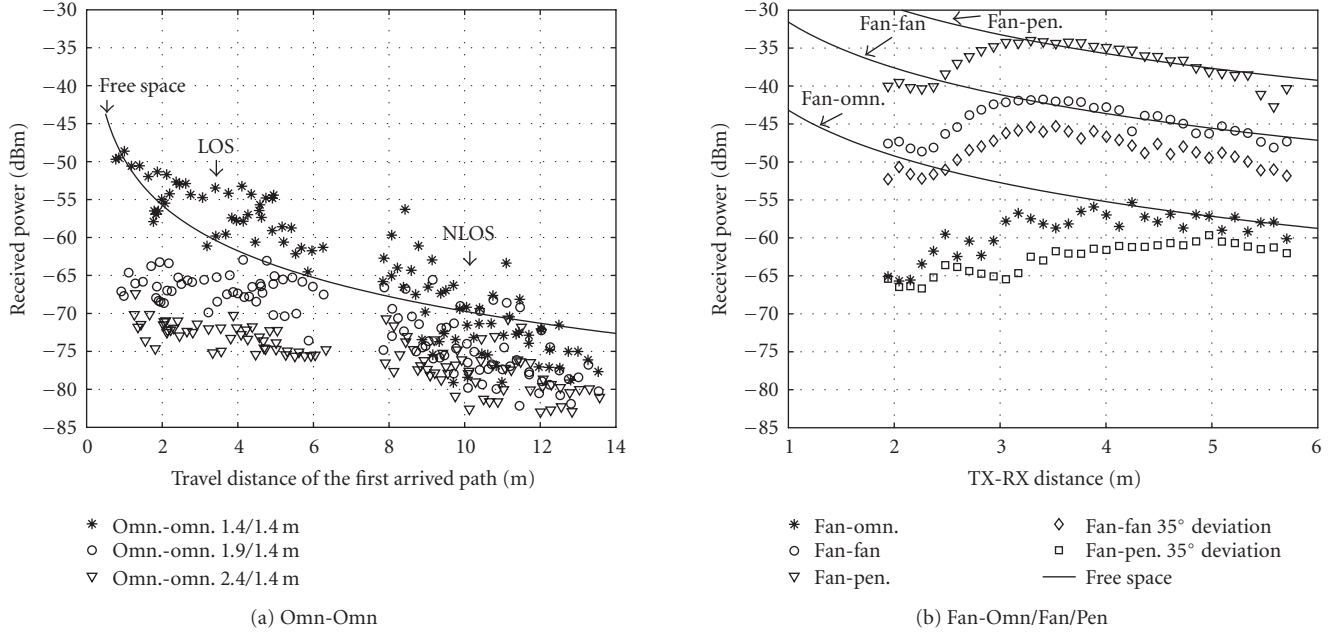


FIGURE 2: The received power over the travel distance of the first arrived path, when the transmit power is 0 dBm.

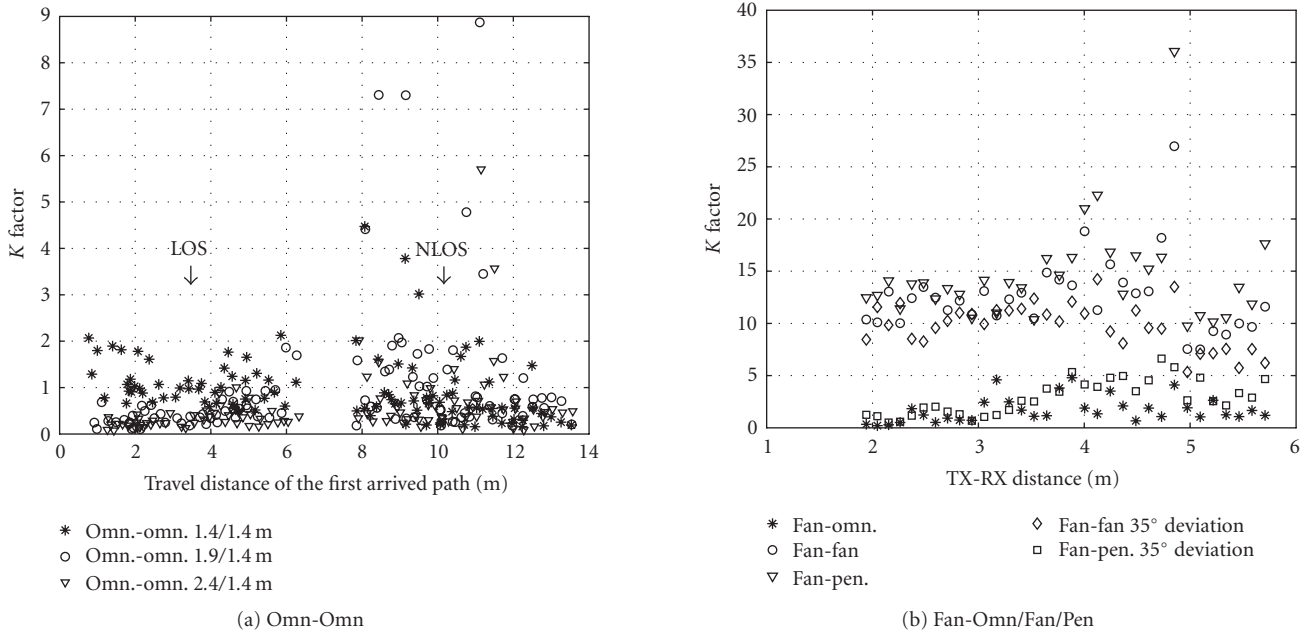


FIGURE 3: The measured instantaneous K -factor over the travel distance of the first arrived path.

large RDSs and the enormous drop of received powers, K -factors, and coherence bandwidth. This implies that channel configurations with wider beams are less sensitive for beam-pointing errors. In this case, the width of the beam has to be properly designed to prevent an enormous drop of channel quality caused by beam-pointing errors. In practice, multiple antennas can be deployed and beamforming algorithms will be used to achieve higher gain and suppress multipath effect

by steering the main beam to the direction of the strongest path.

When an omnidirectional antenna is used at TX or RX side, most of the channel parameters are in the region of $K < 3$, $\sigma_\tau > 5$ ns, $B_{c0.5} < 200$ MHz and $B_{c0.9} < 20$ MHz. The K -factors in the LOS case are generally small because of the highly reflective environment. Under the NLOS condition, channel parameters are strongly variant depending on the

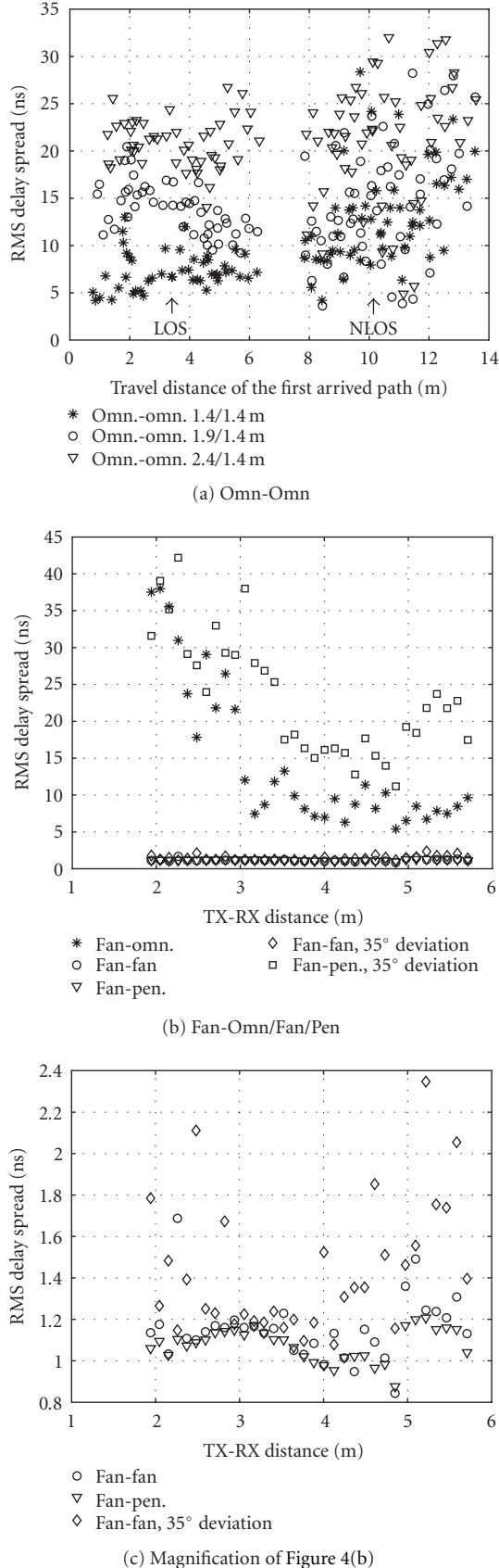


FIGURE 4: The instantaneous RMS delay spread over the travel distance of the first arrived path.

position of the receiver, due to the absence of the direct path. In some NLOS channels, a strong wave reflected from walls appears and leads to desirable values of channel parameters. In particular, the K -factors at some NLOS positions are larger than 4, since the strongest wave reflects at the metallic cable boxes attached to the wall and is much stronger than other reflected waves.

The coherence bandwidth is strongly related to the K -factor and the RDS, which embodies the Fourier transform relationship between the frequency autocorrelation function and the power delay profile described in Section 2. Generally speaking, the larger is the K -factor, the smaller is the RDS and thus the larger is the coherence bandwidth. For a specific shape of the power delay profile, one would expect a fixed relationship between coherence bandwidth and RDS [11]. From the measured data, we have found that for all the antenna configurations the coherence bandwidths at level 0.9 can be empirically related to the RDSs by $\sigma_\tau \cdot B_{c0.9} = 0.063$ [14], but the mean values of $\sigma_\tau \cdot B_{c0.5}$ are highly variant for different configurations.

3.4. Maximum excess delay and number of multipath components

Within the dynamic range of 30 dB of power delay profiles, the maximum excess delay τ_{\max} and the number of multipath components N are investigated for various measurement configurations. Multipath components are recognized from the local peaks in a profile. The values of τ_{\max} are distributed in different regions within 10 to 170 nanoseconds and so is the case for the values of N within 3 to 100, depending on the channel configurations. The mean values are summarized in Table 3. Also, the value of N is strongly related to the value of τ_{\max} , that is, the number of multipath components will increase with the maximum excess delay. For all the measured profiles, the number of paths per nanosecond, N/τ_{\max} , has a mean value of 0.30 with a small standard deviation of 0.06. This leads to an empirical relationship $N = \lceil 0.30 \cdot \tau_{\max} \rceil$.

3.5. Power delay profile shape

To investigate the shape of power delay profiles for various channel configurations, we take the average over all the measured profiles for each configuration. Here, each individual measured profile is normalized by its total received power. As an example, Figure 6 depicts the average profiles for the configurations of Omn-Omn and Fan-Pen. From these average profiles, we observe the following.

- (i) When the TX/RX beams are aligned to each other under the LOS condition, for example, the cases of Omn-Omn 1.4/1.4 m and Fan-Fan/Pen, the average delay profile consists of a direct ray and an exponentially decaying part.
- (ii) In other LOS cases when the TX/RX beams are strongly misaligned and out sight of each other, a constant level part will appear before an exponentially decaying part. The duration of the constant part depends on

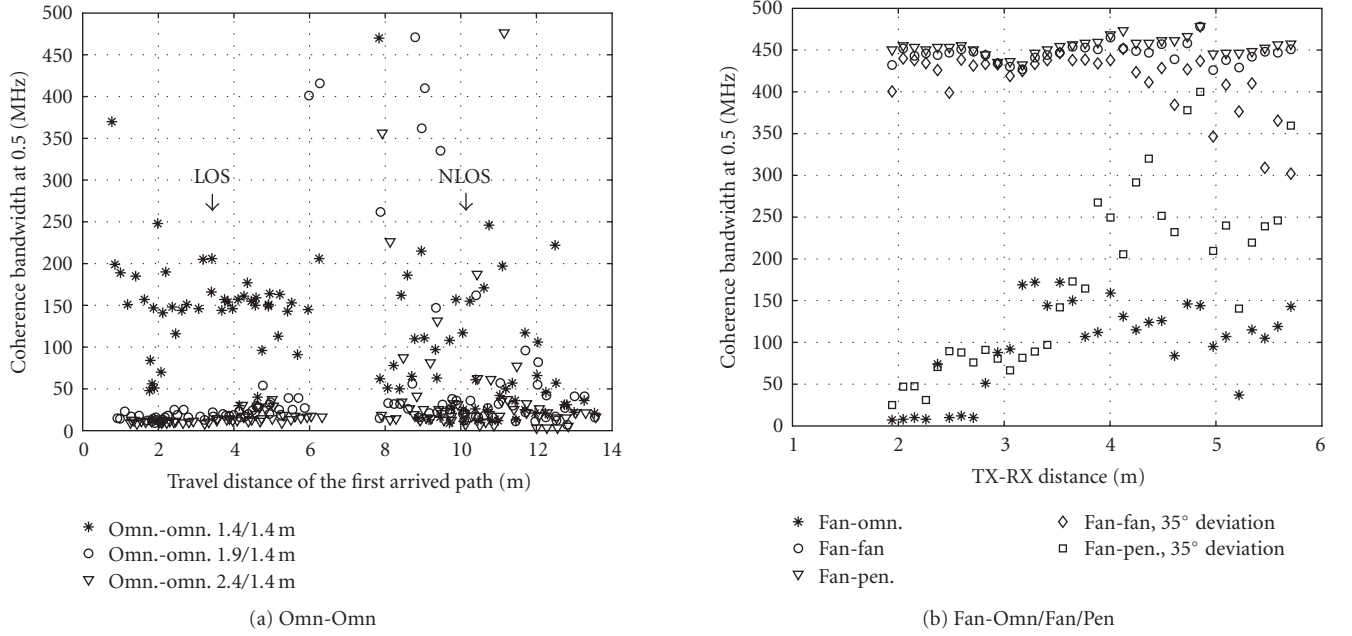


FIGURE 5: The coherence bandwidth at level 0.5 over the travel distance of the first arrived path.

TABLE 3: The log-distance model parameters $\{PL_0, n, \Omega\}$, the mean values of K , σ_τ , B_c , τ_{\max} , and N for various configurations, and the PDP shape parameters $\{s, \tau_c, \gamma\}$.

Cases	LOS			NLOS			LOS				
	OO _{0,0}	OO _{0,5}	OO _{1,0}	OO _{0,0}	OO _{0,5}	OO _{1,0}	FO	FF	FP	FF _{±35°}	FP _{±35°}
PL ₀ (dB)	68.3	83.8	87.8	34.8	56.7	71	79.7	67.0	67.4	72.2	115
n	1.2	0.2	0.6	5.4	3.8	2.7	0.4	2.1	2.0	1.9	-1.5
Ω (dB)	2.7	2.0	1.3	3.9	3.3	2.7	1.0	0.8	0.6	0.9	0.8
$E\{K\}$	1.1	0.5	0.3	0.9	1.6	0.7	1.7	12.5	14.5	9.8	2.9
$E\{\sigma_\tau\}$ (ns)	7.3	13.8	20.8	12.9	14.8	21.0	14.6	1.2	1.1	1.4	23.3
$E\{B_{c0,5}\}$ (MHz)	155.1	37.6	14.0	108.4	148.2	55.9	95.3	445.9	453.4	414.1	173.0
$E\{B_{c0,9}\}$ (MHz)	15.4	5.6	3.0	6.4	6.5	2.6	6.3	51.8	55.6	44.7	3.2
$E\{\tau_{\max}\}$ (ns)	67.8	116.6	144.8	120.6	133.4	146.1	113.2	15.7	15.4	21.5	141.7
$E\{N\}$	20.0	34.0	47.2	35.5	38.6	47.5	28.7	5.0	4.8	5.8	38.3
s (dB)	0	3.3	2.7	0	0	0	3.1	0	0	0	3.3
$E\{\tau_c\}$ (ns)	0	29.5	39.0	0	0	0	27.6	0	0	0	66.7
$E\{\gamma\}$ (dB/ns)	0.2	0.11	0.07	0.07	0.06	0.04	0.14	0.48	0.48	0.42	0.05

the extent of the misalignment and the beam pattern of the antenna.

- (iii) In addition, under the NLOS condition, the average delay profile will be exponentially decaying without a constant part, due to the lower dependency of antenna pattern and beam misalignment.

According to the observation, the average delay profile can be modeled as a function of excess delay that consists of a direct ray, a constant part, and a linear decaying part, as shown in Figure 6. This model was first proposed in [21] and further

developed in [36]. Mathematically, the power delay profile shape of a Rician channel is modeled by

$$P(\tau) = \begin{cases} 0, & \tau < 0, \\ |\alpha_0|^2 \delta(\tau), & \tau = 0, \\ \Pi, & 0 < \tau \leq \tau_c, \\ \Pi \cdot e^{-\gamma(\tau-\tau_c)}, & \tau > \tau_c, \end{cases} \quad (12)$$

where α_0 is the amplitude of the specular path, $\sqrt{\Pi}$ is the amplitude of the constant part with duration τ_c , and $\gamma = (A/10) \ln 10$ is the decay exponent with A in dB/ns. When the

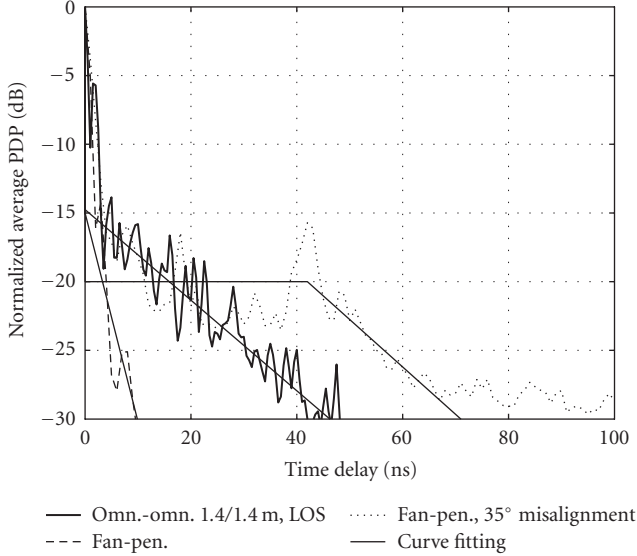


FIGURE 6: Average power delay profiles and curve fittings for the Fan-Omn/Fan/Pen configurations.

constant part disappears, that is, $\tau_c = 0$, it becomes the commonly applied exponentially decaying channel model. Letting $|\alpha_0|^2 = 0$, Rayleigh fading channels are described.

Since the duration τ_c is mainly affected by the narrow-beam antenna pattern and the beam misalignment, and the decay exponent γ is strongly related to a specific environment, particularly the reflection loss of walls, it is reasonable to assume that the product $\tau_c\gamma$ is fixed for a specific antenna configuration in an environment. Based on this assumption, to simplify this model, here we introduce a new parameter $s = \tau_c\gamma$ that defines the shape of a profile. When the shape parameter is known, the channel parameters $\{P, K, \sigma_\tau\}$, where P is the average channel power, can be related to the model parameters $\{|\alpha_0|^2, \Pi, \gamma, \tau_c\}$ as listed in Table 4. In the table, we have $s_1 = s + 1$, $s_2 = s^2/2 + s + 1$ and $s_3 = s^3/3 + s^2 + 2s + 2$.

From the measured results, the shape parameter s can be achieved by fitting the average PDP with (12) for each configuration. Then for each individual measured profile, the model parameters $\{|\alpha_0|^2, \Pi, \gamma, \tau_c\}$ can be retrieved by taking the channel parameters $\{P, K, \sigma_\tau\}$ into the channel-to-model formulas in Table 4. With these model parameters, the channel can be simulated and used for the performance evaluation of a system, as we will see in Section 4. Table 3 lists the shape parameters s and the mean values of the model parameters γ and τ_c for various configurations.

4. SYSTEM DESIGN AND BER PERFORMANCE EVALUATION

In this section, we analyze the link budget for designing a 60 GHz system and performs simulation of an OFDM system. Based on the simulated system, the BER performance is evaluated by using the measured and modeled channels.

4.1. Link budget and scenario analysis

Examining the link budget requirement for a radio system needs to determine the required signal strength at the receiver, that is, receiver sensitivity

$$P_{RX} = \frac{C}{N} + L_I + N_0 \text{ (dB)}, \quad (13)$$

where C/N stands for the required carrier-to-noise ratio for demodulation, L_I is the implementation loss of a transceiver and $N_0 = -174 + 10 \lg B + F$ is the thermal noise level in dB at a standard temperature 17° with B the bandwidth in Hz and F the noise figure. By knowing the receiver sensitivity and the received power at a distance d , one can examine the link margin $M = P_r(d) - P_{RX}$ to see whether the transmitted signal can be recovered properly.

For a coded OFDM system, a certain level of C/N is required in the receiver to achieve a proper demodulation and decoding for different constellations. Here, we take the minimum C/N level in Table 5 required for quasi-error-free reception in Rayleigh channels as a reference.⁴ The values are based on comprehensive system simulations and were computed on the assumption that the channel knowledge is perfectly known in the receiver [37]. For the considered OFDM system, the code rate is 3/4 and the guard interval is one-fourth of the useful symbol duration. If $L_I = 2.5$ dB, $B = 1.28$ GHz, and $F = 7$ dB, then one can readily calculate the receiver sensitivities as $P_{RX} = -62.7, -56.6, -51.5$ dBm for the constellations of QPSK, 16-QAM, and 64-QAM, respectively.

Next we examine possible constellations of the OFDM system for the channel configurations and environments described in Section 3. Given the transmitted power $P_t = 10$ dBm and the TX-RX separation $d = 6$ m, the mean received power $P_r(d)|_{d=6}$ can be predicted from (10) and the link margin can be determined. Table 5 lists the feasibility of the constellations for the LOS channels. In particular, for directive configurations, as long as the TX-RX beams are well aligned, the link margin is always larger than zero within a range of 6 meters for the three constellations and thus the channel bit rate up to 6 Gbps can be achieved. Actually, for the Fan-Fan and Fan-Pen configurations, the remaining link margins allow the radio coverage to be further extended. For the omnidirectional configuration with TX-RX antennas at the same height, the channel bit rate up to 4 Gbps is achievable by using 16-QAM. Additionally, by using QPSK to examine the NLOS channels, we observe that only half of the NLOS area can be covered by omnidirectional antennas. One would expect that the shadowing area can be fully covered if high gain directive antennas are applied.

⁴ Quasi-error-free reception means in the concatenated coding scheme Viterbi/Reed-Solomon, the bit-error-rate BER = 2×10^{-4} after Viterbi decoding and BER = 10^{-11} after Reed-Solomon decoding [37].

TABLE 4: Relation between model and channel parameters when the shape parameter s is known (see [36]).

model \rightarrow channel		channel \rightarrow model	
$s = \tau_c \gamma \in [0, \infty)$	$s = 0$	$s = \tau_c \gamma$	$s = 0$
$P = \alpha_0 ^2 + \frac{\Pi}{\gamma} s_1$	$P = \alpha_0 ^2 + \frac{\Pi}{\gamma}$	$ \alpha_0 ^2 = P \frac{K}{K+1}$	$ \alpha_0 ^2 = P \frac{K}{K+1}$
$K = \frac{ \alpha_0 ^2 \gamma}{\Pi s_1}$	$K = \frac{ \alpha_0 ^2 \gamma}{\Pi}$	$\gamma = \frac{1}{\sigma_\tau} \sqrt{\frac{1}{K+1} \frac{s_3}{s_1} - \frac{1}{(K+1)^2} \frac{s_2^2}{s_1^2}}$	$\gamma = \frac{1}{\sigma_\tau} \frac{\sqrt{2K+1}}{K+1}$
$\sigma_\tau = \frac{1}{\gamma} \sqrt{\frac{1}{K+1} \frac{s_3}{s_1} - \frac{1}{(K+1)^2} \frac{s_2^2}{s_1^2}}$	$\sigma_\tau = \frac{1}{\gamma} \frac{\sqrt{2K+1}}{K+1}$	$\Pi = \frac{P}{K+1} \frac{\gamma}{s_1}$	$\Pi = \frac{P}{K+1} \gamma$

TABLE 5: The required C/N and RX sensitivity for the 3/4 coded OFDM system with guard interval 1/4; the feasibility of modulation schemes for various configurations at a distance $d = 6$ meter in the LOS environments (\checkmark : yes; \times : no).

	QPSK	16-QAM	64-QAM
Minimum required C/N (dB)	10.7	16.7	21.7
RX sensitivity (dBm)	-62.7	-56.5	-51.5
Channel bit rate (Gbps)	2.0	4.0	6.0
Information bit rate (Gbps)	1.5	3.0	4.5
OO _{0.0}	\checkmark	\checkmark	\times
OO _{0.5}	\checkmark	\times	\times
OO _{1.0}	\times	\times	\times
FO, FF, FP, FF $_{\pm 35}$, FP $_{\pm 35}$	\checkmark	\checkmark	\checkmark

4.2. Baseband design and simulation of an OFDM system

To analyze the system performance of various channel configurations and evaluate the channel model (12) for the high data rate transmission, we simulate a coded OFDM system by using the measured and modeled channels. The baseband OFDM transmission scheme is depicted in Figure 7 and the system parameters are listed in Table 6. Before mapping to the QPSK symbols in the transmitter, the sequence of user bits undergoes a 3/4 convolutional punctured encoder and then a random interleaver in bit level. With the modulation of QPSK and the IFFT/FFT length of 1024, the coded data rate can reach 2 Gbps which is the target rate proposed by the IEEE 802.15.3c task group [5]. Here, the subcarrier spacing is 1.25 MHz and the guard interval is set to be 200 nanoseconds, which are large enough to prevent the possible inter-carrier-interference (ICI) caused by nonlinearities of the RF-frontend and to absorb the ISI between blocks caused by the multipath channel, respectively.

During the baseband simulation, the radio channels are implemented either by the measured impulse responses or the modeled impulse responses according to the delay profile model (12). For the modeled channels, the channel parameters of an individual realization, including K -factor, RDS, the shape parameter s , and the model parameters $\{|\alpha_0|^2, \Pi, \gamma, \tau_c\}$, are the same as those from the measured channels. Note that each delay profile is normalized to have a unit power. Additionally, the transmitter and the receiver

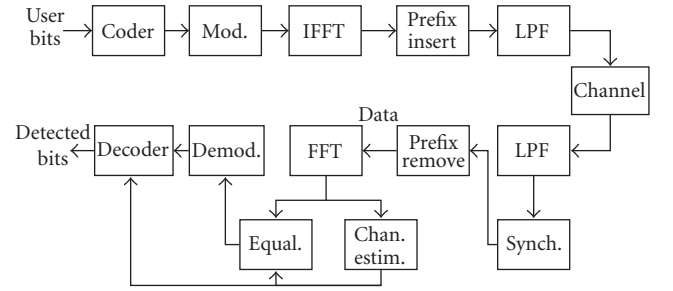


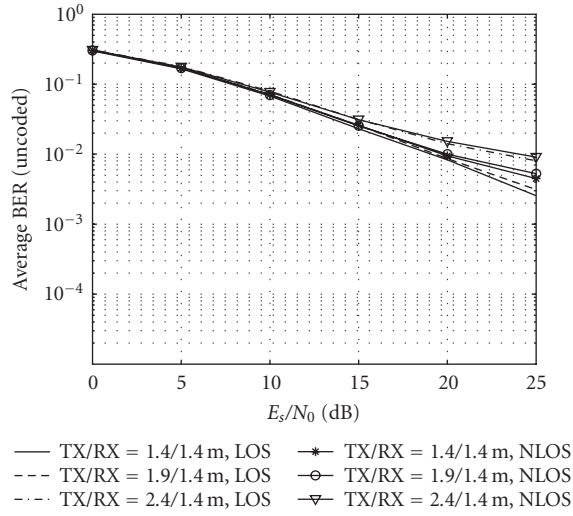
FIGURE 7: Baseband structure of a coded OFDM system.

TABLE 6: OFDM system parameters.

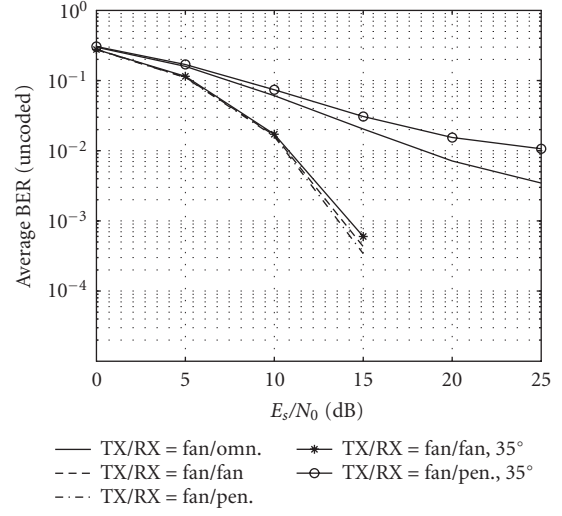
Carrier frequency	60 GHz
Modulation scheme	QPSK
Object moving speed	3 m/s
Channel bandwidth	1.28 GHz
Subcarrier number	1024
Subcarrier spacing	1.25 MHz
OFDM symbol duration	800 ns
Guard interval	200 ns
Code rate	3/4
Channel bit rate	2 Gbps
Information bit rate	1.5 Gbps

are considered to be stationary. But the time variation of the channel is caused by one moving object at speed 3 m/s and simulated according to the model (9). In the receiver, additive white Gaussian noise (AWGN) is added to the received signal. The nonlinearity effects, such as phase noise and IQ imbalance caused by the RF-frontend, are not included in the simulation.

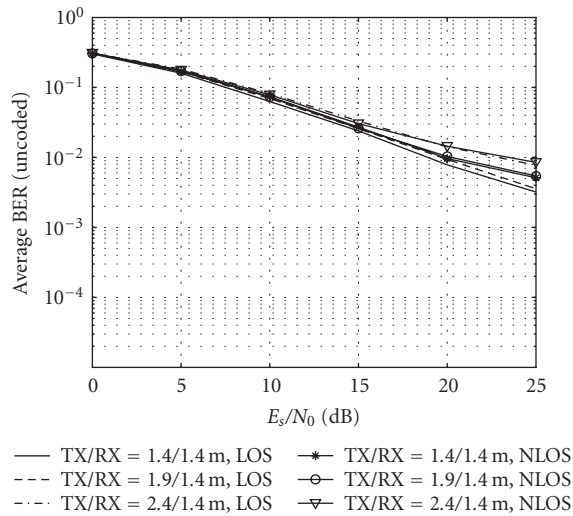
In the receiver, for the purpose of time synchronization, the received signal is correlated with a known training symbol to find the best starting point of an OFDM symbol. The training symbol is also used for the zero-forcing estimation of the channel response, which is applied for the one-tap symbol equalization before demodulation. The demodulator outputs the bitwise log-likelihood values for the alphabet of QPSK symbols, which are then used for the soft-decision



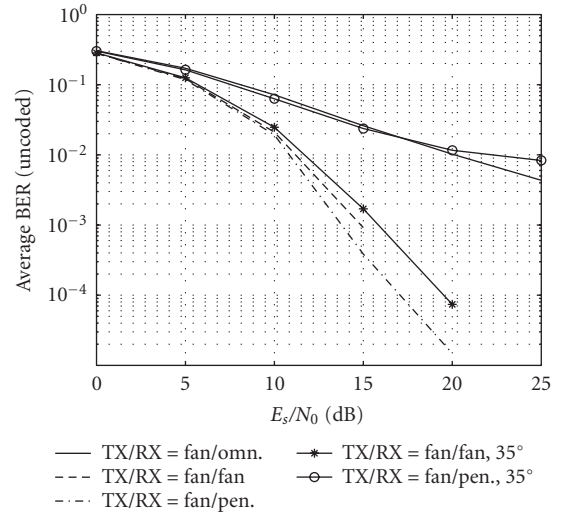
(a) Measured Omn-Omn channels



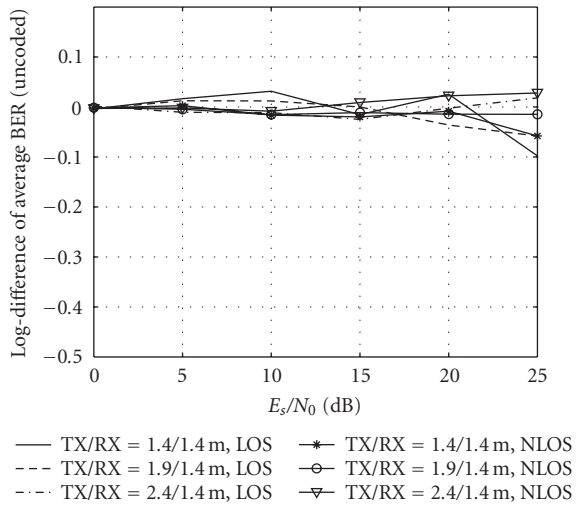
(b) Measured Fan-Omn/Fan/Pen channels



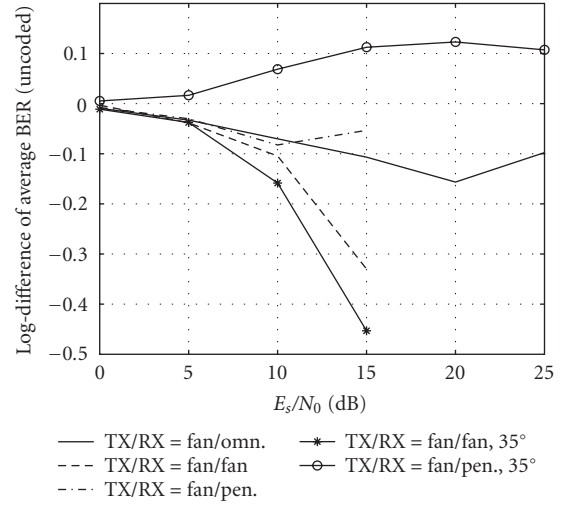
(c) Modeled Omn-Omn channels



(d) Modeled Fan-Omn/Fan/Pen channels

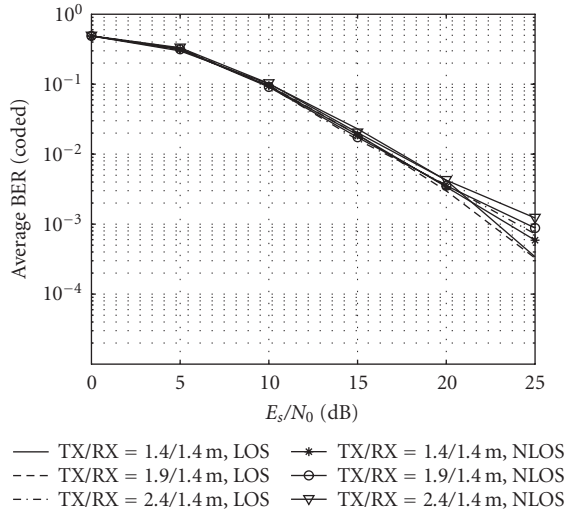


(e) Omn-Omn channels

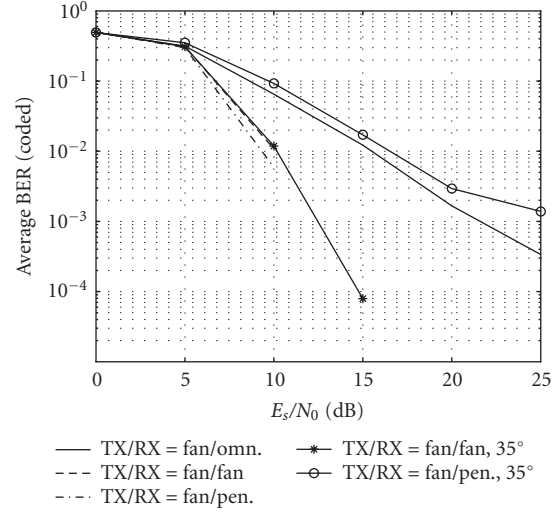


(f) Fan-Omn/Fan/Pen channels

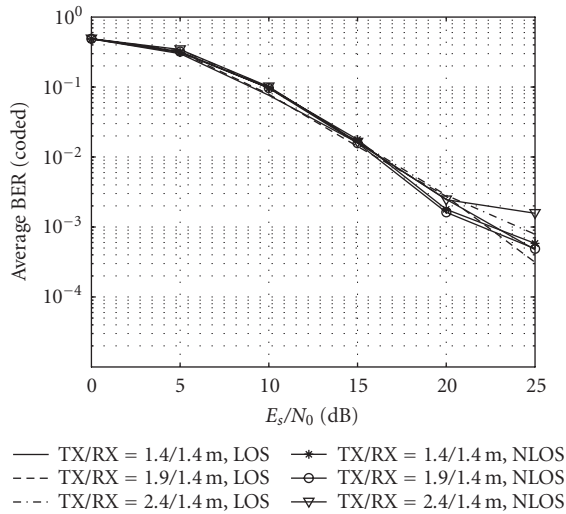
FIGURE 8: BER performance of uncoded OFDM system based on the measured and modeled channels and the log-difference of average BER between them.



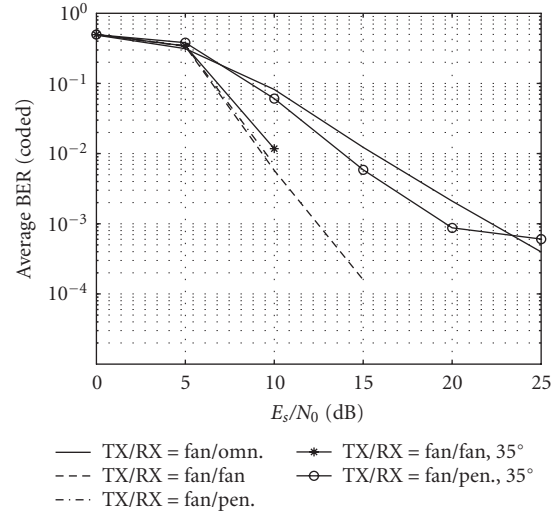
(a) Measured Omn-Omn channels



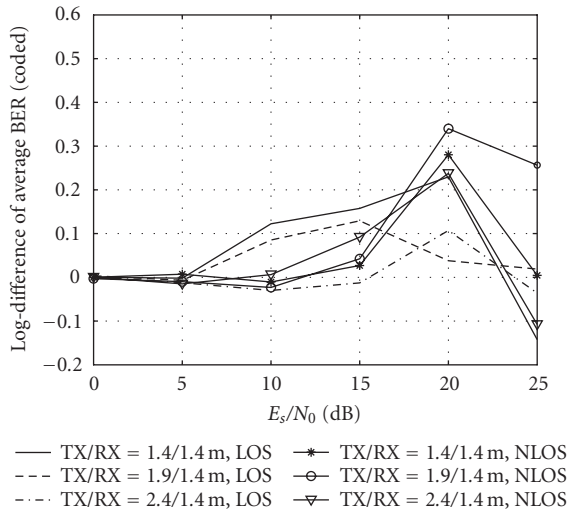
(b) Measured Fan-Omn/Fan/Pen channels



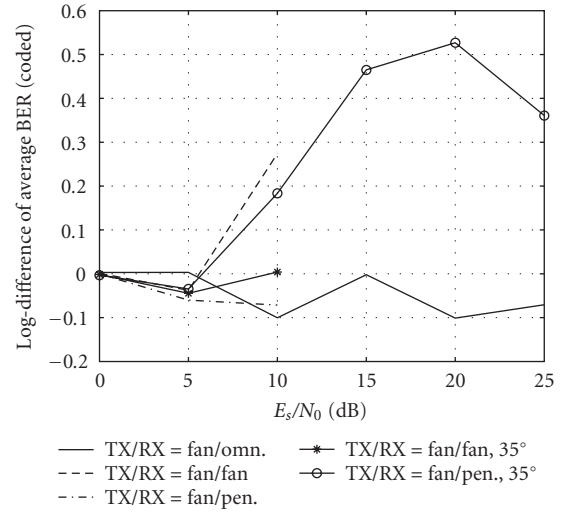
(c) Modeled Omn-Omn channels



(d) Modeled Fan-Omn/Fan/Pen channels



(e) Omn-Omn channels



(f) Fan-Omn/Fan/Pen channels

FIGURE 9: BER performance of coded OFDM system based on the measured and modeled channels and the log-difference of average BER between them.

Viterbi decoding. The simple channel estimation and equalization applied here are sufficient for a low-cost and low-complexity implementation of a 60 GHz system. There is no doubt that the system performance can be further improved by doing better channel estimation and equalization, which however will increase the implementation complexity.

4.3. BER performance analysis

The OFDM system described in Table 6 with and without coding is simulated and the BER performance is evaluated by using the measured and modeled channel impulse responses. For each set of model parameters $\{|\alpha_0|^2, \Pi, \gamma, \tau_c\}$, we conduct 200 runs of simulation.

Figures 8 and 9 depict the average uncoded- and coded-BER performance, respectively, over the receive C/N in terms of E_s/N_0 (energy per symbol divided by the noise density). In addition, the difference of average BER in logarithm domain between the measured and modeled channels is also shown in the figures for each antenna configuration. The BER performance is an average over the set of the possible channel responses with a specific TX/RX antenna configuration in one room. At high C/N , the BER event might be not well observed due to a limited number of sent bits, particularly for the directive channels, but this would not affect our analysis.

First of all, we observe that the log-differences of average BERs are in the ranges of $[-0.5, 0.1]$ and $[-0.1, 0.5]$ for the uncoded and coded performance, respectively. The small BER differences indicate that the BER curves show a similar performances for the measured and modeled channels for most antenna configurations. It is also important to notice that the modeled channels of Fan/Pen 35° show a more optimistic behavior than the measured ones in the uncoded- and coded-BER performance. This might be caused by the strong cluster behavior in the power delay profile as shown in Figure 6, which is not included in the single-cluster model (12). From these observations, we conclude that the statistical delay profile models according to (12) are well behaved and thus sufficient to evaluate the system performance for various channel configurations, as long as the channel does not show a strong multiple-cluster behavior.

Next for the uncoded BER performance, the Fan-Fan and Fan-Pen configurations achieve a similar performance if the TX-RX beams are well aligned to each other, due to similar channel characteristics as seen in Section 3, and the required C/N at $\text{BER} = 1 \times 10^{-3}$ is about 15 dB less than the omnidirectional ones. The big gap can be explained by the fact that the time dispersion and frequency selectivity of the directive channels are much less severer than the omnidirectional channels, as seen from Figures 3–5. However, when the RX beam is misaligned about 35° over the boresight, the resulting performance of Fan-Pen channels becomes rapidly worse compared to the slight performance drop of the Fan-Fan ones, which is consistent with the enormous difference between the values of their channel parameters.

With the convolutional coding, interleaving and Viterbi decoding applied in the system, the performance is dramatically improved for omnidirectional channels compared to

the lower improvement for the directive channels. This arises because the strong frequency selectivity of omnidirectional channels provides the frequency diversity to the channel, which is exploited by the decoder for error correction with the help of the interleaver. Even so, the coding gain cannot bring the system in the omnidirectional channel to a comparable performance level as in the directive ones. For instance, the Omn-Omn configuration requires at least 10 dB higher signal level than the Fan-Fan one to achieve the same $\text{BER} = 1 \times 10^{-3}$. In other words, the directive configurations will save many dBs for the link budget requirement.

In the above BER analysis, all the channels are assumed to have the same received power at each C/N . However, for physical channels, the actual received power in Figure 2 and thus the actual C/N of each configuration will be different from each other. Taking the actual C/N into account in the BER comparison, the directive configurations will further outperform the omnidirectional configurations.

5. CONCLUSIONS

In this paper, we analyzed the time dispersion and frequency selectivity of 60 GHz channels with various antenna configurations based on extensive channel measurements in LOS/NLOS environments. Statistical channel parameters were retrieved from measurements and compared. Particularly, the shape parameters of power delay profiles were retrieved based on a simple profile model. Next the link budget was analyzed and examined for an OFDM system with different constellations and then a baseband OFDM system was simulated to evaluate the BER performance. For the considered environments and antenna configurations, the following conclusions can be drawn from this work.

- (i) The link budget analysis shows that directive configurations will provide sufficient link margins and radio coverage for high data rate communications. In this work, the Fan-Fan and Fan-Pen configurations can achieve the data rate of at least 6 Gbps within a range of 6 meters for LOS scenarios, while the Omn-Omn will achieve up to 4 Gbps. It is also preferable to use directive configurations in NLOS scenarios.
- (ii) For each channel configuration, the coded/uncoded BER performance agreed well for the measured and modeled channels. This confirms that the simple model of the delay profile shape and its parameters are sufficiently accurate for the evaluation of system performance for various channel configurations without a strong cluster-behavior in the channel.
- (iii) Since the multipath effect has been effectively suppressed, a remarkable BER performance is achieved by directive configurations and this leads to the saving of link budget as high as 10 dB compared to omnidirectional ones. Although the omnidirectional configurations can attain higher coding gain from frequency selectivity, the required C/N level is still too high to achieve the target BER in practice.
- (iv) The TX-RX antenna beams have to be properly aligned within the sight of each other, otherwise the

beam-pointing errors will cause an enormous drop in the channel quality and BER performance. The wider beam antennas are generally less sensitive for beam-pointing errors, which indicates that a proper beamwidth has to be designed in practice.

REFERENCES

- [1] M. Fiacco, M. Parks, H. Radi, and S. R. Saunders, "Final report—indoor propagation factors at 17 and 60GHz," Tech. Rep., University of Surrey, Guildford, Surrey, UK, August 1998, study carried out on behalf of the Radiocommunications Agency.
- [2] J. Schöthier, "WP3-study: the 60 GHz channel and its modelling," Tech. Rep., 2001, IST-2001-32686 Broadway.
- [3] P. F. M. Smulders, "Exploiting the 60 GHz band for local wireless multimedia access: prospects and future directions," *IEEE Communications Magazine*, vol. 40, no. 1, pp. 140–147, 2002.
- [4] H. Xu, V. Kukshya, and T. S. Rappaport, "Spatial and temporal characteristics of 60-GHz indoor channels," *IEEE Journal on Selected Areas in Communications*, vol. 20, no. 3, pp. 620–630, 2002.
- [5] IEEE 802.15 WPAN Millimeter Wave Alternative PHY Task Group 3c (TG3c), <http://www.ieee802.org/15/pub/TG3c.html>.
- [6] R. Davies, M. Bensebti, M. A. Beach, and J. P. McGeehan, "Wireless propagation measurements in indoor multipath environments at 1.7 GHz and 60 GHz for small cell systems," in *Proceedings of the 41st IEEE Vehicular Technology Conference (VTC '91)*, pp. 589–593, Saint Louis, Mo, USA, May 1991.
- [7] C. R. Anderson, T. S. Rappaport, K. Bae, et al., "In-building wideband multipath characteristics at 2.5 & 60 GHz," in *Proceedings of the 56th IEEE Vehicular Technology Conference (VTC '02)*, vol. 1, pp. 97–101, Vancouver, BC, Canada, September 2002.
- [8] R. J. C. Bultitude, R. F. Hahn, and R. J. Davies, "Propagation considerations for the design of an indoor broad-band communications system at EHF," *IEEE Transactions on Vehicular Technology*, vol. 47, no. 1, pp. 235–245, 1998.
- [9] N. Moraitis and P. Constantinou, "Indoor channel measurements and characterization at 60 GHz for wireless local area network applications," *IEEE Transactions on Antennas and Propagation*, vol. 52, no. 12, pp. 3180–3189, 2004.
- [10] S. Collonge, G. Zaharia, and G. El Zein, "Influence of the human activity on wide-band characteristics of the 60 GHz indoor radio channel," *IEEE Transactions on Wireless Communications*, vol. 3, no. 6, pp. 2396–2406, 2004.
- [11] D. C. Cox and R. P. Leck, "Correlation bandwidth and delay spread multipath propagation statistics for 910-MHz urban mobile radio channels," *IEEE Transactions on Communications*, vol. 23, no. 11, pp. 1271–1280, 1975.
- [12] B. Glance and L. J. Greenstein, "Frequency-selective fading effects in digital mobile radio with diversity combining," *IEEE Transactions on Communications*, vol. 31, no. 9, pp. 1085–1094, 1983.
- [13] H. Hashemi, "The indoor radio propagation channel," *Proceedings of the IEEE*, vol. 81, no. 7, pp. 943–968, 1993.
- [14] H. Yang, M. H. A. J. Herben, and P. F. M. Smulders, "Frequency selectivity of 60-GHz LOS and NLOS Indoor Radio Channels," in *Proceedings of the 63rd IEEE Vehicular Technology Conference (VTC '06)*, vol. 6, pp. 2727–2731, Melbourne, Australia, May 2006.
- [15] A. A. M. Saleh and R. A. Valenzuela, "A statistical model for indoor multipath propagation," *IEEE Journal on Selected Areas in Communications*, vol. 5, no. 2, pp. 128–137, 1987.
- [16] Q. H. Spencer, B. D. Jeffs, M. A. Jensen, and A. L. Swindlehurst, "Modeling the statistical time and angle of arrival characteristics of an indoor multipath channel," *IEEE Journal on Selected Areas in Communications*, vol. 18, no. 3, pp. 347–360, 2000.
- [17] C.-C. Chong, C.-M. Tan, D. I. Laurenson, S. McLaughlin, M. A. Beach, and A. R. Nix, "A new statistical wideband spatio-temporal channel model for 5-GHz band WLAN systems," *IEEE Journal on Selected Areas in Communications*, vol. 21, no. 2, pp. 139–150, 2003.
- [18] C.-C. Chong and S. K. Yong, "A generic statistical-based UWB channel model for high-rise apartments," *IEEE Transactions on Antennas and Propagation*, vol. 53, no. 8, part 1, pp. 2389–2399, 2005.
- [19] A. F. Molisch, D. Cassioli, C.-C. Chong, et al., "A comprehensive standardized model for ultrawideband propagation channels," *IEEE Transactions on Antennas and Propagation*, vol. 54, no. 11, part 1, pp. 3151–3166, 2006.
- [20] H. Takai, "In-room transmission BER performance of anti-multipath modulation PSK-VP," *IEEE Transactions on Vehicular Technology*, vol. 42, no. 2, pp. 177–185, 1993.
- [21] P. F. M. Smulders, "Broadband wireless LANs: a feasibility study," Ph.D. dissertation, Eindhoven University of Technology, Eindhoven, The Netherlands, December 1995.
- [22] J. C.-I. Chuang, "The effects of time delay spread on portable radio communications channels with digital modulation," *IEEE Journal on Selected Areas in Communications*, vol. 5, no. 5, pp. 879–889, 1987.
- [23] F. Adachi and K. Ohno, "BER performance of QDPSK with postdetection diversity reception in mobile radio channels," *IEEE Transactions on Vehicular Technology*, vol. 40, no. 1, part 2, pp. 237–249, 1991.
- [24] L. Dossi, G. Tartara, and F. Tallone, "Statistical analysis of measured impulse response functions of 2.0 GHz indoor radio channels," *IEEE Journal on Selected Areas in Communications*, vol. 14, no. 3, pp. 405–410, 1996.
- [25] J. B. Andersen, T. S. Rappaport, and S. Yoshida, "Propagation measurements and models for wireless communications channels," *IEEE Communications Magazine*, vol. 33, no. 1, pp. 42–49, 1995.
- [26] J. Medbo, H. Hallenberg, and J.-E. Berg, "Propagation characteristics at 5 GHz in typical radio-LAN scenarios," in *Proceedings of the 49th IEEE Vehicular Technology Conference (VTC '99)*, vol. 1, pp. 185–189, Houston, Tex, USA, May 1999.
- [27] P. A. Bello, "Characterization of randomly time-variant linear channels," *IEEE Transactions on Communications Systems*, vol. 11, no. 4, pp. 360–393, 1963.
- [28] P. Marinier, G. Y. Delisle, and C. L. Despains, "Temporal variations of the indoor wireless millimeter-wave channel," *IEEE Transactions on Antennas and Propagation*, vol. 46, no. 6, pp. 928–934, 1998.
- [29] G. Durgin, T. S. Rappaport, and H. Xu, "Measurements and models for radio path loss and penetration loss in and around homes and trees at 5.85 GHz," *IEEE Transactions on Communications*, vol. 46, no. 11, pp. 1484–1496, 1998.
- [30] R. H. Clarke, "A statistical theory of mobile-radio reception," *Bell System Technical Journal*, vol. 47, no. 6, pp. 957–1000, 1968.
- [31] W. C. Jakes, *Microwave Mobile Communications*, John Wiley & Sons, New York, NY, USA, 1974.

- [32] T. Aulin, "A modified model for the fading signal at a mobile radio channel," *IEEE Transactions on Vehicular Technology*, vol. 28, no. 3, pp. 182–203, 1979.
- [33] S. Qu and T. Yeap, "A three-dimensional scattering model for fading channels in land mobile environment," *IEEE Transactions on Vehicular Technology*, vol. 48, no. 3, pp. 765–781, 1999.
- [34] S. Thoen, L. Van der Perre, and M. Engels, "Modeling the channel time-variance for fixed wireless communications," *IEEE Communications Letters*, vol. 6, no. 8, pp. 331–333, 2002.
- [35] K. Sato and T. Manabe, "Estimation of propagation-path visibility for indoor wireless LAN systems under shadowing condition by human bodies," in *Proceedings of the 48th IEEE Vehicular Technology Conference (VTC '98)*, vol. 3, pp. 2109–2113, Ottawa, Canada, May 1998.
- [36] K. Witrals, G. Landman, and A. Bohdanowicz, "Practical application of a novel method for estimating the RMS delay spread from power measurements," in *Proceedings of the 4th European Mobile Communications Conference (EPMCC '01)*, Vienna, Austria, February 2001.
- [37] ETSI, "Digital Video Broadcasting (DVB); framing structure, channel coding and modulation for digital terrestrial television," European Telecommunications Standards Institute, November 2004, eN 300 744 V1.5.1.

Research Article

Rain Attenuation at 58 GHz: Prediction versus Long-Term Trial Results

Vaclav Kvicera and Martin Grabner

Technical Centre of Telecommunications and Posts (TESTCOM), Hvozdanska 3, 148 01 Praha 4, Czech Republic

Received 13 April 2006; Revised 13 October 2006; Accepted 17 December 2006

Recommended by Su-Khiong Yong

Electromagnetic wave propagation research in frequency band 58 GHz was started at TESTCOM in Praha due to lack of experimentally obtained results needed for a realistic calculation of quality and availability of point-to-point fixed systems. Rain attenuation data obtained from a path at 58 GHz with V polarization located in Praha was processed over a 5-year period. Rainfall intensities have been measured by means of a heated siphon rain gauge. In parallel, rainfall intensity data from rain gauge records was statistically processed over the same year periods as the rain attenuation data. Cumulative distributions of rainfall intensities obtained as well as cumulative distributions of rain attenuation obtained are compared with the calculated ones in accordance with relevant ITU-R recommendations. The results obtained can be used as the primary basis for the possible extension of the ITU-R recommendation for calculating rain attenuation distributions up to 60 GHz. The obtained dependence of percentages of time of the average year on the percentages of time of the average worst month is also compared with the relevant ITU-R recommendation. The results obtained are discussed.

Copyright © 2007 V. Kvicera and M. Grabner. This is an open access article distributed under the Creative Commons Attribution License, which permits unrestricted use, distribution, and reproduction in any medium, provided the original work is properly cited.

1. INTRODUCTION

Frequency bands above 38 GHz will be extensively utilized by terrestrial digital fixed services in the near future because the lower bands are almost fully occupied. It means that the 60 GHz frequency band will be utilized now although there is a lack of experimentally obtained primary bases which are needed for realistic calculations of both availability and reliability of service. Some experimental activities is focused on specific attenuation due to rain [1] or intervehicle communications [2]. One-year results of propagation experiment at 58 GHz carried out in Sydney and Praha were described in [3]. Results of 2-year measurement of attenuation due to specific hydrometeors (rain, rain with hail, snow, fog) were described in [4]. Relevant ITU-R recommendation [5] which can be used for estimating long-term statistics of rain attenuation is considered to be valid in all parts of the world at least for frequencies up to 40 GHz and path lengths up to 60 km. Minimum usable path length is not mentioned.

The 60 GHz frequency band is suitable for short-range communications technologies. Significant oxygen absorption, water vapour absorption, and attenuation due to hydrometeors (rain, snow, hail, and fog) limit communications

systems. The oxygen absorption has a peak near 60 GHz, typically around 16 dB/km [6]. Water vapour further slightly attenuates the signal, about 0.2 dB/km. Therefore the band is the most suitable one for intensive frequency reuse.

This contribution presents rain attenuation characteristics at 58 GHz with V polarization obtained on a path 850 m long, over a 5-year period of observation.

2. EXPERIMENTAL SETUP

Electromagnetic wave propagation research in the frequency band 58 GHz was started at TESTCOM in December 2000. NOKIA MetroHopper equipment working on frequency 57.650 GHz with V polarization has been used. The length of the experimental path which is located in Praha is about 850 m. Recording margin has been about 30 dB due to special offset antennas used. The research is focused on attenuation due to hydrometeors. The calibrated AGC voltages corresponding to the received signal level have been gathered continuously with the sampling of 10 Hz on PC hard disc, and data obtained over a 5-year period from December 2000 to November 2005 was processed statistically.

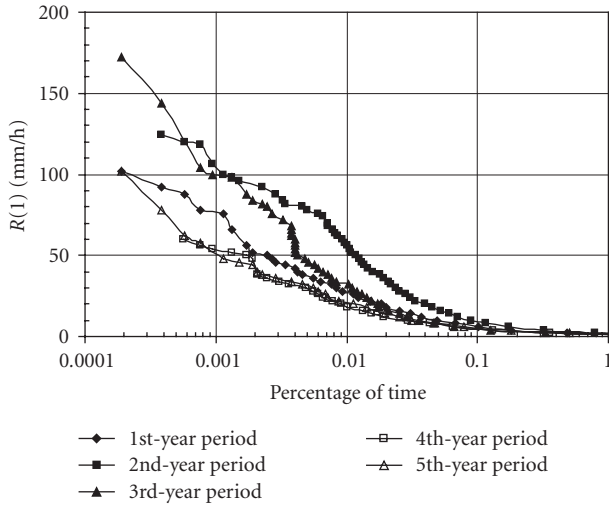


FIGURE 1: CDs of average 1-minute rain intensities for individual 1-year periods.

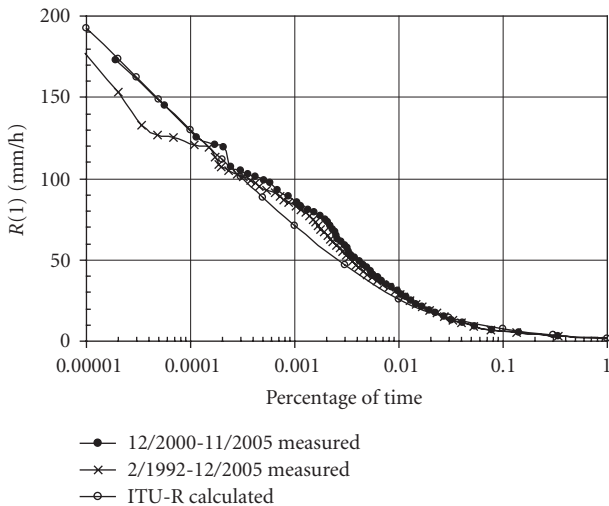


FIGURE 2: CDs of average 1-minute rain intensities for AY.

It should be noted that only rain attenuation events were processed. Not only attenuation due to rain but also attenuation due to rain with snow, snow, fog, and hail occurred within the 5-year period of observation. Individual attenuation events were compared with concurrent meteorological situations and were carefully classified according to the types of individual hydrometeors occurring.

Meteorological conditions were identified by means of both video BW camera images of the space between transmitter and receiver sites, and data obtained from an automatic meteorological station located near the receiver site. The automatic meteorological station is equipped with VAISALA sensors for measurement of temperature, humidity and pressure of air, velocity and direction of wind, visibility and 2 tipping-bucket rain gauges with differing collecting areas. These rain gauges were used only for indication of rainfalls due to their low time resolution of tips.

Rainfall intensities have been measured since February 1992 by means of a heated siphon rain gauge. Rainfall intensity data from rain gauge records was statistically processed over the same contiguous 1-year periods as was the rain attenuation data.

Both the rain attenuation data and the rainfall intensity data were statistically processed twice: (1) over five individual contiguous 1-year periods, and (2) together over the entire 5-year period.

3. TRIAL RESULTS AND DISCUSSION

3.1. Rainfall intensity distributions

Resulting cumulative distributions (CDs) of average 1-minute rainfall intensities ($R(1)$) for individual 1-year periods of observation are given in Figure 1.

Large year-to-year variations of individual year distributions may be seen clearly in Figure 1. Differences up to +15 mm/h – 37 mm/h for 0.001% of time, +25 mm/h – 11 mm/h for 0.01% of time, and +5 mm/h – 2 mm/h for 0.1% of time occur between measured average 1-minute rainfall intensities and rainfall intensities corresponding to CD of $R(1)$ for the average year (AY).

It should be noted that the values of rain intensities for the lowest percentages of time correspond mostly to a single rain event in a full year, and therefore they are not statistically reliable.

Resulting CD of $R(1)$ for the AY over the 5-year period, resulting CD of $R(1)$ for the AY over the 14-year period 1992–2005, and CD of $R(1)$ for the AY in accordance with ITU-R recommendation [7] are plotted together in Figure 2.

It can be seen that the value of $R(1)$ for 0.01% of time for the entire 5-year period is 30.2 mm/h while the value of $R(1)$ for the same percentage of time obtained through processing rainfall intensity data over the 14-year period is 29.3 mm/h, and the $R(1)$ for 0.01% of time in accordance with ITU-R recommendation [7] is 26.0 mm/h.

Resulting CDs of $R(1)$ for the whole 5-year period of observation together and for the 14-year period are very much alike: they differ from each other by no more than 14 mm/h in the range from 1% to 0.0001%. $R(1)$ obtained over the 5-year period are up to 20 mm/h greater (for the percentage of time of about 0.002%) than the $R(1)$ calculated in accordance with ITU-R recommendation [7].

Perfect agreement emerging between the obtained values $R(1)$ and the calculated ones for percentages of time smaller than 0.0001% is remarkable.

3.2. Rain attenuation distributions

Rain attenuation data obtained on the path at 58 GHz with V polarization was processed over the same 5-year period as was rainfall intensity data. For the first 3-year period, special offset V-polarized antennas were not covered with radomes. Radomes made of special rubberized canvas have been used since November 2003 to protect antennas against snow drifts.

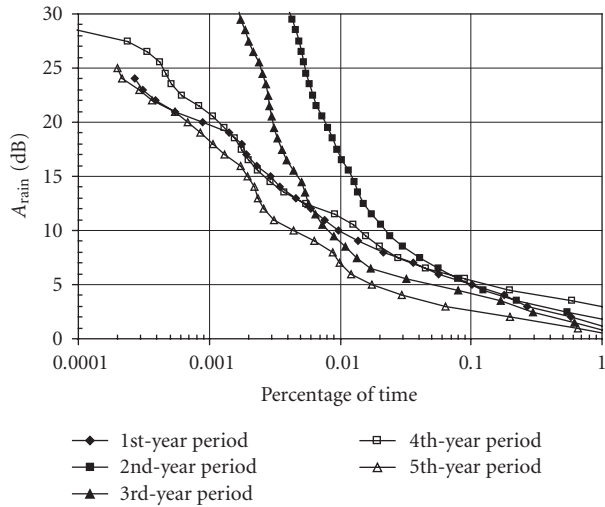


FIGURE 3: CDs of rain attenuation for individual 1-year periods.

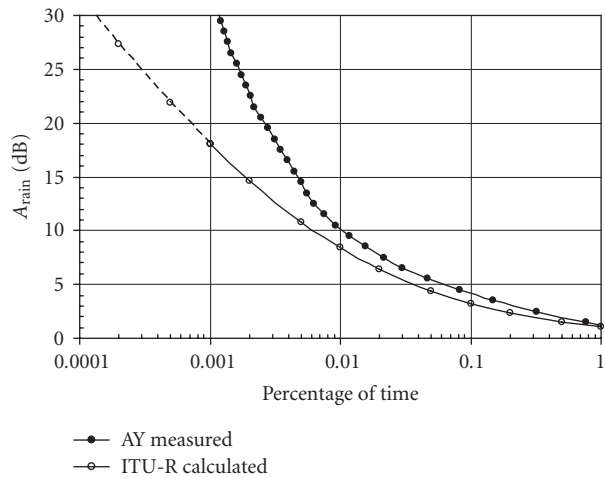


FIGURE 4: CDs of rain attenuation for AY.

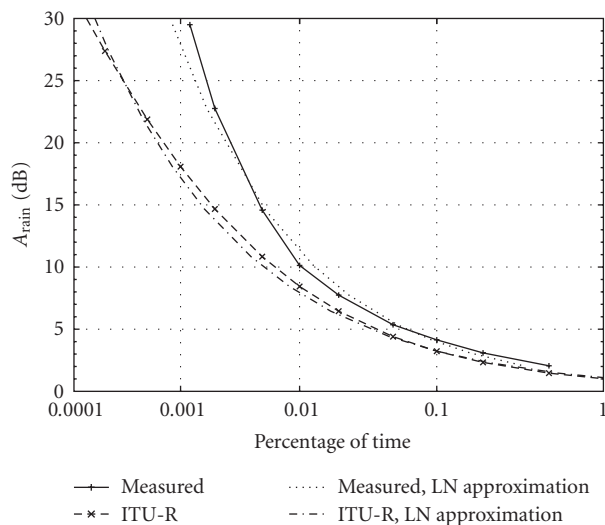


FIGURE 5: CDs of rain attenuation for AY and its LN approximations.

Moreover, when radomes installed on antennas were wet, additional attenuation about 2 dB was observed. Therefore the obtained CDs of attenuation due to rain were shifted about 2 dB since November 2003 to compensate for this effect. Of course, CDs of attenuation due to rain for the first 3-year period of observation remained without modifications.

Resulting CDs of attenuation due to rain for individual 1-year periods of observation separately are plotted in Figure 3.

Large year-to-year variations of individual year distributions may be seen, similarly as in Figure 1. The notice concerning the low statistic reliability of the values of rain attenuation for the lowest percentages of time is also valid for distributions given in Figures 3 and 6. The comparison of CDs of $R(1)$ and CDs of rain attenuation, as plotted in Figures 1 and 3, is very interesting. Very good correspondence exists between rainfall intensities and rain attenuation for the second year of observation. The values of both rainfall intensities and rain attenuation are the highest ones for time percentages between 0.1% and 0.004%. While the rainfall intensities for the 4th- and the fifth-year periods are very close to each other, associated rain attenuation values significantly differ. Relevant analysis in more detail is given in Section 3.3.

Resulting CD of attenuation due to rain for the average year over the 5-year period of observation and CDs of attenuation due to rain for the AY in accordance with ITU-R recommendation [5] are plotted together in Figure 4. The measured value of $R(1) = 30.2$ mm/h for 0.01% of time over all the 5-years of observation, obtained from Figure 2, was used for the calculation of CD of rain attenuation in accordance with ITU-R recommendation [5].

Due to the fact that the recommendation is valid for percentages of time of AY between 0.001% and 1% only, the part of CD calculated for percentages of time smaller than 0.001% is plotted by dashed line. This convention is also used in Figures 8–12. It must be stressed that all the comparisons made out of the range of validity must be treated with care. Naturally, availability smaller than 0.001% can be assessed only exceptionally. If the calculated value of $R(1) = 26.0$ mm/h for 0.01% of time, obtained from ITU-R recommendation [7], is used for the calculation of CD, the calculated values of attenuation will be even smaller if the measured value of $R(1)$ over the entire 5-year period of observation is used.

Very smooth curve was obtained for the measured CD of attenuation due to rain for the average year over the 5-year period of observation. It can be seen that the smaller the percentage of time is, the greater the difference between measured values of rain attenuation and the calculated ones is. For percentages of time greater than 0.01%, measured values of attenuation due to rain are greater than the calculated ones up to about 1.5 dB. The obtained values of rain attenuation then grow up rapidly for percentages of time smaller than 0.01%. A difference of about 13 dB can be observed between the measured rain attenuation and the calculated one for the chosen percentage of time of about 0.001%.

From the point of view of the percentages of time, it can be noted that for the value of attenuation due to rain of 30 dB, the difference between the measured percentage of time and the calculated one is about one decade. These

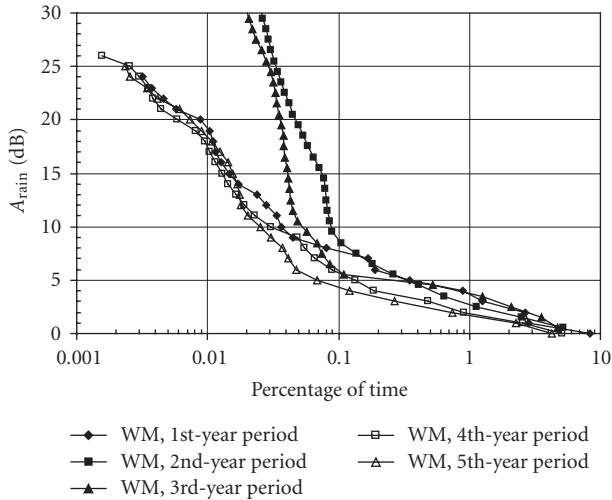


FIGURE 6: CDs of rain attenuation for WM of individual 1-year periods.

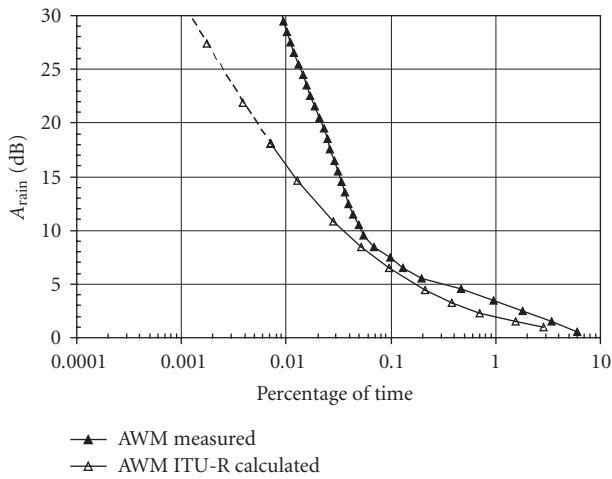


FIGURE 7: CDs of rain attenuation for AWM.

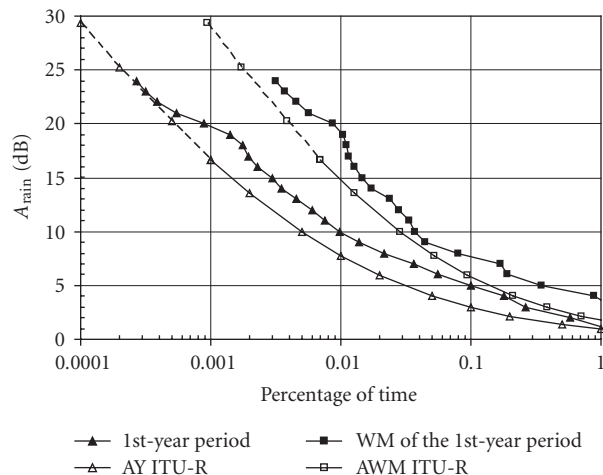


FIGURE 8: CDs of rain attenuation obtained for the first-year period.

differences can be explained (1) by the fact that the ITU-R prediction procedure is considered to be valid for frequencies up to 40 GHz, and (2) by the influence of local climate conditions.

The cumulative distributions of rain attenuation for the average year, as plotted in Figure 4, can be approximated by log-normal (LN) distributions. The measured CD of rain attenuation can be approximated by LN distribution with the parameters $\mu = 0.0239$ dB and $\sigma^2 = 2.7394$, and the calculated CD of rain attenuation in accordance with ITU-R recommendation [7] can be approximated by LN distribution with the parameters $\mu = 0.0402$ dB and $\sigma^2 = 2.0154$. All distributions mentioned here are shown together in Figure 5 in the dB-normal scale to better see the differences between the obtained distributions and their LN approximations than when shown in the log-normal scale. Differences between the calculated CD of rain attenuation in accordance with the ITU-R recommendation and its LN approximation are about ± 1 dB. Slightly greater differences can be seen between the measured CD of rain attenuation and its LN approximation, about +1.5 dB for 0.01% of time and about 3.5 dB for about 0.001% of time of year.

Resulting CDs of attenuation due to rain for the worst months (WMs) of individual 1-year periods of observation separately are plotted in Figure 6.

The CD of rain attenuation obtained for the average worst month (AWM) over the entire 5-year period of observation and CDs of attenuation due to rain for the AWM in accordance with ITU-R recommendation [5] are plotted together in Figure 7. The measured value of $R(1) = 30.2$ mm/h for 0.01% of time over the entire 5-year period of observation (obtained from Figure 2) was used for the calculation of CD of rain attenuation for the average worst month in accordance with ITU-R recommendation [5]. Because the recommendation is valid for percentages of time of AWM between 0.007% and 1% only, the part of CD calculated for percentages of time smaller than 0.007% is plotted by dashed line. This convention is also used in Figures 8–12. The comparisons made out of the validity range must be treated again with care.

For percentages of time greater than 0.005%, measured values of attenuation due to rain are greater than the calculated ones up to about 2 dB. The difference up to about 13 dB can be observed between the measured rain attenuation and the calculated one for the percentage of time of about 0.01%.

From the point of view of the percentages of time, the difference between measured percentage of time and the calculated one is about one decade for the attenuation due to rain of 30 dB. These significant differences can also be explained by the fact that the ITU-R prediction procedure is considered to be valid for frequencies up to 40 GHz only and by influence of local climate conditions.

3.3. Year-to-year variability of rain attenuation distributions

Due to the fact that measured values of attenuation due to rain are greater than those calculated in accordance with

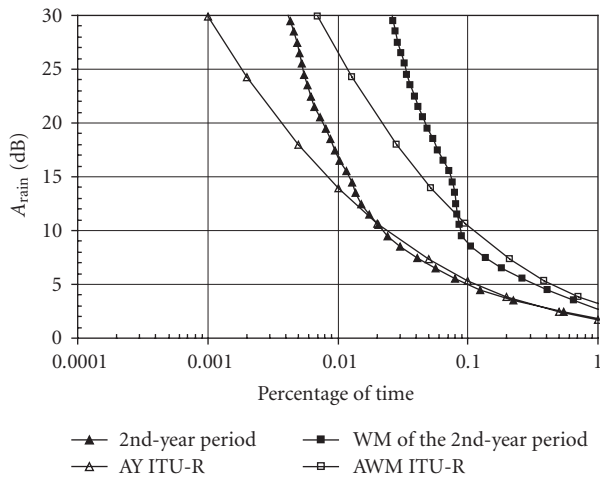


FIGURE 9: CDs of rain attenuation obtained for the second-year period.

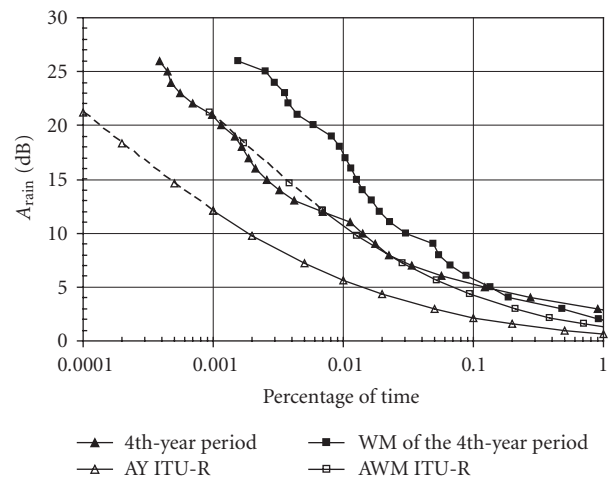


FIGURE 11: CDs of rain attenuation obtained for the fourth-year period.

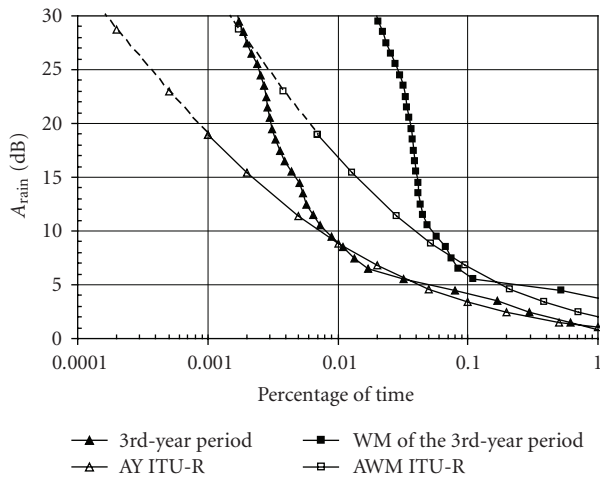


FIGURE 10: CDs of rain attenuation obtained for the third-year period.

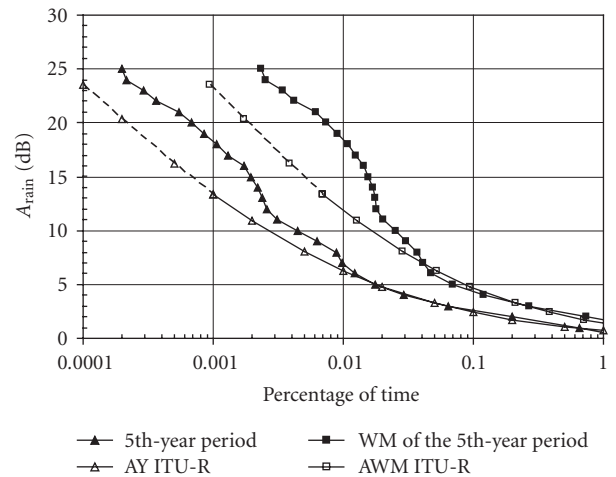


FIGURE 12: CDs of rain attenuation obtained for the fifth-year period.

ITU-R recommendation [5] for both the average year distribution (Figure 4) and the average worst-month distribution (Figure 7), it will be useful to analyze the results obtained on a year-to-year basis. Measured values of $R(1)$ for 0.01% of time in individual-year periods, obtained from Figure 1, were used for the calculation of CDs of rain attenuation for individual-year periods in accordance with ITU-R recommendation [5]. Worst-month distributions were calculated from the year distributions using ITU-R recommendation [8].

Resulting CDs of attenuation due to rain and the calculated ones in accordance with [5] for both the first-year period and the worst month of the first-year period are plotted together in Figure 8.

It can be seen that measured values of attenuation due to rain are greater than the calculated ones by up to about 4.5 dB for both the first-year period and the worst month of the first-year period.

The results obtained for the second-year period are shown in Figure 9.

For the second-year period, the measured values of attenuation due to rain agree very well with the calculated values of attenuation due to rain in accordance with the ITU-R recommendation [5] for the percentages of time greater than 0.02%. For the worst month of the second-year period, measured values of attenuation due to rain are lower than the calculated ones by up to about 1.5 dB for percentages of time greater than 0.09%. Measured values of attenuation are greater than the calculated ones for smaller percentages of time than forenamed.

The results obtained for the third-year period are drawn in Figure 10.

For the third-year period, measured values of attenuation due to rain agree very well with the calculated values of attenuation due to rain in accordance with the ITU-R recommendation [5] for percentages of time greater than 0.01%. For the

TABLE 1: Comparison of the measured rainfall intensities, the calculated attenuation due to rain, and the measured attenuation due to rain for the individual-year periods and the entire 5-year period for 0.01% of time of year only. Note that the numbers in parenthesis are the span of relevant quantities from the highest value to the lowest one.

Period	$R_{0.01}(1)$ (mm/h)	$A_{0.01}$ (dB) ITU-R [1]	$A_{0.01}$ (dB) measured
1st year	27.4 (3)	7.8 (3)	10.0 (3)
2nd year	56.4 (1)	14.0 (1)	16.8 (1)
3rd year	32.0 (2)	8.8 (2)	9.0 (4)
4th year	18.5 (5)	5.6 (5)	11.2 (2)
5th year	21.0 (4)	6.3 (4)	7.0 (5)
5 years	30.2	8.4	10.1

worst month of the third-year period, measured values of attenuation due to rain agree very well with calculated values of attenuation due to rain in accordance with the ITU-R recommendation [5] for percentages of time greater than 0.07%. Measured values of attenuation for both the third-year period and its worst month grow up rapidly for smaller percentages of time than forenamed.

The results obtained for the fourth-year period are plotted in Figure 11.

Both the measured values of attenuation due to rain for the fourth-year period and for its worst month are greater than the calculated ones by up to about 10 dB. Besides this, the measured CD of attenuation due to rain for the fourth-year period agree very well with the calculated CD of attenuation due to rain for its worst month.

The results obtained for last-the fifth-year periods are shown in Figure 12.

For the fifth-year period, measured values of attenuation due to rain agree very well with calculated values of attenuation due to rain in accordance with the ITU-R recommendation [5] for percentages of time greater than 0.01%. For the worst month of the third-year period, measured values of attenuation due to rain agree very well with the calculated ones for percentages of time greater than 0.04%. For percentages of time smaller than the forenamed ones, measured values of attenuation due to rain are greater than the calculated ones by up to about 5 dB for the year period and by up to about 7 dB for its worst month.

For the average year distribution, good agreement between measured values of rain attenuation and those calculated was found for percentages of time greater than 0.01%. For percentages of time smaller than 0.01%, obtained values of rain attenuation then grow up rapidly and a difference of about 13 dB occurs for 0.001 percentage of time.

For the average worst-month distribution, good agreement between measured values of rain attenuation and those calculated was found for percentages of time greater than 0.05%. For percentages of time smaller than 0.05%, obtained values of rain attenuation then grow up rapidly, and a difference of about 13 dB occurs for 0.01% of time.

Comparison of measured rainfall intensities, calculated attenuation due to rain, and measured attenuation due to rain for individual 1-year periods and the entire 5-year period for exclusively 0.01% of time of year are given in Table 1.

Best agreement between the measured value of rain attenuation and the calculated one for exclusively 0.01% of time of year was found for the third year of observation. Very good agreement, that is, a difference smaller than 3 dB between the calculated value of rain attenuation and the measured one, can be observed for the first-, the second-, and the fifth-year periods.

While calculated values of attenuation in accordance with the ITU-R recommendation correspond with measured rainfall intensities in individual-year periods very well (i.e., the higher rain intensity, the higher rain attenuation), measured values of rain attenuation do not correspond exactly with measured rainfall intensities for the second, fourth, and fifth years. Better correspondence can be found for the first and the third years of observation.

While rainfall intensities for the fourth- and the fifth-year periods are very close to each other, rain attenuation values significantly differ by about 4 dB. While rainfall intensities for the first- and the third-year periods are greater than rainfall intensities for the fourth- and fifth-year periods, rain attenuation values are situated between the CDs for the fourth- and the fifth-year periods.

Although the measured rainfall intensity of 32.0 mm/h is the second highest one, the measured rain attenuation of 9.0 dB is on the fourth position. Similarly, the measured rainfall intensity of 18.5 mm/h is the lowest one while the measured rain attenuation of 11.2 dB is on the second position. Finally, the measured rainfall intensity of 21.0 mm/h is on the fourth position while the measured rain attenuation of 7.7 dB is the lowest one.

It is apparent that the span of measured rain attenuation values for individual-year periods should correspond with the span of values of measured rainfall intensities, similarly as the correspondence is in the case of the span of rain attenuation values calculated in accordance with the ITU-R recommendation. It should be further analyzed why it is not so.

3.4. Conversion of annual statistics to worst-month statistics

The obtained dependence of the percentage of time of the average year P_{AY} on the percentage of time of the average worst month P_{AWM} for selected values of rain attenuation is drawn in Figure 13. The dependence can be approximated for $1 \text{ dB} \leq A_{\text{rain}} \leq 30 \text{ dB}$ by the formula

$$P_{AWM} = 3.79P_{AY}^{0.89} (\%) \quad (1)$$

with a correlation coefficient $r = 0.9895$.

It can be seen from Figure 13 that calculated percentages of time of AWM in accordance with ITU-R recommendation [8] are slightly lower than percentages of time corresponding to linear approximation of measured values. The reason is that ITU-R recommendation [8] presents slightly different

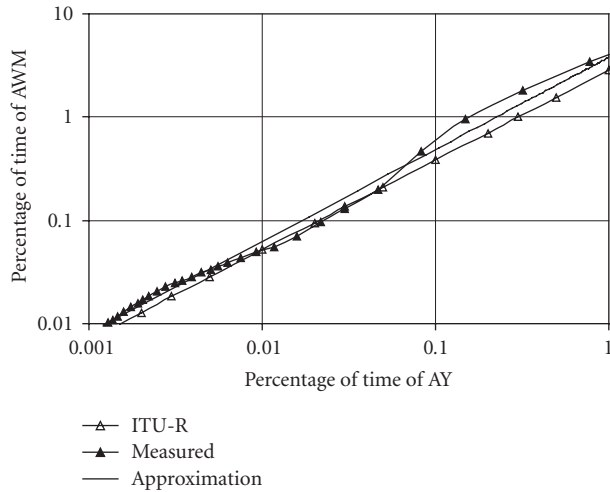


FIGURE 13: Dependence of percentages of time of AWM on percentages of time of AY.

formulas for the calculation of P_{AWM} from P_{AY} :

$$P_{AWM} = 2.85P_{AY}^{0.87} (\%). \quad (2)$$

4. CONCLUSIONS

Rain attenuation data obtained at 58 GHz for V polarizations on an 850 m terrestrial path as well as rainfall intensity data from rain gauge records were statistically processed over five individual contiguous 1-year periods and over the entire 5-year period of observation together. Cumulative distributions of average 1-minute rainfall intensities as well as cumulative distributions of rain attenuation for individual-year periods, individual worst months of 1-year periods, for the average year and the average worst month were obtained.

Large year-to-year variations of individual-year distributions were noted. Cumulative distributions of rain attenuation for both the average year and the average worst month obtained were compared with those calculated in accordance with relevant ITU-R recommendation. Results obtained can be used as basis for the extension of ITU-R recommendation [5] for frequencies over 40 GHz.

Cumulative distributions of rain attenuation obtained were analyzed in detail on a year-to-year basis and were compared with distributions corresponding to relevant ITU-R recommendation. It may be seen clearly that the results obtained from 1-year measurement only are not statistically reliable from the long-term point of view. Results of long-term measurements only, that is, at least 3-year measurement, are needed for the realistic assessment of availability of point-to-point fixed systems. The conversion of cumulative distributions of rainfall intensities into cumulative distributions of rain attenuation should be further analyzed. The dependence of average worst-month time percentages on average year time percentages was examined and the result obtained was compared with relevant ITU-R recommendation.

Our long-term experimental research will continue. Further work will be focused on conversion of cumulative distributions of rainfall intensities into cumulative distributions of rain attenuation and on polarization dependence of rain attenuation at 58 GHz.

ACKNOWLEDGMENTS

The work on recording and processing of both rainfall intensity data and rain attenuation data was supported by the Ministry of Informatics of the Czech Republic under the Project no. MIO 0000346806 "Application of methods and tools aimed at the development of communication infrastructure and services to information society in the Czech Republic."

REFERENCES

- [1] W. Åsen and C. J. Gibbins, "A comparison of rain attenuation and drop size distributions measured in Chilbolton and Singapore," *Radio Science*, vol. 37, no. 3, 2002.
- [2] A. Kato, K. Sato, M. Fujise, and S. Kawakami, "Propagation characteristics of 60-GHz millimeter waves for ITS inter-vehicle communications," *IEICE Transactions on Communications*, vol. E84-B, no. 9, pp. 2530–2539, 2001.
- [3] G. Timms, V. Kvicera, and M. Grabner, "60 GHz band propagation experiments on terrestrial paths in Sydney and Praha," *Radioengineering*, vol. 14, no. 4, pp. 27–32, 2005.
- [4] V. Kvicera, M. Grabner, and O. Fiser, "Results of 2-year concurrent measurements of attenuation at 58 GHz and rain intensities," in *Proceedings of the 11th Microcoll Conference*, pp. 77–80, Budapest, Hungary, September 2003.
- [5] Rec. ITU-R P.530-11, "Propagation data and prediction methods required for the design of terrestrial line-of-sight systems," ITU-R Recommendations, September 2005.
- [6] Rec. ITU-R P.676-6, "Attenuation by atmospheric gases," ITU-R Recommendations, September 2005.
- [7] Rec. ITU-R P.837-4, "Characteristics of precipitation for propagation modelling," ITU-R Recommendations, September 2005.
- [8] Rec. ITU-R P.841-4, "Conversion of annual statistics to worst-month statistics," ITU-R Recommendations, September 2005.

Research Article

Rain-Induced Bistatic Scattering at 60 GHz

Henry T. van der Zanden,^{1,2} Robert J. Watson,² and Matti H. A. J. Herben¹

¹Department of Electrical Engineering, Eindhoven University of Technology, 5600 MB Eindhoven, The Netherlands

²Department of Electronic and Electrical Engineering, University of Bath, Bath BA2 7AY, UK

Received 27 June 2006; Revised 10 November 2006; Accepted 15 January 2007

Recommended by Peter F. M. Smulders

This paper presents the results of a study into the modeling and prediction of rain-induced bistatic scattering at 60 GHz. The bistatic radar equation together with Mie theory is applied as the basis for calculating the scattering. Together with the attenuation induced by the medium before and after scattering, the received scattered power can be calculated at a given path geometry and known orientations of transmit and receive antennas. The model results are validated by comparison with published measurements. Finally, recommendations are made for future deployments of 60 GHz infrastructure.

Copyright © 2007 Henry T. van der Zanden et al. This is an open access article distributed under the Creative Commons Attribution License, which permits unrestricted use, distribution, and reproduction in any medium, provided the original work is properly cited.

1. INTRODUCTION

Recently there has been considerable interest in the 60 GHz frequency band for short distance fixed point-to-point links (<2.5 km) including the so-called “last-mile” communications. The high oxygen attenuation in this band limits its practical use for longer terrestrial links and for Earth-space communication. The main application therefore is in dense urban environments where a high density of short links might be expected. For point-to-point links, one of the key advantages of the 60 GHz band is the relatively high directivity achievable from a physically small antenna. The narrow beam-widths and low side-lobe levels achievable mean that the signal power outside the narrow main lobe is very low.

This is compounded by the high oxygen attenuation in the 60 GHz frequency band, which results in an even faster decrease of signal power outside the main beam. At 60 GHz the oxygen attenuation is typically between 12 and 15 dB km⁻¹. This high attenuation results in very short frequency-reuse distances making these systems extremely suited for high-link density deployments with minimum interference between the links. However, when rain falls on the link, interference between nearby links can occur due to bistatic scattering.

In 2003, a study was performed by QinetiQ on behalf of Ofcom (the UK Office of Communications) to investigate

bistatic scattering at 60 GHz. This study performed a number of measurements and drafted guidelines to take account for rain scattering in dense networks of 60 GHz point-to-point links. This study concluded that even for modest rainfall rates, <10 mm h⁻¹, bistatic coupling is often evident. The study also highlighted the need for the development of theoretical models such as the one presented here.

The basic theory of bistatic scattering has been well explained in the literature (see [1, 2]). There has been much research work into the effects of bistatic scattering at frequencies other than 60 GHz (see, e.g., [3, 4]). At 94 GHz it has been shown that a first-order approximation of multiple-scattering is sufficient to describe bistatic scattering by rain [4]. The effect of multiple scattering generally increases with increasing frequency. It is expected that the first-order approximation of multiple scattering should be sufficient to describe bistatic scattering of rain at 60 GHz. At both 94 GHz and 60 GHz, the wavelength is comparable to the typical diameters of raindrops.

There are few experimental results on bistatic scattering available at 60 GHz (see [5, 6]). Results of rain-induced bistatic scattering have already been investigated and presented in literature. There is a lot of information available, but no specific models have been produced for the evaluation of rain-induced bistatic scattering at 60 GHz.

2. THEORETICAL BACKGROUND

2.1. Bistatic scattering in rain

Bistatic scattering can be obtained in different ways; by single scattering, first-order multiple scattering, multiple scattering, and by the diffusion approximation. The first-order multiple scattering assumes that the wave interacts only with one particle and suffers from attenuation on its way from transmitter to receiver. The incident waves at the particles are assumed to come directly from the transmitter. The amount of incident power from scattered waves is negligible because of the relative low density of rain drops, even in high rain rates. Gloaguen and Lavergnat [4] have shown that the first-order multiple scattering is sufficient to describe scattering in rain for 94 GHz. Since the wavelengths at 60 GHz and 94 GHz are both of the same order as the raindrop radii, a first-order multiple scattering approximation is expected to be applicable at 60 GHz.

The single particle scattering by rain can broadly be described by the bistatic radar equation [1]:

$$\frac{P_r}{P_t} = \iiint_{V_c} \frac{\lambda^2 G_t G_r A_1 A_2}{(4\pi)^3 R_1^2 R_2^2} \rho \sigma_{\text{bi}} \exp(-\gamma_1 - \gamma_2) dV. \quad (1)$$

P_r is the received power, P_t the transmitter power, V_c the common volume, G_t the gain of the transmit antenna, G_r the gain of the receive antenna, A_1 the attenuation at the path from the transmitter to the common volume, A_2 the attenuation at the path from the common volume to the receiver, R_1 the distance from the transmitter to the common volume, R_2 the distance from the common volume to the receiver, $\rho \sigma_{\text{bi}}$ the scatter cross section of each point in the common volume, and γ_1 and γ_2 the optical distances from the transmitter to dV and from dV to the receiver, respectively.

When narrow-beam antennas are used, (1) can further be simplified. The assumption of modeling the antennas as narrow beams is valid since, in practical point-to-point link deployments at 60 GHz, beamwidths will typically be between 0.5 and 2.5 degrees with the first side-lobe at least 20 dB down from the main lobe. Since the beams are very narrow and the path lengths short, the common volume is relatively small. This permits the additional assumption that the raindrop size distribution in the common volume is constant. The rainfall rate is assumed to be constant which is also likely to be true for a small common volume. Finally, the narrow beam approximation for the antennas allows them to be modeled as constant-gain cones. This last assumption gives rise to slight overestimation of the received power, but yields a straightforward analytical solution to V_c (see [1]):

$$V_c = \frac{\pi \sqrt{\pi}}{8(\ln 2)^{3/2}} \frac{R_1^2 R_2^2 \theta_1 \theta_2 \phi_1 \phi_2}{[R_1^2 \phi_1^2 + R_2^2 \phi_2^2]^{1/2}} \frac{1}{\sin \theta_s}, \quad (2)$$

where θ_1 and Φ_1 are the half-power beamwidths of the transmitter and θ_2 and Φ_2 are the half-power beamwidths of the receiver. $\rho \sigma_{\text{bi}}$ can then be replaced with $\rho \langle \sigma_{\text{bi}} \rangle$, the total cross-section per unit volume and the integral over V_c becomes a

straightforward product:

$$\frac{P_r}{P_t} = \frac{\lambda^2 G_t G_r A_1 A_2}{(4\pi)^3 R_1^2 R_2^2} \rho \langle \sigma_{\text{bi}} \rangle \exp(-\gamma_1 - \gamma_2) V_c. \quad (3)$$

$\rho \langle \sigma_{\text{bi}} \rangle$ is dependent on the raindrop size distribution and the scattering cross section. The relationship between them is

$$\rho \langle \sigma_{\text{bi}} \rangle = \int_0^\infty n(D, \bar{r}) \sigma_{\text{bi}}(D) dD, \quad (4)$$

where σ_{bi} is the bistatic scattering cross section and $n(D, \bar{r}) dD$ is the number of drops per unit volume located at \bar{r} having a range of sizes between D and $D + dD$.

To calculate $\rho \langle \sigma_{\text{bi}} \rangle$ for raindrops and signals with a frequency between 58 and 66 GHz, Mie theory is a good option. The use of Mie theory requires the approximation that raindrops are spheres (see [7]). While raindrops are only spherical for small drop radii, the uncertainty in the raindrop size distribution is likely to outweigh the difference between modeling the raindrops as spheroids, which would be more accurate.

2.2. Mie theory

Mie theory describes an exact solution to the scattering properties of an isotropic, homogeneous sphere having radius a , with an incident plane electromagnetic wave [2].

In contrast to the geometrical optics approximation (requiring $\lambda \ll D$) and the Rayleigh approximation (requiring $\lambda \gg D$), Mie theory can be used for all possible ratios of diameter to wavelength. For raindrops and frequencies between 58 and 66 GHz, the wavelength and the diameter are of similar order.

To calculate the scattering cross sections of raindrops and the extinction cross sections of raindrops with Mie theory, the amplitude functions defined in classical Mie theory are used [8]:

$$S_1(\theta_s) = \sum_{n=1}^{\infty} \frac{2n+1}{n(n+1)} (a_n \pi_n(\cos \theta_s) + b_n \tau_n(\cos \theta_s)), \quad (5)$$

$$S_2(\theta_s) = \sum_{n=1}^{\infty} \frac{2n+1}{n(n+1)} (a_n \tau_n(\cos \theta_s) + b_n \pi_n(\cos \theta_s)).$$

The functions a_n and b_n are terms involving spherical Bessel functions, the complex refractive index, and the functions τ_n and π_n which are terms involving the Legendre polynomials.

The extinction cross sections for perpendicular (\perp) and parallel (\parallel) incident waves are:

$$\sigma_{\text{ext}\perp}(\theta_s) = \frac{2\pi a^2}{x^2} \Re \{S_1(\theta_s)\}, \quad (6)$$

$$\sigma_{\text{ext}\parallel}(\theta_s) = \frac{2\pi a^2}{x^2} \Re \{S_2(\theta_s)\},$$

where the size parameter $x = ka$, in which the wavenumber $k = 2\pi/\lambda$.

A raindrop can be seen as a particle illuminated with incident power from the transmitter which it then re-radiates

like a directive antenna. The gain functions for a raindrop with a perpendicular and parallel polarized wave are [3]

$$\begin{aligned} G_1 &= \frac{4i_1}{x^2}, \\ G_2 &= \frac{4i_2}{x^2} \end{aligned} \quad (7)$$

with $i_1 = |S_1(\theta_s)|^2$ and $i_2 = |S_2(\theta_s)|^2$. The antenna gain function is defined by

$$G = \frac{4\pi A_{\text{eff}}}{\lambda^2}. \quad (8)$$

By combining those gain functions of the raindrop and the antenna gain function, the effective aperture of a raindrop can be calculated. This effective aperture is the scattering cross section. This analysis yields in the following functions for the scattering cross section for perpendicular and parallel incident waves:

$$\begin{aligned} \sigma_{\text{sca}\perp}(\theta_s) &= \frac{\lambda^2}{4\pi} \frac{4i_1}{x^2} = \frac{\lambda^2}{\pi x^2} |S_1(\theta_s)|^2, \\ \sigma_{\text{sca}\parallel}(\theta_s) &= \frac{\lambda^2}{4\pi} \frac{4i_2}{x^2} = \frac{\lambda^2}{\pi x^2} |S_2(\theta_s)|^2. \end{aligned} \quad (9)$$

2.3. Link geometry

The geometry of the link (altitude and elevation of the antennas) is an important factor in the scattering calculation. The geometry has to be taken into account in order to accurately calculate the line-of-sight distances and R_1 and R_2 . A difference in altitude between the receiver and transmitter antenna results in a nonhorizontal scattering plane. The scattering plane is defined as the plane formed by the transmitter and receiver antenna points and the center point of the common volume. It is convenient to specify the orientations of the antennas related to the local horizontal plane. In general, the scattering plane will not be parallel to the horizontal plane. Therefore the horizontal and vertical orientation vectors of the transmitted signal related to the scattering plane must first be calculated. Following this, the bistatic scattering may be calculated and the resulting signal may be transformed into the local horizontal and vertical coordinate planes of the receiver antenna. It is vital that the impact of link geometry on the bistatic coupling be taken into account as it has in the analysis presented here.

2.4. Attenuation

Gaseous attenuation due to oxygen and attenuation due to rain are the dominant contributors to excess attenuation on the link path from the transmitter to the receiver. Water vapor attenuation is negligible by comparison.

The oxygen molecule has a permanent magnetic moment which gives rise to frequency-dependent absorption of incident electromagnetic energy. When an electromagnetic wave impinges on an oxygen molecule, electrons transit within a single electron state. This interaction happens only at the resonant frequencies of the electrons. Between 58 and 66 GHz

there are 16 resonant frequencies, which results in significant oxygen attenuation centered around 60 GHz. For standard atmospheric conditions at sea level this is typically between 12 and 16 dB km⁻¹.

In 1985, Liebe proposed the microwave propagation model (MPM) to describe oxygen attenuation. This model has been well tested and is often used for modeling the gaseous attenuation, especially when the 60 GHz band is included in the frequency range. Further detailed discussion on the microwave propagation model can be found in [9–11].

The path attenuation due to rain is determined from ITU-R recommendation P.838-2 [12].

2.5. Drop size distribution

Many models have been proposed for raindrop size distribution. However, because of the high degree of variability of drop size distribution with time and location, finding a model that accurately represents observations is fraught with difficulty. In the absence of other data, the distribution that fitted best to the observed data was the Marshall-Palmer distribution. Uncertainty in the drop size distribution is one of the largest sources of errors in the bistatic scattering model.

3. VALIDATION OF THE MODEL

During the development of the model, results were regularly checked with other programs. The scattering calculations were checked with the program MiePlot [13]. Although it was designed for light scattering, the Mie theory is valid for all frequencies and therefore the model could be compared with this program. A good agreement between the model and the results of MiePlot was found.

4. MODEL VERSUS MEASUREMENTS

As part of an Ofcom study, rain scattering measurements at 60 GHz were made by QinetiQ [5, 6]. For the measurements, an experimental propagation link was established using a wideband channel-sounder. The transmitter antenna was fed with an RF power of +5.1 dBm. The transmitter and receiver antennas were lens horn antennas with a gain of 34.5 dBi. The beamwidth of the antennas was 3° which is comparable with that of typical commercial equipment. The receiver noise bandwidth was 120 MHz. The antennas were located in two buildings at QinetiQ's Great Malvern site, with a line-of-sight distance of 75 m.

For a 45° scattering angle, Figure 1 shows the measured received power, together with the calculated power (derived from the theoretical model) and the associated rainfall rate. It can be seen that there is good agreement between the calculated power and the measured data. Note that even the modest rainfall rates of this event can cause significant bistatic coupling.

Similar good agreement between the model and measurements was observed for several other events confirming the validity of the model.

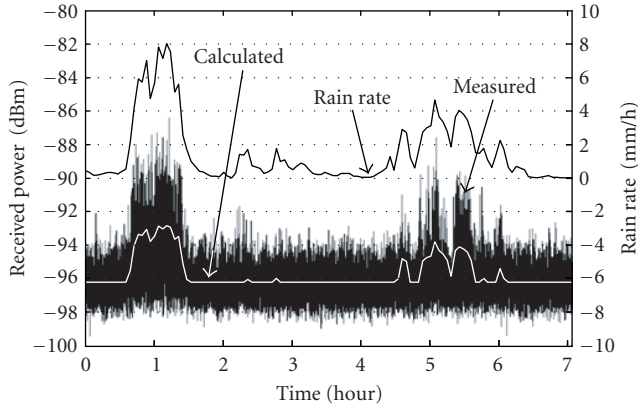


FIGURE 1: Received and calculated scattered power versus the rain rate.

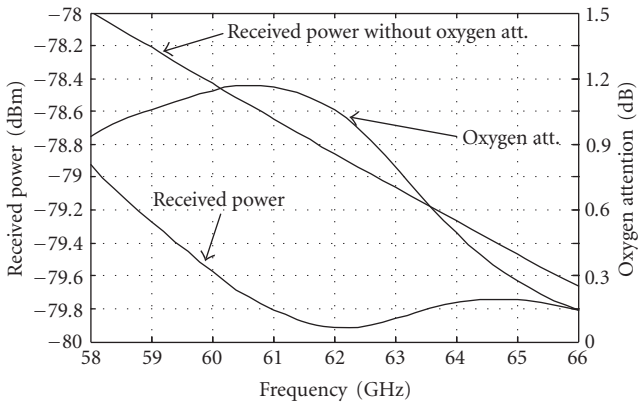


FIGURE 2: Influence of the frequency on received power.

5. MODELING 60 GHZ SCATTERING

Using the model, several scenarios were investigated to study the behavior of rain-induced bistatic scattering at 60 GHz. This analysis was performed to determine the general behavior in the case of link configurations not experimentally measured. This analysis highlighted some interesting results.

5.1. Influence of frequency

For the same link geometry as that of Figure 1, the frequency dependence from 58 GHz to 66 GHz was investigated. From Figure 2 it can be seen that the received power without taking the oxygen attenuation into account shows a linear decrease for increasing frequency. However, taking into account the significant oxygen attenuation around 61 GHz changes the trend of the received power for frequencies above 62 GHz.

5.2. Scattering angle

The scattering angle can be formed by many different combinations of the antenna orientations, with two extremes: the

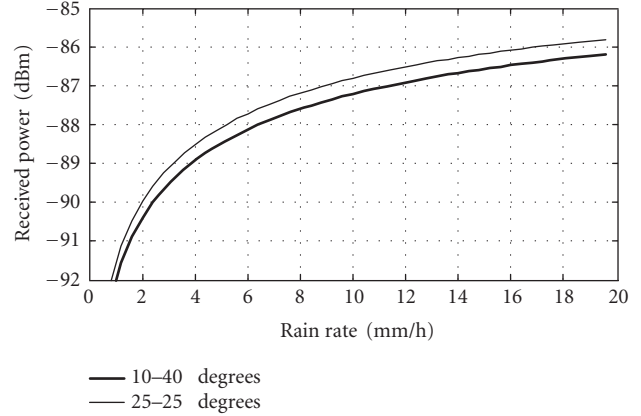


FIGURE 3: Received power versus rain rate for the same system settings and a different path orientation.

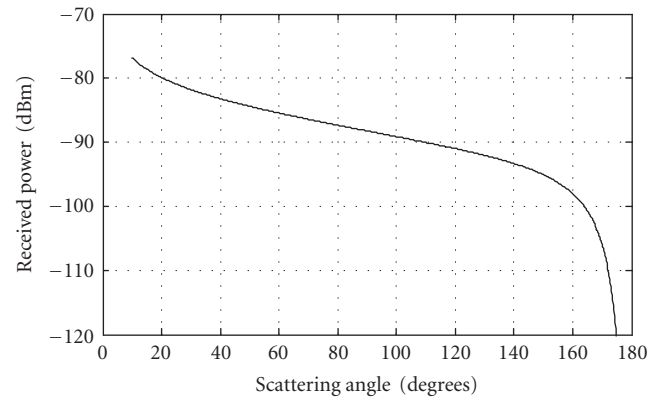


FIGURE 4: Received power versus scattering angle.

orientation of the transmitter and receiver antennas is the same (e.g., 40-40 degrees) or the orientation of one of the antennas is minimal and the other maximal (e.g., 10-70 degrees). The path length in case of the same orientation angle is larger than when the antenna orientations are maximally different. This results in a lower received scattered power. But the common volume for the same-orientation case is larger, resulting in more received scattered power. From the model simulations it appears that both effects almost cancel each other. The largest difference noticed is 0.5 dB in received power (see Figure 3), which is minimal.

The influence of the scattering angle on the received power was further investigated. Therefore an angular sweep of the scattering angle from 20 to 180 degrees was performed. This result is shown in Figure 4. This result is as one would intuitively expect; strong forward scattering and very weak backward scattering. This behavior has also been found at 94 GHz [4], therefore it confirms the model behavior.

6. CONCLUSION

A theoretical model for the calculation of bistatic scattering at 60 GHz has been presented. The theoretical model shows

good agreement with experimental data. It demonstrates that the first-order multiple scattering is sufficient to describe bistatic scattering by rain at 60 GHz. Using Mie theory for individual scattering by water spheres, we show that the bistatic scattered power reaches a maximum, which depends on the value of the scattering angle, the line-of-sight distance, and the frequency.

The modeling of the measured rain events shows that the model can predict the received scattered power for any configuration of interfering link. It is shown that the path orientation does not affect the received power very much, for constant system settings. The scattering angle does affect the received power very much, but the behavior it shows was expected, and confirms the model behavior.

This model shows good agreement between measured and calculated received powers. This shows that there is a relationship between scattered power and the rain rate, which can also be predicted, provided by the drop size distribution.

In the context of the wide deployment of 60 GHz links, it should be noted that coupling between adjacent links caused by bistatic scattering could be significant even in light rain ($<3 \text{ mm h}^{-1}$). This occurs in spite of the high oxygen attenuation. The effects of variable raindrop size distribution can also be significant. Although best agreement between model and measurements was found using a Marshall-Palmer raindrop size distribution, it should be noted that in many cases the Marshall-Palmer distribution can substantially overestimate the number of smaller raindrops, and therefore overestimate the scattered power. The use of the Marshall-Palmer distribution does however provide a “worst case” estimate that may be useful when considering high-availability links.

ACKNOWLEDGMENTS

We thank D. Eden of Ofcom and A. Shukla of QinetiQ for making available the experimental data used in this study. The data were collected under Ofcom Contract AY4497.

REFERENCES

- [1] A. Ishimaru, *Wave Propagation and Scattering in Random Media*, IEEE Press and Oxford University Press, New York, NY, USA, 1997.
- [2] M. Kerker, *The Scattering of Light and Other Electromagnetic Radiation*, Academic Press, London, UK, 1969.
- [3] R. K. Crane, “Bistatic scatter from rain,” *IEEE Transactions on Antennas and Propagation*, vol. 22, no. 2, pp. 312–320, 1974.
- [4] C. Gloaguen and L. Lavergnat, “94 GHz bistatic scattering in rain,” *IEEE Transactions on Antennas and Propagation*, vol. 44, no. 9, pp. 1247–1258, 1996.
- [5] R. M. Swindell and D. J. Fraser, “Improving spectrum utilization at 58-66GHz through an accurate assessment of rain scatter interference phase 1 report,” QinetiQ/03/00084, 2003, unpublished.
- [6] R. M. Swindell, D. J. Fraser, and R. J. Watson, “Improving spectrum utilization at 58-66 GHz through an accurate assessment of rain scatter interference phase 2 report,” AY4487, QinetiQ, 2004, unpublished.
- [7] T. Oguchi, “Electromagnetic wave propagation and scattering in rain and other hydrometers,” *Proceedings of the IEEE*, vol. 71, no. 9, pp. 1029–1078, 1983.
- [8] H. C. van de Hulst, *Light Scattering by Small Particles*, Dover, New York, NY, USA, 1981.
- [9] H. J. Liebe, “MPM—an atmospheric millimeter-wave propagation model,” *International Journal of Infrared and Millimeter Waves*, vol. 10, no. 6, pp. 631–650, 1989.
- [10] A. C. Valdez, “Analysis of atmospheric effects due to atmospheric oxygen on a wideband digital signal in the 60 GHz band,” M.S. thesis, Department of Electrical Engineering, Virginia Polytechnic Institute and State University, Blacksburg, Va, USA, 2001.
- [11] G. Brussaard and P. A. Watson, *Atmospheric Modelling and Millimetre Wave Propagation*, Chapman & Hall, London, UK, 1995.
- [12] “Specific Attenuation Model for Rain for Use in Prediction Methods,” ITU-R, Recommendation P.838-2, 2003.
- [13] P. Laven, “MiePlot a computer program for scattering of light from a sphere using Mie theory & the Debye series,” January 2006, <http://www.philiplaven.com/mieplot.htm>.

Research Article

Comparison of OQPSK and CPM for Communications at 60 GHz with a Nonideal Front End

Jimmy Nsenga,^{1,2} Wim Van Thillo,^{1,2} François Horlin,¹ André Bourdoux,¹ and Rudy Lauwereins^{1,2}

¹IMEC, Kapeldreef 75, 3001 Leuven, Belgium

²Departement Elektrotechniek - ESAT, Katholieke Universiteit Leuven, Kasteelpark Arenberg 10, 3001 Leuven, Belgium

Received 4 May 2006; Revised 14 November 2006; Accepted 3 January 2007

Recommended by Su-Khiong Yong

Short-range digital communications at 60 GHz have recently received a lot of interest because of the huge bandwidth available at those frequencies. The capacity offered to the users could finally reach 2 Gbps, enabling the deployment of new multimedia applications. However, the design of analog components is critical, leading to a possible high nonideality of the front end (FE). The goal of this paper is to compare the suitability of two different air interfaces characterized by a low peak-to-average power ratio (PAPR) to support communications at 60 GHz. On one hand, we study the offset-QPSK (OQPSK) modulation combined with a channel frequency-domain equalization (FDE). On the other hand, we study the class of continuous phase modulations (CPM) combined with a channel time-domain equalizer (TDE). We evaluate their performance in terms of bit error rate (BER) considering a typical indoor propagation environment at 60 GHz. For both air interfaces, we analyze the degradation caused by the phase noise (PN) coming from the local oscillators; and by the clipping and quantization errors caused by the analog-to-digital converter (ADC); and finally by the nonlinearity in the PA.

Copyright © 2007 Jimmy Nsenga et al. This is an open access article distributed under the Creative Commons Attribution License, which permits unrestricted use, distribution, and reproduction in any medium, provided the original work is properly cited.

1. INTRODUCTION

We are witnessing an explosive growth in the demand for wireless connectivity. Short-range wireless links like wireless local area networks (WLANs) and wireless personal area networks (WPANs) will soon be expected to deliver bit rates of over 1 Gbps to keep on satisfying this demand. Fast wireless download of multimedia content and streaming high-definition TV are two obvious examples. As lower frequencies (below 10 GHz) are getting completely congested though, bandwidth for these Gbps links has to be sought at higher frequencies. Recent regulation assigned a 3 GHz wide, worldwide available frequency band at 60 GHz to this kind of applications [1].

Communications at 60 GHz have some advantages as well as some disadvantages. The main advantages are three-fold. The large unlicensed bandwidth around 60 GHz (more than 3 GHz wide) will enable very high data rate wireless applications. Secondly, the high free space path loss and high attenuation by walls simplify the frequency reuse over small distances. Thirdly, as the wavelength in free space is only 5 mm, the analog components can be made small. Therefore, on a small area, one can design an array of antennas, which

steers the beam in a given target direction. This improves the link budget and reduces the time dispersion of the channel. Opposed to this are some disadvantages: the high path loss will restrict communications at 60 GHz to short distances, more stringent requirements are put on the analog components (like multi-Gsamples/s analog-to-digital converter ADC), and nonidealities of the radio frequency (RF) front end have a much larger impact than at lower frequencies. The design of circuits at millimeter waves is more problematic than at lower frequencies for two important reasons. First, the operating frequency is relatively close to the cut-off frequency and to the maximum oscillation frequency of nowadays' complementary metal oxide semiconductor (CMOS) transistors (e.g., the cut-off frequency of a transistor in a 90 nm state-of-the-art CMOS is around 150 GHz [2]), reducing significantly the design freedom. Second, the wavelength approaches the size of on-chip dimensions so that the interconnects have to be modeled as (lossy) transmission lines, complicating the modeling and circuit simulation and also the layout of the chip.

A suitable air interface for low-cost, low-power 60 GHz transceivers should thus use a modulation technique that has a high level of immunity to FE nonidealities (especially phase

noise (PN) and ADC quantization and clipping), and allows an efficient operation of the power amplifier (PA). Since the 60 GHz channel has been shown to be frequency selective for very large bandwidths and low antenna gains [3, 4], orthogonal frequency division multiplexing (OFDM) has been proposed for communications at 60 GHz. However, it is very sensitive to nonidealities such as PN and carrier frequency offset (CFO). Moreover, due to its high PAPR, it requires the PA to be backed off by several dB more than for a single carrier (SC) system, thus lowering the power efficiency of the system.

Therefore, we consider two other promising air interfaces that relax the FE requirements. First, we study an SC transmission scheme combined with OQPSK because it has a lower PAPR than regular QPSK or QAM in band-limited channels. As the multipath channel should be equalized at a low complexity, we add redundancy at the transmitter to make the signal cyclic and to be able to equalize the channel in the frequency domain [5]. Secondly, we study CPM techniques [6]. These have a perfectly constant amplitude, or a PAPR of 0 dB. Moreover, their continuous phase property results in lower spectral sidelobes. Linear representations and approximations developed by Laurent [7] and Rimoldi [8] allow for great complexity reductions in the equalization and detection processes. In order to mitigate the multipath channel, a conventional convolutive zero-forcing (ZF) equalizer is used.

The goal of this paper is to analyze, by means of simulations, the impact of three of the most critical building blocks in RF transceivers, and to compare the robustness of the two air interfaces to their nonideal behavior:

- (i) the mixing stage where the local oscillator PN can be very high at 60 GHz,
- (ii) the ADC that, for low-power consumption, must have the lowest possible resolution (number of bits) given the very high bit rate,
- (iii) the PA where nonlinearities cause distortion and spectral regrowth.

The paper is organized as follows. In Section 2, we describe the indoor channel at 60 GHz. Section 3 describes the considered FE nonidealities. Sections 4 and 5 introduce the OQPSK and CPM air interfaces, respectively, together with their receiver design. Simulation setup and results are provided in Section 6 and the conclusions are drawn in Section 7.

Notation

We use roman letters to represent scalars, single underlined letters to denote column vectors, and double underlined letters to represent matrices. $[\cdot]^T$ and $[\cdot]^H$ stand for transpose and complex conjugate transpose operators, respectively. The symbol \star denotes the convolution operation and \otimes the Kronecker product. \underline{I}_k is the identity matrix of size $k \times k$ and $\underline{0}_{m \times n}$ is an $m \times n$ matrix with all entries equal to 0.

2. THE INDOOR 60 GHZ CHANNEL

2.1. Propagation characteristics

The interest in the 60 GHz band is motivated by the large amount of unlicensed bandwidth located between 57 and 64 GHz [1, 9]. Analyzing the spectrum allocation in the United States (US), Japan, and Europe, one notices that there is a common contiguous 3 GHz bandwidth between 59 and 62 GHz that has been reserved for high data rate applications. This large amount of bandwidth can be exploited to establish a wireless connection at more than 1 Gbps.

Different measurement campaigns have been carried out to characterize the 60 GHz channel. The free space loss (FSL) can be computed using the Friis formula (1) as follows:

$$\text{FSL [dB]} = 20 \times \log_{10} \left(\frac{4\pi d}{\lambda} \right), \quad (1)$$

where λ is signal wavelength and d is the distance of the terminal from the transmitter base station. One can see that the FLS is already 68 dB at 1 m separation away from the transmitter. Thus, given the limited transmitted power, the communication range will hardly extend over 10 m. Besides the FSL, reflection and penetration losses of objects at 60 GHz are higher than at lower frequencies [10, 11]. For instance, concrete walls 15 cm thick attenuate the signal by 36 dB. They act thus as real boundaries between different rooms.

However, the signals reflected off the concrete walls have a sufficient amplitude to contribute to the total received power, thus making the 60 GHz channel a multipath channel [3, 12]. Typical root mean-square (RMS) delay spreads at 60 GHz can vary from 10 nanoseconds to 100 nanoseconds if omni-directional antennas are used, depending on the dimensions and reflectivity of the environment [3]. However, the RMS delay spread can be greatly reduced to less than 1 nanosecond by using directional antennas, thus increasing the coherence bandwidth of the channel up to 200 MHz [13].

Moreover, the objects moving within the communication environment make the channel variant over time. Typical values of Doppler spread at 60 GHz are around 200 Hz at a normal walking speed of 1 millisecond. This results in a coherence time of approximately 1 millisecond. With a symbol period of 1 nanosecond, 10^6 symbols can be transmitted in a quasistatic environment. Thus, Doppler spread at 60 GHz will not have a significant impact on the system performance.

In summary, 60 GHz communications are mainly suitable for short-range communications due to the high propagation loss. The channel is frequency selective due to the large bandwidth used (more than 1 GHz). However, one can assume the channel to be time invariant during the transmission of one block.

2.2. Channel model

In this study, we model the indoor channel at 60 GHz using the Saleh-Valenzuela model [14], which assumes that the

received signals arrive in clusters. The rays within a cluster have independent uniform phases. They also have independent Rayleigh amplitudes whose variances decay exponentially with cluster and rays delays. In the Saleh-Valenzuela model, the cluster decay factor is denoted by Γ and the rays decay factor is represented by γ . The clusters and the rays form Poisson arrival processes that have different, but fixed rates Λ and λ , respectively [14].

We consider the same scenario as that defined in [15]. The base station has an omni-directional antenna with 120° beam width and is located in the center of the room. The remote station has an omni-directional antenna with 60° beam width and is placed at the edge of the room. The corresponding Saleh-Valenzuela parameters are presented in Table 1.

3. NONIDEALITIES IN ANALOG TRANSCEIVERS

In this section, we introduce 3 FE nonidealities: ADC clipping and quantization, PN and nonlinearity of the PA. The rationale for choosing these 3 nonidealities is that a good PA, a high resolution ADC, and a low PN oscillator have a high power consumption [16].

3.1. Clipping and quantization

3.1.1. Motivation

The number of bits (NOB) of the ADC must be kept as low as possible for obvious reasons of cost and power consumption. On the other hand, a large number of bits is desirable to reduce the effect of quantization noise and the risk of clipping the signal. Clipping occurs when the signal fluctuation is larger than the dynamic range of the ADC. Without going into detail, we mention that there is always an optimal clipping level for a given NOB. As the clipping level is increased, the signal degradation due to clipping is reduced. However, the degradation due to quantization is increased as a larger dynamic range must be covered with the same NOB. For a more elaborate discussion, we refer to [17].

3.1.2. Model

The ADC is thus characterized by two parameters: the NOB and the normalized clipping level μ , which is the ratio of the clipping level to the RMS value of the amplitude of the signal. In Figure 1, we illustrate the clipping/quantization function for an NOB = 3. This simple model is used in our simulations in Section 6.4.

3.2. Phase noise

3.2.1. Motivation

PN originates from nonideal clock oscillators, voltagecontrolled oscillators (VCO), and frequency synthesis circuits. In the frequency domain, PN is most often characterized by the power spectral density (PSD) of the the oscillator phase $\phi(t)$. The PSD of an ideal oscillator has only a Dirac pulse at its carrier frequency, corresponding to no phase fluctuation

TABLE 1: Saleh-Valenzuela channel parameters at 60 GHz.

$1/\Lambda$	75 nanoseconds
Γ	20 nanoseconds
$1/\lambda$	5 nanoseconds
γ	9 nanoseconds

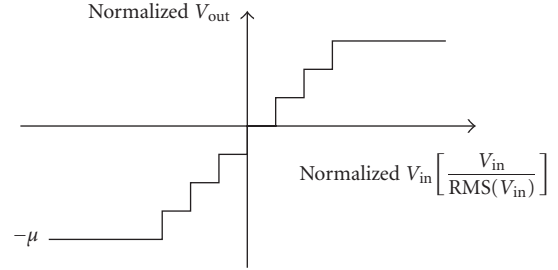


FIGURE 1: ADC input-output characteristic.

at all. In practice, the PSD of the phase exhibits a 20 dB/dec decreasing behavior as the offset from the carrier frequency increases. Nonmonotonic behavior is attributable to, for example, phase-locked loop (PLL) filters in the frequency synthesis circuit.

3.2.2. Model

We characterize the phase noise by a set of 3 parameters (see Figure 2) [18]:

- (i) the integrated PSD denoted K , expressed in dBc, which is the two-sided integral of the phase noise PSD,
- (ii) the 3 dB bandwidth,
- (iii) the VCO noise floor.

Note that these 3 parameters will fix the value of the PN PSD at low frequency offsets. In our simulations (see Section 6.3), we assume a phase noise bandwidth of 1 MHz and a noise floor of -130 dBc/Hz. Typical values of the level of PN PSD at 1 MHz are considered [19] and the corresponding integrated PSD is calculated in Table 2. In order to generate a phase noise characterized by the PSD illustrated in Figure 2, a white Gaussian noise is convolved with a filter whose frequency domain response is equal to the square root of the PSD.

3.3. Nonlinear power amplification

3.3.1. Motivation

Nonlinear behavior can occur in any amplifier but it is more likely to occur in the last amplifier of the transmitter where the signal power is the highest. For power consumption reasons, this amplifier must have a saturated output power that is as low as possible, compatible with the system level constraints such as transmit power and link budget. The gain characteristic of an amplifier is almost perfectly linear at low

TABLE 2: Simulated integrated PSD.

PN @1 MHz [dBc/Hz]	Integrated PSD [dBc]
-90	-24
-85	-20
-82	-16

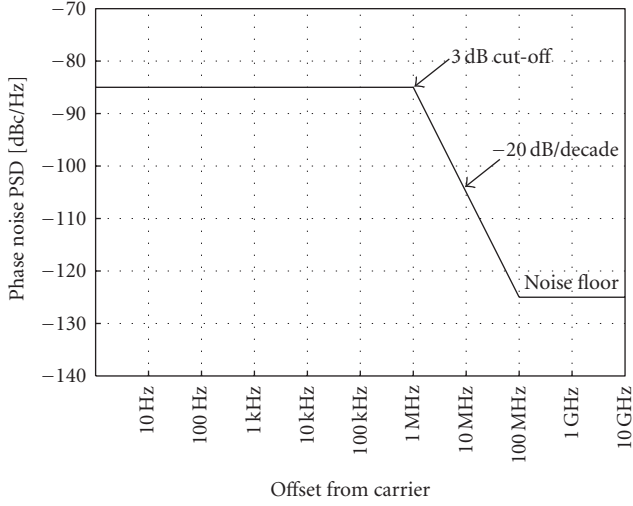


FIGURE 2: Piecewise linear phase noise PSD definition used in the phase noise model.

input level and, for increasing input power, deviates from the linear behavior as the input power approaches the 1-dB compression point ($P_{1\text{ dB}}$: the point at which the gain is reduced by 1-dB because the amplifier is driven into saturation) and eventually reaches complete saturation. The input third-order intercept point (IP_3) is also often used to quantify the nonlinear behavior of amplifiers. It is the input power at which the power of the two-tone third-order intermodulation product would become equal to the power of the first-order term. When peaks are present in the transmitted waveform, one has to operate the PA with a few dBs of backoff to prevent distortion. This backoff actually reduces the power efficiency of the PA and must be kept to a minimum.

3.3.2. Model

In our simulation (see Section 6.5), we characterize the nonlinearity of the PA by a third-order nonlinear equation

$$y(t) = a_1 x(t) + a_3 |x(t)|^2 x(t), \quad (2)$$

where $x(t)$ and $y(t)$ are the baseband equivalent PA input and output, respectively, a_1 and a_3 are real polynomial coefficients. We assume an amplifier with a unity gain ($a_1 = 1$) and an input amplitude at 1-dB compression point $A_{1\text{ dB}}$ normalized to 1. Therefore, by using (3), one can compute the third-order coefficient a_3

$$a_3 = -0.145 \frac{a_1}{A_{1\text{ dB}}^2}. \quad (3)$$

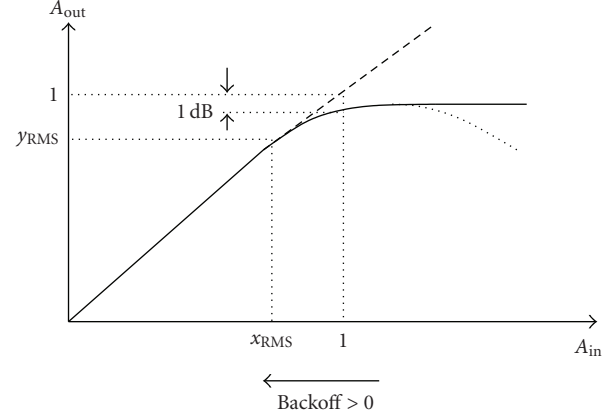


FIGURE 3: PA input-output power characteristic.

The parameter a_3 is then equal to -0.145 . Note that (2) models only the amplitude-to-amplitude (AM-AM) conversion of a nonlinear PA. In order to make our model more realistic, a saturation level is set from the extremum of the cubic function. The root mean-square (RMS) value of the input PA signal is computed and its level is adapted according to the backoff requirement. The backoff is defined relative to $A_{1\text{ dB}}$ and is the only varying parameter. Then the nonlinearity is introduced using the AM-AM conversion as shown in Figure 3.

4. OFFSET QPSK WITH FREQUENCY DOMAIN EQUALIZATION

4.1. Initial concept

Offset-QPSK, a variant of QPSK digital modulation, is characterized by a half symbol period delay between the data mapped on the quadrature (Q) branch and the one mapped on the inphase (I) branch. This offset imposes that either the I or the Q signal changes during the half symbol period. Consequently, the phase shift between two consecutive OQPSK symbols is limited to $\pm 90^\circ$ ($\pm 180^\circ$ in conventional QPSK modulation), thus avoiding the amplitude of the signal to go through the “0” point. The advantage of an OQPSK modulated signal over QPSK signal is observed in band-limited channels where nonrectangular pulse shaping, for instance, root raised root cosine, is used. The envelope fluctuation of an OQPSK signal is found to be 70% lower than that of a conventional QPSK signal [20]. Thus, OQPSK is considered to be a low PAPR modulation scheme, for which a nonlinear PA with less backoff can be used, thus increasing the power efficiency of the system.

4.2. System model

Our system model is inspired from the model of Wang and Giannakis [21]. Let us consider the baseband block transmitter model represented in Figure 4. The inphase component of the digital OQPSK signal is denoted by $u_I[k]$ and

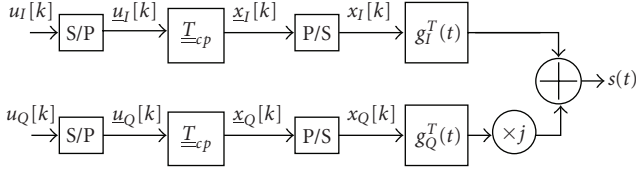


FIGURE 4: Offset QPSK block transmission.

the quadrature-phase component denoted by $u_Q[k]$. The two streams are first serial-to-parallel (S/P) converted to form blocks $\underline{u}_I[k] := [u_I[kB], u_I[kB+1], \dots, u_I[kB+B-1]]^T$ and $\underline{u}_Q[k] := [u_Q[kB], u_Q[kB+1], \dots, u_Q[kB+B-1]]^T$ where B is the block size. Then, a cyclic prefix (CP) of length N_{cp} is inserted at the beginning of each block to get cyclic blocks $\underline{x}_I[k]$ and $\underline{x}_Q[k]$. The cyclic prefix insertion is done by multiplying both $\underline{u}_I[k]$ and $\underline{u}_Q[k]$ with the matrix $\underline{T}_{cp} = \begin{bmatrix} 0_{N_{cp} \times (B-N_{cp})} & \underline{I}_{N_{cp}} \\ \underline{I}_B & 0_{(B-N_{cp}) \times N_{cp}} \end{bmatrix}$ of size $(B+N_{cp}) \times B$. In a practical system, the N_{cp} should be larger than the channel impulse response length, and the size of the block B is chosen so that the CP overhead is limited (practically an overhead of 1/5 is often used). The size B should on the other hand be as small as possible to reduce the complexity and to ensure that the channel is constant within one symbol block duration. The cyclic blocks $\underline{x}_I[k]$ and $\underline{x}_Q[k]$ are afterwards converted back to serial streams and the resulting streams $x_I[k]$ and $x_Q[k]$ of sample duration equal to T are filtered by square root raised cosine filters $g_I^T(t)$ and $g_Q^T(t)$, respectively. The inherent offset between I and Q branches, which differentiates the OQPSK signaling from the normal QPSK, is modeled through the pulse-shaping filters defined such that $g_Q^T(t) = g_I^T(t - T/2)$. The two pulse-shaped signals are then summed together to form the equivalent complex lowpass transmitted signal $s(t)$.

The signal $s(t)$ is then transmitted through a frequency selective channel, which we model by its equivalent lowpass channel impulse response $c(t)$. Figure 5 shows a block diagram of the receiver. The received signal $r_{in}(t)$ is corrupted by additive white Gaussian noise (AWGN), $n(t)$, generated by analog FE components. The noisy received signal is first lowpass-filtered by an anti-aliasing filter with ideal lowpass specifications before the discretization. We consider the following two sample rates.

- (i) The nonfractional sampling (NFS) rate which corresponds to sampling the analog signal every T seconds. The corresponding anti-aliasing filter, denoted $g_{NFS}^R(t)$, eliminates all the frequencies above $0.5/T$.
- (ii) The fractional sampling (FS) rate for which the sampling period is $T/2$ seconds. The cutoff frequency of the anti-aliasing filter $g_{FS}^R(t)$ is set to $1/T$.

More information about the two sampling modes can be found in [22]. In the sequel, we focus on the FS case. The NFS can be seen as a special case of FS. In order to characterize the received signal, we define $h_I(t) := g_I^T(t) \star c(t) \star g_{FS}^R(t)$ and $h_Q(t) := j \star g_Q^T(t) \star c(t) \star g_{FS}^R(t)$ as the overall channel impulse response encountered by data symbols on I and Q , respectively. The received signal after lowpass filtering is

given by

$$r(t) = \sum_k x_I[k] h_I(t - kT) + \sum_k x_Q[k] h_Q(t - kT) + v(t) \quad (4)$$

in which $v(t)$ is the lowpass filtered noise. The analog received signal $r(t)$ is then sampled every $T/2$ seconds to get the discrete-time sequence $r[m]$.

As explained in [22], fractionally sampled signals are processed by creating polyphase components, where even and odd indexed samples of the received signal are separated. In the following, the index “0” is related to even samples or polyphase component “0” while odd samples are represented by index “1” or polyphase component “1.” Thus, we define

$$\begin{aligned} r^\rho[m] &\stackrel{\text{def}}{=} r[2m + \rho], \\ v^\rho[m] &\stackrel{\text{def}}{=} v[2m + \rho], \\ h_I^\rho[m] &\stackrel{\text{def}}{=} h_I[2m + \rho], \\ h_Q^\rho[m] &\stackrel{\text{def}}{=} h_Q[2m + \rho], \end{aligned} \quad (5)$$

where ρ denotes either the polyphase component “0” or the polyphase component “1,” $r[m]$ and $v[m]$ are, respectively, the received signal $r(t)$ and the noise $v(t)$ sampled every $T/2$ seconds, $h_I[m]$ and $h_Q[m]$ represent the discrete-time version of, respectively, $h_I(t)$ and $h_Q(t)$ sampled every $T/2$ seconds. The sampled channels $h_I^\rho[m]$ and $h_Q^\rho[m]$ have finite impulse responses, of length L_I and L_Q , respectively. These time dispersions cause the intersymbol interference (ISI) between consecutive symbols, which, if not mitigated, degrades the performance of the system. Next to the separation in polyphase components, we separate the real and imaginary parts of different polyphase signals. Starting from now, we use the supplementary upper index $c = \{r, i\}$ to identify the real or imaginary parts of the sequences.

The four real-valued sequences $r^{\rho c}[m]$ are serial to parallel converted to obtain the blocks $\underline{r}^{\rho c}[m] := [r^{\rho c}[mB], r^{\rho c}[mB+1], \dots, r^{\rho c}[mB+B+N_{cp}-1]]^T$ of $(B+N_{cp})$ samples. The corresponding transmit-receive block relationship, assuming a correct time and frequency synchronization, is given by

$$\begin{aligned} \underline{r}^{\rho c}[m] &= \underline{H}_I^{\rho c}[0] \underline{T}_{cp} \underline{u}_I[m] + \underline{H}_I^{\rho c}[1] \underline{T}_{cp} \underline{u}_I[m-1] \\ &\quad + \underline{H}_Q^{\rho c}[0] \underline{T}_{cp} \underline{u}_Q[m] + \underline{H}_Q^{\rho c}[1] \underline{T}_{cp} \underline{u}_Q[m-1] \\ &\quad + \underline{v}^{\rho c}[m], \end{aligned} \quad (6)$$

where $\underline{v}^{\rho c}[m]$ is the m th filtered noise block defined as $\underline{v}^{\rho c}[m] := [v^{\rho c}[mB], v^{\rho c}[mB+1], \dots, v^{\rho c}[mB+B+N_{cp}-1]]^T$. The square matrices $\underline{H}_X^{\rho c}[0]$ and $\underline{H}_X^{\rho c}[1]$ of size $(B+N_{cp}) \times (B+N_{cp})$, with X equal to I or Q , are represented in the following

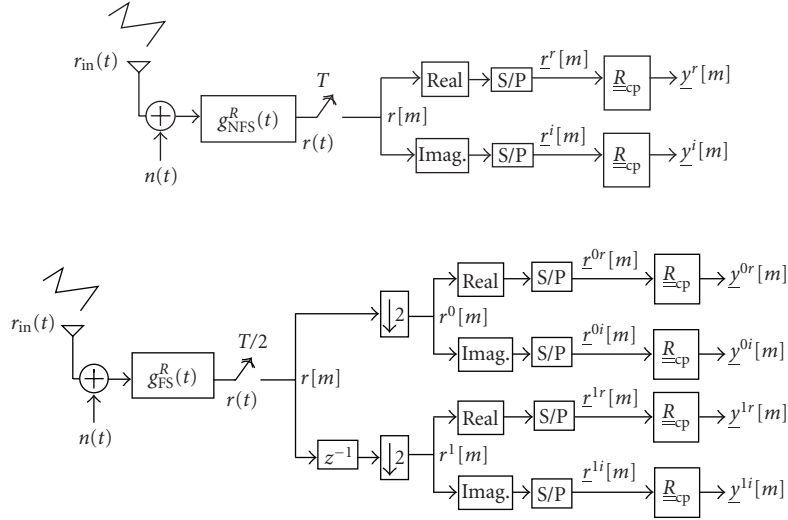


FIGURE 5: Receiver: upper part NFS, lower part FS.

equations:

$$\underline{H}_X^{\rho c}[0] = \begin{bmatrix} h_X^{\rho c}[0] & 0 & 0 & \cdots & 0 \\ \vdots & h_X^{\rho c}[0] & 0 & \cdots & 0 \\ h_X^{\rho c}[L_X] & \cdots & \ddots & \cdots & 0 \\ \vdots & \ddots & \cdots & \ddots & 0 \\ 0 & \cdots & h_X^{\rho c}[L_X] & \cdots & h_X^{\rho c}[0] \end{bmatrix}, \quad (7)$$

$$\underline{H}_X^{\rho c}[1] = \begin{bmatrix} 0 & \cdots & h_X^{\rho c}[L_X] & \cdots & h_X^{\rho c}[1] \\ \vdots & \ddots & 0 & \ddots & \vdots \\ 0 & \cdots & \ddots & \cdots & h_X^{\rho c}[L_X] \\ \vdots & \vdots & \cdots & \ddots & \vdots \\ 0 & \cdots & 0 & \cdots & 0 \end{bmatrix}.$$

The second and the fourth terms in (6) highlight the inter-block interference (IBI) that arises between consecutive blocks due to the time dispersion of the channel. The IBI between consecutive blocks $\underline{u}_I[m]$ or $\underline{u}_Q[m]$ is afterwards eliminated by discarding the first N_{cp} samples in each received block. This operation is carried out by multiplying the received blocks in (6) by a guard removal matrix $\underline{R}_{cp} = [\underline{0}_{B \times N_{cp}}, \underline{I}_B]$ of size $B \times (B + N_{cp})$. We get

$$\begin{aligned} \underline{y}^{\rho c}[m] &\stackrel{\text{def}}{=} \underline{R}_{cp} \underline{r}^{\rho c}[m] = \underline{R}_{cp} \underline{H}_I^{\rho c}[0] \underline{T}_{cp} \underline{u}_I[m] \\ &+ \underline{R}_{cp} \underline{H}_I^{\rho c}[1] \underline{T}_{cp} \underline{u}_I[m-1] + \underline{R}_{cp} \underline{H}_Q^{\rho c}[0] \underline{T}_{cp} \underline{u}_Q[m] \\ &+ \underline{R}_{cp} \underline{H}_Q^{\rho c}[1] \underline{T}_{cp} \underline{u}_Q[m-1] + \underline{R}_{cp} \underline{v}^{\rho c}[m]. \end{aligned} \quad (8)$$

As N_{cp} has been chosen to be larger than the $\max\{L_I, L_Q\}$, the product of \underline{R}_{cp} and each of $\underline{H}_I^{\rho c}[1]$ and $\underline{H}_Q^{\rho c}[1]$ matrices is null. Moreover, the left and right cyclic prefix insertion and removal operations around $\underline{H}_I^{\rho c}[0]$ and $\underline{H}_Q^{\rho c}[0]$, described mathematically as $\underline{R}_{cp} \underline{H}_I^{\rho c}[0] \underline{T}_{cp}$ and $\underline{R}_{cp} \underline{H}_Q^{\rho c}[0] \underline{T}_{cp}$,

respectively, result in circulant matrices $\underline{H}_I^{\rho c}$ and $\underline{H}_Q^{\rho c}$ of size $(B \times B)$. Finally, the discrete-time block input-output relationship taking the CP insertion and removal operations into account is

$$\underline{y}^{\rho c}[m] = \underline{H}_I^{\rho c} \underline{u}_I[m] + \underline{H}_Q^{\rho c} \underline{u}_Q[m] + \underline{w}^{\rho c}[m] \quad (9)$$

in which $\underline{w}^{\rho c}[m]$ is obtained by discarding the first N_{cp} samples from the filtered noise block $\underline{v}^{\rho c}[m]$. By stacking the real and the imaginary parts of the two polyphase components on top of each other, the matrix representation of the FS case is

$$\begin{bmatrix} y^{0r}[m] \\ y^{0i}[m] \\ y^{1r}[m] \\ y^{1i}[m] \end{bmatrix} = \underbrace{\begin{bmatrix} \underline{H}_I^{0r} & \underline{H}_Q^{0r} \\ \underline{H}_I^{0i} & \underline{H}_Q^{0i} \\ \underline{H}_I^{1r} & \underline{H}_Q^{1r} \\ \underline{H}_I^{1i} & \underline{H}_Q^{1i} \end{bmatrix}}_{\underline{H}} \underbrace{\begin{bmatrix} u_I[m] \\ u_Q[m] \end{bmatrix}}_{\underline{u}[m]} + \underbrace{\begin{bmatrix} w^{0r}[m] \\ w^{0i}[m] \\ w^{1r}[m] \\ w^{1i}[m] \end{bmatrix}}_{\underline{w}[m]}. \quad (10)$$

Finally, we get

$$\underline{y}[m] = \underline{H} \underline{u}[m] + \underline{w}[m] \quad (11)$$

in which $\underline{y}[m]$ denotes the compound received signal, $\underline{u}[m]$ is a vector containing both the I and Q transmitted symbols, and $\underline{w}[m]$ denotes the noise vector, \underline{H} is the compound channel matrix. The vectors $\underline{y}[m]$ and $\underline{w}[m]$ contain $4B$ symbols, \underline{H} is a matrix of size $4B \times 2B$, and $\underline{u}[m]$ is a vector of $2B$ symbols. Notice that all these vectors and matrices are real valued. Interestingly, the NFS case can be obtained from the FS by the two following adaptations.

- (i) First, one has to change the analog anti-aliasing filter at the receiver. In fact, the cut-off frequency of the NFS filter is $0.5/T$ while it is $1/T$ for the FS filter.
- (ii) Second, one keeps only the polyphase component with superscript index "0" in (10).

TABLE 3: Equalizer computation.

Task	Operation	NOPS	
		FS	NFS
Computation of $\text{diag}(\underline{\Lambda}_X^{\rho c})$	FFT	8	4
Computation of $[\underline{\Psi}^H \underline{\Psi}]^{-1} \underline{\Psi}^H$	+ and \times	8B	4B

TABLE 4: Equalization.

Task	Operation	NOPS	
		FS	NFS
Frequency components of $\underline{y}^{\rho c}[m]$	FFT	4	2
Equalization	+ and \times	14B	6B
Equalized symbols in time domain	IFFT	2	2

5. CONTINUOUS PHASE MODULATION

5.1. Transmitted signal

CPM covers a large class of modulation schemes with a constant amplitude, defined by

$$s(t, \underline{a}) = \sqrt{\frac{2E_S}{T}} e^{j\phi(t, \underline{a})}, \quad (19)$$

where $s(t, \underline{a})$ is the sent complex baseband signal, E_S the energy per symbol, T the symbol duration, and $\underline{a} = [a[0], a[1], \dots, a[N-1]]$ is a vector of length N containing the sequence of M -ary data symbols $a[n] = \pm 1, \pm 3, \dots, \pm(M-1)$. The transmitted information is contained in the phase

$$\phi(t, \underline{a}) = 2\pi h \sum_{n=0}^{N-1} a[n] \cdot q(t - nT), \quad (20)$$

where h is the modulation index and

$$q(t) = \int_{-\infty}^t g(\tau) d\tau. \quad (21)$$

Normally the function $g(t)$ is a smooth pulse shape over a finite time interval $0 \leq t \leq LT$ and zero outside. Thus L is the length of the pulse per unit T . The function $g(t)$ is normalized such that $\int_{-\infty}^{\infty} g(t) dt = 1/2$. This means that for schemes with positive pulses of finite length, the maximum phase change over any symbol interval is $(M-1)h\pi$.

As shown in [24], the BER can be halved by precoding the information sequence before passing it through the CPM modulator. If $\underline{d} = [d[1], d[2], \dots, d[N-1]]$ is a vector containing the uncoded input bipolar symbol stream, the output of the precoder \underline{a} (assuming $M=2$) can be written as

$$a[n] = d[n] \cdot d[n-1], \quad (22)$$

where $d[-1] = 1$.

A conceptual general transmitter structure based on (19) and (22) is shown in Figure 8.

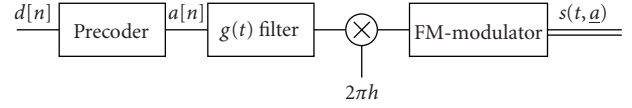


FIGURE 8: Conceptual modulator for CPM.

5.2. GMSK for low-cost, low-power 60 GHz transmitters

GMSK has been adopted as the modulation scheme for the European GSM system and for Bluetooth due to its spectral efficiency and constant-envelope property [25]. These two characteristics result in superior performance in the presence of adjacent channel interference and nonlinear amplifiers [24], making it a very attractive scheme for 60 GHz applications too. GMSK is obtained by choosing a Gaussian frequency pulse

$$g(t) = Q\left(\frac{2\pi B_T(t - T/2)}{\sqrt{\ln 2}}\right) - Q\left(\frac{2\pi B_T(t + T/2)}{\sqrt{\ln 2}}\right), \quad (23)$$

where $Q(x)$ is the well-known *error function* and B_T is the *bandwidth parameter*, which represents the -3 dB bandwidth of the Gaussian pulse. We will focus on a GMSK scheme with *time-bandwidth product* $B_T T = 0.3$, which enables us to truncate the Gaussian pulse to $L=3$ without significantly influencing the spectral properties [26]. A modulation index $h = 1/2$ is chosen as this enables the use of simple MSK-type receivers [27]. The number of symbol levels is chosen as $M=2$.

5.3. Linear representation by Laurent

Laurent [7] showed that a binary partial-response CPM signal can be represented as a linear combination of 2^{L-1} amplitude modulated pulses $C_k(t)$ (with $t = NT + \tau$, $0 \leq \tau < T$):

$$s(t, \underline{a}) = \sum_{n=0}^{N-1} \sum_{k=0}^{2^{L-1}-1} e^{j\pi h \alpha_k[n]} C_k(t - nT), \quad (24)$$

where

$$C_k(t - nT) = S(t) \cdot \prod_{n=1}^{L-1} S(t + (n + L\beta_{n,k})T), \quad (25)$$

$$\alpha_k[n] = \sum_{m=0}^n a[m] - \sum_{m=1}^{L-1} a[n-m] \beta_{n,k},$$

and $\beta_{n,k} = 0, 1$ are the coefficients of the binary representation of the index k such that

$$k = \beta_{0,k} + 2\beta_{1,k} + \dots + 2^{L-2}\beta_{L-2,k}. \quad (26)$$

The function $S(t)$ is given by

$$S(t) = \begin{cases} \frac{\sin(2\pi h q(t))}{\sin \pi h}, & 0 \leq t < LT, \\ \frac{\sin(\pi h - 2\pi h q(t - LT))}{\sin \pi h}, & LT \leq t < 2LT, \\ 0, & \text{otherwise.} \end{cases} \quad (27)$$

5.4. Receiver design

In [27], it is shown that an optimal CPM receiver can be built based on the Laurent linear representation and a Viterbi detector. Without going into details, we mention that sufficient statistics for the decision can be obtained by sampling at times nT the outputs of 2^{L-1} matched filters $C_k(-t)$; $k = 0, 1, \dots, 2^{L-1} - 1$ simultaneously fed by the complex input $r(t)$.

As we aim at bit rates higher than 1 Gbps using low-power receivers, the complexity of this type of receivers is not acceptable. Fortunately, the Laurent approximation allows us to construct linear near-optimum MSK-type receivers. In (24), the pulse described by the component function $C_0(t)$ is the most important among all other components $C_k(t)$. Its duration is the longest ($2T$ more than any other component), and it conveys the most significant part of the energy of the signal. Kaleb [27] mentions the case of GMSK with $L = 4$, where more than 99% of the energy is contained in the main pulse $C_0(t)$. It is therefore a reasonable attempt to represent CPM using not all components, or even only one component. We study a linear receiver taking into account only the first Laurent pulse $C_0(t)$. According to (24), the sent signal $s(t)$ can thus be written as

$$s(t) = \sum_{n=0}^{N-1} e^{j\pi h\alpha_0[n]} C_0(t - nT) + \epsilon(t), \quad (28)$$

where $\epsilon(t)$ is a negligible term generated by the pulses $C_k(t)$; $k = 1, \dots, 2^{L-1} - 1$. The received signal $r(t)$ can be written as

$$r(t) = s(t) \star h(t) + n(t), \quad (29)$$

where $h(t)$ is the linear multipath channel and $n(t)$ is the complex-valued AWGN. The equalization of the multipath channel is done with a simple zero-forcing filter $f_{ZF}(t)$ assuming perfect channel knowledge. The output of the ZF filter can thus be written as

$$\hat{s}(t) = s(t) + n(t) \star f_{ZF}(t). \quad (30)$$

Substituting (28) in (30), we get

$$\hat{s}(t) = \sum_{n=0}^{N-1} e^{j\pi h\alpha_0[n]} C_0(t - nT) + \epsilon(t) + n(t) \star f_{ZF}(t). \quad (31)$$

The output $y(t)$ of the filter matched to $C_0(t)$ can now be written as

$$y(t) = \int_{-\infty}^{\infty} \hat{s}(s) \cdot C_0(s - t) ds, \quad (32)$$

and this signal sampled at $t = nT$ becomes

$$y[n] \stackrel{\text{def}}{=} y(t = nT) = \int_{-\infty}^{\infty} \hat{s}(s) \cdot C_0(s - nT) ds. \quad (33)$$

Substituting (31) in (33), we get

$$y[n] = \sum_{m=0}^{N-1} e^{j\pi h\alpha_0[m]} \int_{-\infty}^{\infty} C_0(s - mT) \cdot C_0(s - nT) ds + \xi[n], \quad (34)$$

TABLE 5: System parameters OQPSK.

Filter bandwidth	BW = 1 GHz
Sample period	$T = 1$ ns
Number of bits per symbol	2
Number of symbols per block	256
Cyclic prefix length	64
Roll-off transmit filter	0.2

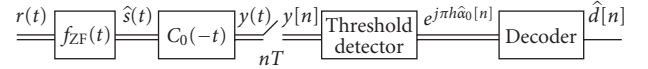


FIGURE 9: Linear GMSK receiver using the Laurent approximation.

where

$$\xi[n] = \int_{-\infty}^{\infty} [\epsilon(s) + n(s) \star f_{ZF}(s)] \cdot C_0(s - nT) ds. \quad (35)$$

The linear receiver presented in [27] includes a Wiener estimator, as $C_0(t)$ extends beyond $t = T$ and thus causes intersymbol interference (ISI). When $h = 0.5$ though, $e^{j\pi h\alpha_0[m]} = j^{\alpha_0[m]}$ is alternatively purely real and purely imaginary, so the ISI in adjacent intervals is orthogonal to the signal in that interval. As the power in the autocorrelation of $C_0(t)$ at $t_1 - t_2 \geq 2T$ is very small, we can further simplify our receiver by neglecting the ISI. Equation (34) is indeed approximately:

$$y[n] \approx e^{j\pi h\alpha_0[n]} + \xi'[n]. \quad (36)$$

Thus we get an estimate of the complex coefficient $e^{j\pi h\hat{\alpha}_0[n]}$ of the first Laurent pulse $C_0(t)$ after the threshold detector. Taking into account the precoder (22), the Viterbi detection can now be replaced by a simple decoder [24]

$$\hat{d}[n] = j^{-n} \cdot e^{j\pi h\hat{\alpha}_0[n]}. \quad (37)$$

This linear receiver is shown in Figure 9.

6. NUMERICAL RESULTS

6.1. Simulation setup

6.1.1. Offset-QPSK with FDE

The system parameters of OQPSK are summarized in Table 5. The root-raised cosine transmit filter has a bandwidth of 1 GHz. The sample period after the insertion of the CP is 1 nanosecond. An OQPSK symbol carries the information of 2 bits. The CP length has been set to 64 samples, which is larger than the maximum channel time dispersion (around 40 nanoseconds). The transmitter filter has a roll-off factor of 0.2. This configuration enables a bit rate equal to 1.6 Gbps.

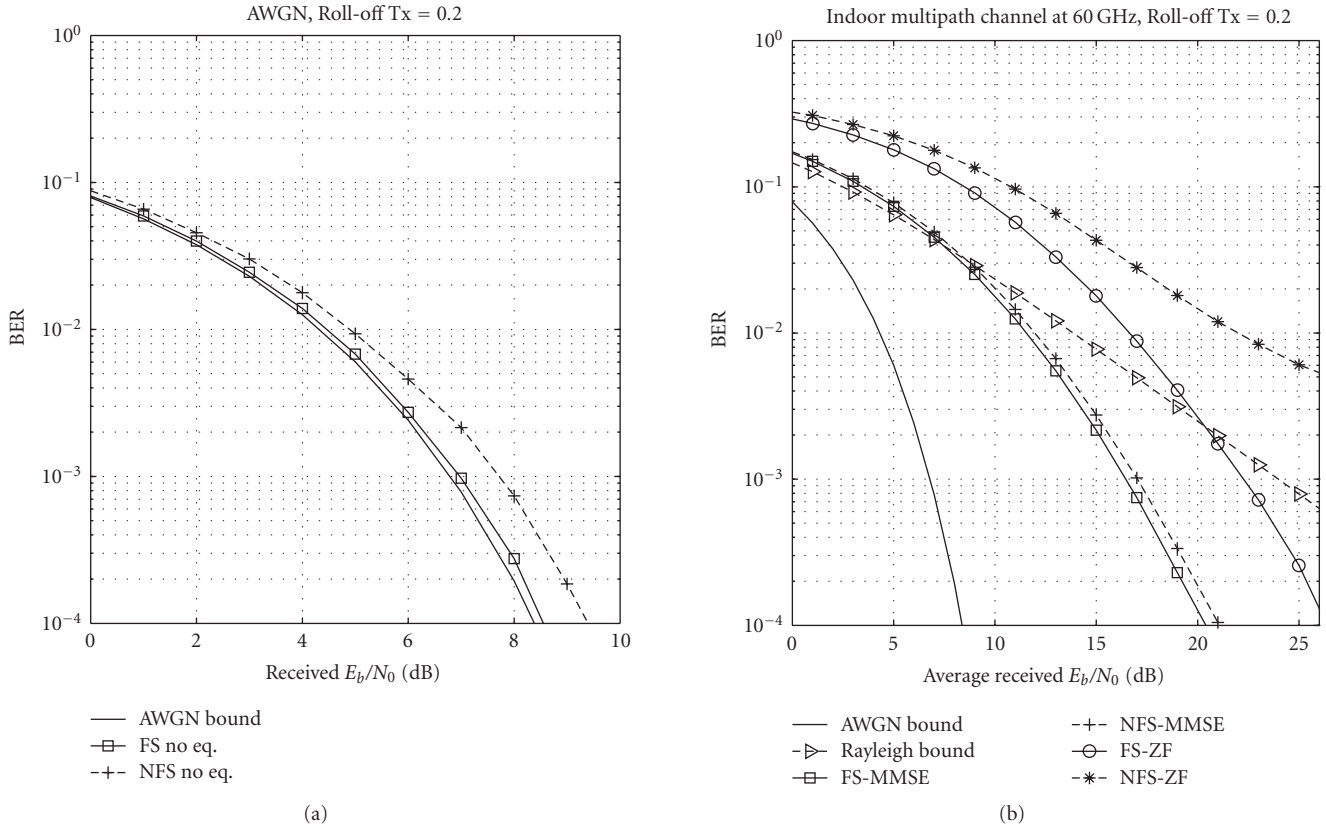


FIGURE 10: Uncoded BER performance of OQPSK with FDE for different receivers.

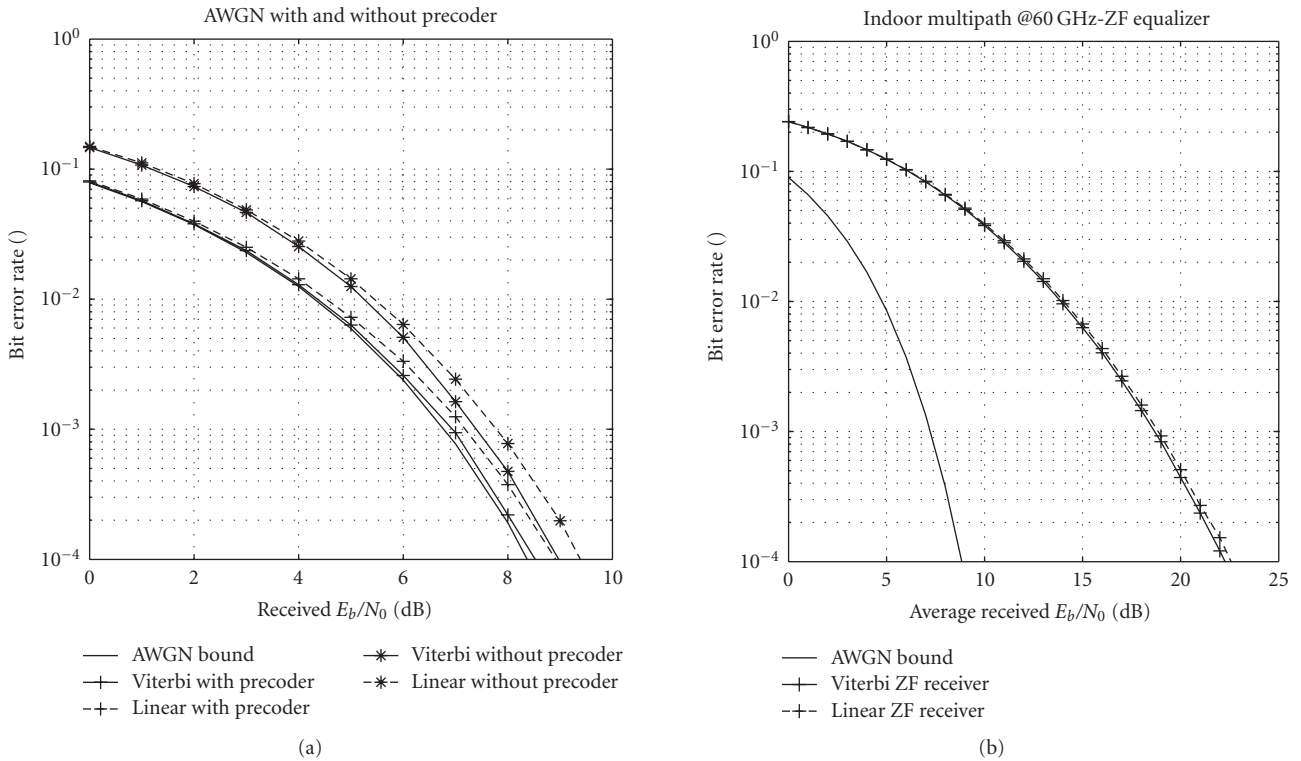


FIGURE 11: BER performance of CPM with ZF equalizer for different receivers.

TABLE 6: System parameters CPM.

Symbol duration	$T = 1 \text{ ns}$
Pulse shape	Gaussian
Pulse duration	$3.T$
Modulation index	$h = 1/2$
Number of symbol levels	$M = 2$
Channel coding	Uncoded

6.1.2. CPM

The system parameters for CPM are summarized in Table 6. With these parameters, a bit rate of 1 Gbps is reached.

6.2. BER performance with ideal FE

6.2.1. OQPSK with FDE

We have compared the uncoded BER performance of the ZF and MMSE equalizers for both FS and NFS receivers. Simulation results are represented in Figure 10. In Figure 10(a), we show the BER performance in an AWGN channel. The simulation in an indoor frequency fading channel at 60 GHz is shown in Figure 10(b). One notices that the performance of FS receiver (solid line) is always better than that of NFS receivers (dashed line). In fact, in the NFS case, the frequency components of the transmitted signal above $0.5/T$ are filtered out by the anti-aliasing receiver filter, thus the received signal does not contain all the information from the transmitted signal. On the contrary, in the FS case, the anti-aliasing filter has a larger bandwidth than the transmitted signal, thus all the information from the transmitted signal is available in the received sampled signal.

Simulations show that the performance gain of FS over NFS receiver at a BER of 10^{-3} is about 0.5 dB with an MMSE equalizer. This gain is much higher with a ZF equalizer. In fact, the ZF equalizer is known to be very sensitive to nulls in the frequency domain. However, in the FS case, the performance is improved thanks to the diversity provided by the polyphase components. Thus, the probability that both the polyphase channels fall in a deep fade at the same time is reduced compared to the probability that only one of the channels fades.

ZF equalizers perform at least 5 dB worse at a BER of 10^{-3} relative to MMSE equalizers. However, even though the FS receivers yield better performance, they require an ADC with a sampling clock twice as fast as that needed by the NFS receivers. Moreover, the digital receiver is twice as complex as that of NFS receivers. Therefore, by trading-off complexity, cost and BER performance, the combination of NFS with MMSE is the most appropriate for low-cost low-consumption devices. We will thus use the NFS-MMSE receiver to assess the impact of FE nonidealities on the BER performance of OQPSK with FDE transceiver.

Notice that by comparing with the Rayleigh bound (solid triangle Figure 10(b)), it can also be verified that the SC modulation scheme with FDE inherently provides frequency diversity [5].

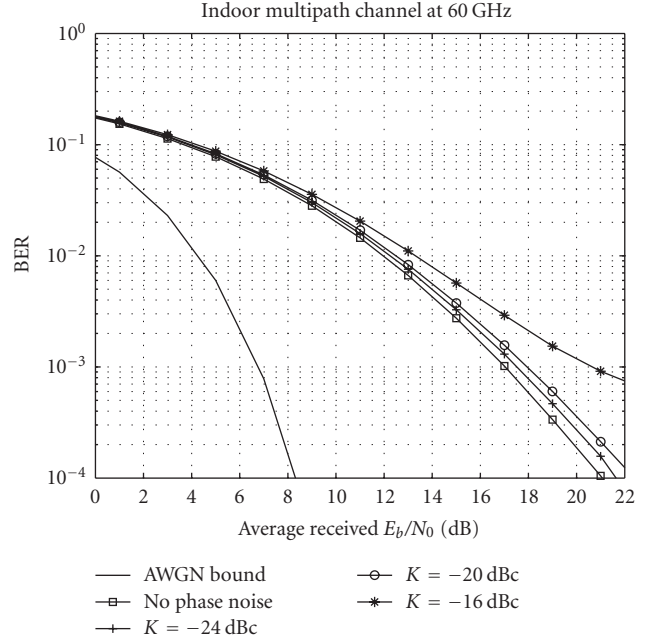


FIGURE 12: Impact of phase noise on BER performance of OQPSK.

6.2.2. CPM

Figure 11 shows the comparison of different GMSK receivers in AWGN and in a multipath 60 GHz scenario. In Figure 11(a), we compare the Viterbi and the linear receivers in AWGN, and show the theoretical BER bound as a reference. An obvious conclusion is that using a precoder delivers a gain of 0.5–1 dB with only a minor complexity increase. Next, we observe that using the linear receiver results in a loss of at most 0.5 dB compared to the Viterbi receiver. The complexity savings are huge though, so a linear receiver seems to be the right choice for 60 GHz applications.

In Figure 11(b), the BER performance in a 60 GHz indoor multipath environment is shown. The Viterbi and linear receiver, both with precoder and ZF equalizers, are compared. Here, the difference between both receivers almost completely vanishes. The linear receiver with ZF equalizer will be used to assess the impact of FE nonidealities on CPM.

6.3. Impact of phase noise on BER performance

6.3.1. OQPSK with FDE

We have simulated the BER performance of the NFS-MMSE receiver taking into account the phase noise. The simulations have been carried out in an indoor multipath environment at 60 GHz. Simulation results are represented in Figure 12. For a BER of 10^{-3} , the performance degradation is about 4 dB for an integrated PSD of -16 dBc . However, the performance can be improved by 3 dB when the integrated PSD is -20 dBc . That is at the price of more stringent requirements on VCO and synthesizer design.

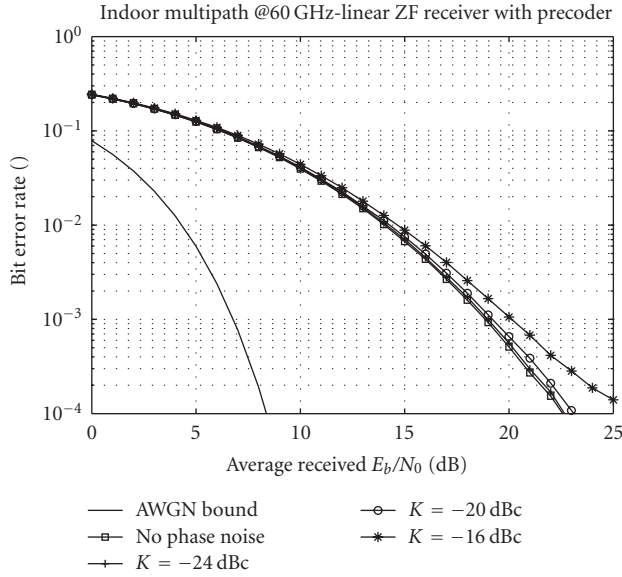


FIGURE 13: Impact of phase noise on the BER performance of CPM.

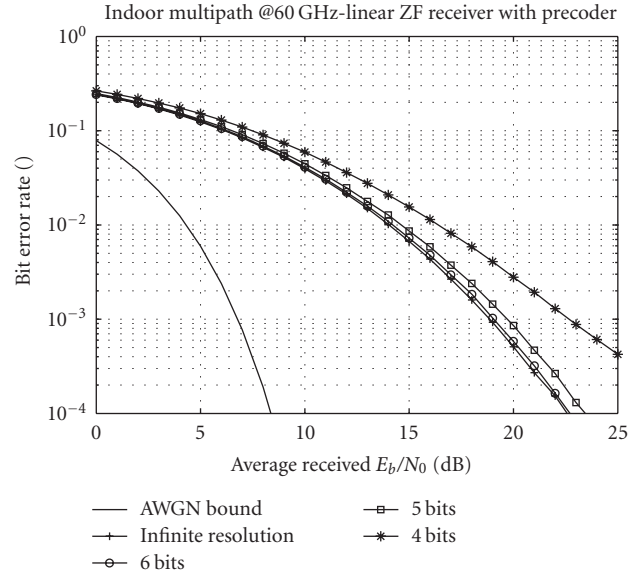


FIGURE 15: Impact of quantization on the BER performance of CPM.

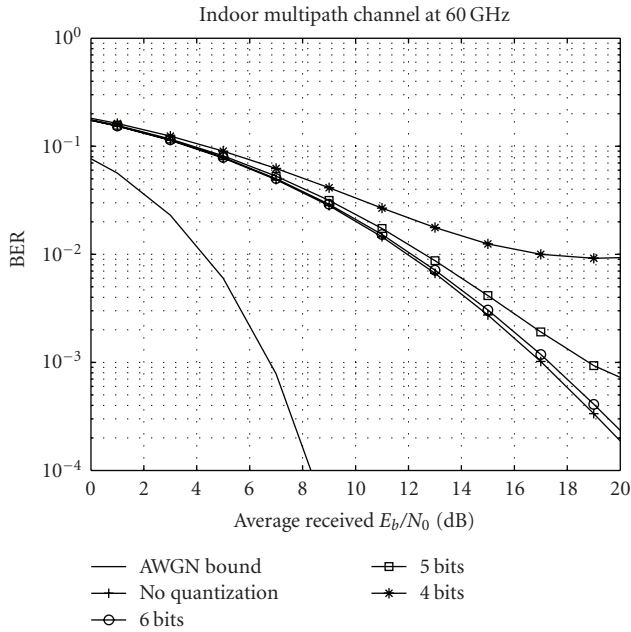


FIGURE 14: Impact of quantization on the BER performance of OQPSK.

6.3.2. CPM

Simulation results with PN in an indoor multipath environment at 60 GHz are presented in Figure 13. The performance degradation is negligible for an integrated PN power of -24 dBc. For a BER of 10^{-3} , we lose only slightly more than 1 dB with an integrated PN power of -16 dBc. CPM seems to be less sensitive to phase noise, or at least the effect of the multipath propagation, equalized with a ZF filter, drowns it out.

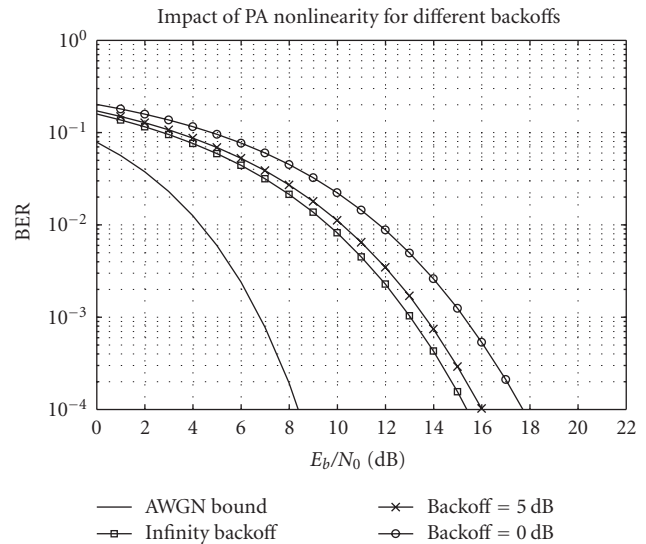


FIGURE 16: Impact of PA nonlinearity on BER performance of OQPSK.

6.4. Impact of ADC nonidealities on BER performance

6.4.1. OQPSK with FDE

The impact of the resolution of the ADC in terms of bits is analyzed. Simulation results are represented in Figure 14. For a BER of 10^{-3} , the performance degradations are about 2 dB with an ADC of 5 bits. With one additional bit, the performance degradation becomes negligible. However, by increasing the number of resolution bits, the power consumption of the ADC will grow up.

6.4.2. CPM

Figure 15 shows the effect of quantization due to the ADC for CPM modulation. For a BER of 10^{-3} , the performance degradation is about 1 dB for an ADC with 5 bits. With an additional bit, performance degradation becomes negligible. CPM is less affected by a low resolution ADC than OQPSK.

6.5. Impact of PA nonlinearity on BER performance

Figure 16 shows the impact of inband distortion due to PA nonlinearity on the performance of OQPSK for different values of backoff. With a backoff of 5 dB, the performance degradation is only 0.5 dB for a BER of 10^{-3} . However, the power efficiency of the system is reduced. If the PA operates in the saturated region (0.5 dB backoff) to improve the power efficiency, then the performance degradation becomes 2 dB. Note that CPM is not affected by the nonlinearity in the PA thanks to its completely constant envelope.

7. CONCLUSION

In this paper, we compared the OQPSK and CPM modulators for communications at 60 GHz with a nonideal FE. For the OQPSK modulator, the NFS-MMSE receiver offers the best trade off between BER performance and complexity. Concerning the CPM modulator, the linear receiver offers a huge complexity reduction with only a minor performance degradation. The spectral efficiency of the OQPSK is higher than that of CPM. However, CPM is slightly less sensible to phase noise than OQPSK. The same conclusion applies to ADC resolution when the number of bits is less than 6. This is because the CPM signal after the multipath channel has a smaller envelope fluctuation than the OQPSK signal. For the same reason, CPM allows more power efficient operation of the PA while OQPSK needs a few dBs of backoff to avoid distortion.

REFERENCES

- [1] <http://www.ieee802.org/15/pub/TG3c.html>.
- [2] B. M. Motlagh, S. E. Gunnarsson, M. Ferndahl, and H. Zirath, "Fully integrated 60-GHz single-ended resistive mixer in 90-nm CMOS technology," *IEEE Microwave and Wireless Components Letters*, vol. 16, no. 1, pp. 25–27, 2006.
- [3] P. F. M. Smulders and A. G. Wagemans, "Wide-band measurements of MM-wave indoor radio channels," in *Proceedings of the 3rd IEEE International Symposium on Personal, Indoor and Mobile Radio Communications (PIMRC '92)*, pp. 329–333, Boston, Mass, USA, October 1992.
- [4] H. Yang, P. F. M. Smulders, and M. H. A. J. Herben, "Frequency selectivity of 60-GHz LOS and NLOS indoor radio channels," in *Proceedings of the 63rd IEEE Vehicular Technology Conference (VTC '06)*, vol. 6, pp. 2727–2731, Melbourne, Australia, May 2006.
- [5] D. Falconer, S. L. Ariyavisitakul, A. Benyamin-Seeyar, and B. Eidson, "Frequency domain equalization for single-carrier broadband wireless systems," *IEEE Communications Magazine*, vol. 40, no. 4, pp. 58–66, 2002.
- [6] C.-E. Sundberg, "Continuous phase modulation," *IEEE Communications Magazine*, vol. 24, no. 4, pp. 25–38, 1986.
- [7] P. A. Laurent, "Exact and approximate construction of digital phase modulations by superposition of amplitude modulated pulses (AMP)," *IEEE Transactions on Communications*, vol. 34, no. 2, pp. 150–160, 1986.
- [8] B. E. Rimoldi, "Decomposition approach to CPM," *IEEE Transactions on Information Theory*, vol. 34, no. 2, pp. 260–270, 1988.
- [9] P. Smulders, "Exploiting the 60 GHz band for local wireless multimedia access: prospects and future directions," *IEEE Communications Magazine*, vol. 40, no. 1, pp. 140–147, 2002.
- [10] C. R. Anderson and T. S. Rappaport, "In-building wideband partition loss measurements at 2.5 and 60 GHz," *IEEE Transactions on Wireless Communications*, vol. 3, no. 3, pp. 922–928, 2004.
- [11] P. F. M. Smulders and L. M. Correia, "Characterisation of propagation in 60 GHz radio channels," *Electronics and Communication Engineering Journal*, vol. 9, no. 2, pp. 73–80, 1997.
- [12] R. Davies, M. Bensebti, M. A. Beach, and J. P. McGeehan, "Wireless propagation measurements in indoor multipath environments at 1.7 GHz and 60 GHz for small cell systems," in *Proceedings of the 41st IEEE Vehicular Technology Conference (VTC '91)*, pp. 589–593, St. Louis, Mo, USA, May 1991.
- [13] P. F. M. Smulders and G. J. A. P. Vervuurt, "Influence of antenna radiation patterns on MM-wave indoor radio channels," in *Proceedings of the 2nd International Conference on Universal Personal Communications*, vol. 2, pp. 631–635, Ottawa, Ont, Canada, October 1993.
- [14] A. A. M. Saleh and R. A. Valenzuela, "Statistical model for indoor multipath propagation," *IEEE Journal on Selected Areas in Communications*, vol. 5, no. 2, pp. 128–137, 1987.
- [15] J.-H. Park, Y. Kim, Y.-S. Hur, K. Lim, and K.-H. Kim, "Analysis of 60 GHz band indoor wireless channels with channel configurations," in *Proceedings of the 9th IEEE International Symposium on Personal, Indoor and Mobile Radio Communications (PIMRC '98)*, vol. 2, pp. 617–620, Boston, Mass, USA, September 1998.
- [16] A. Bourdoux and J. Liu, "Transceiver nonidealities in multi-antenna systems," in *Smart Antennas—State of the Art*, chapter 32, pp. 651–682, Hindawi, New York, NY, USA, 2005.
- [17] D. Dardari, "Exact analysis of joint clipping and quantization effects in high speed WLAN receivers," in *IEEE International Conference on Communications (ICC '03)*, vol. 5, pp. 3487–3492, Anchorage, Alaska, USA, May 2003.
- [18] M. Engels, *Wireless OFDM Systems: How to Make Them Work?*, Kluwer Academic, Norwell, Mass, USA, 2002.
- [19] C. Cao and K. O. Kenneth, "Millimeter-wave voltage-controlled oscillators in 0.13- μm CMOS technology," *IEEE Journal of Solid-State Circuits*, vol. 41, no. 6, pp. 1297–1304, 2006.
- [20] L. W. Couch II, *Digital and Analog Communication Systems*, Prentice Hall PTR, Upper Saddle River, NJ, USA, 6th edition, 2001.
- [21] Z. Wang and G. B. Giannakis, "Wireless multicarrier communications," *IEEE Signal Processing Magazine*, vol. 17, no. 3, pp. 29–48, 2000.
- [22] F. Horlin and L. Vandendorpe, "A comparison between chip fractional and non-fractional sampling for a direct sequence CDMA receiver," *IEEE Transactions on Signal Processing*, vol. 50, no. 7, pp. 1713–1723, 2002.
- [23] A. Klein, G. K. Kaleb, and P. W. Baier, "Zero forcing and minimum mean-square-error equalization for multiuser detection in code-division multiple-access channels," *IEEE Transactions on Vehicular Technology*, vol. 45, no. 2, pp. 276–287, 1996.

- [24] N. Al-Dhahir and G. Saulnier, "A high-performance reduced-complexity GMSK demodulator," *IEEE Transactions on Communications*, vol. 46, no. 11, pp. 1409–1412, 1998.
- [25] K. Murota and K. Hirade, "GMSK modulation for digital mobile radio telephony," *IEEE Transactions on Communications Systems*, vol. 29, no. 7, pp. 1044–1050, 1981.
- [26] J. G. Proakis, *Digital Communications*, McGraw-Hill, Boston, Mass, USA, 4th edition, 2001.
- [27] G. K. Kaleh, "Simple coherent receivers for partial response continuous phase modulation," *IEEE Journal on Selected Areas in Communications*, vol. 7, no. 9, pp. 1427–1436, 1989.

Research Article

Direct Conversion EHM Transceivers Design for Millimeter-Wave Wireless Applications

Abbas Mohammadi,¹ Farnaz Shayegh,² Abdolali Abdipour,¹ and Rashid Mirzavand¹

¹ Microwave and Wireless Communication Research Laboratory, Electrical Engineering Department, Amirkabir University of Technology (Polytechnic), Tehran 1587-4413, Iran

² Electrical and Computer Engineering Department, Concordia University, Montreal, QC, Canada H4G2W1

Received 29 March 2006; Revised 14 November 2006; Accepted 15 November 2006

Recommended by Kiyoshi Hamaguchi

A direct conversion modulator-demodulator with even harmonic mixers for fixed wireless applications is presented. The circuits consist of even harmonic mixers (EHMs) realized with antiparallel diode pairs (APDPs). A communication link is set up to examine the overall performance of proposed modulator-demodulator. The transmission of 16-QAM signal with 110 Mbps data rate over fixed wireless link has been examined. We also evaluate the different levels of I/Q imbalances and DC offsets and use signal space concepts to analyze the bit error rate (BER) of the proposed transceiver using M -ary QAM schemes. The results show that this structure can be efficiently used for fixed wireless applications in Ka band.

Copyright © 2007 Abbas Mohammadi et al. This is an open access article distributed under the Creative Commons Attribution License, which permits unrestricted use, distribution, and reproduction in any medium, provided the original work is properly cited.

1. INTRODUCTION

Local multipoint distribution system (LMDS) is a broadband wireless point-to-multipoint communication system operating above 20 GHz and provide high-data-rate voice, TV, and internet services. It is desirable to increase the spectral efficiency or the transmission capacity of LMDS services by using sophisticated amplitude and phase modulation techniques (QPSK and QAM). The cost reduction in LMDS transceiver design is a key issue to increase the deployment of this system. Among various realization techniques, the direct conversion implementation reduces the size and cost of LMDS transceiver. A direct conversion modulator-demodulator using even harmonic mixers (EHMs) is designed at 28 GHz for LMDS applications. The EHM is based on antiparallel diode pair (APDP). The APDP has a balanced structure that suppresses the fundamental mixing products ($m f_{LO} \pm n f_{IF}$ where $m + n = \text{even}$). These products flow only within the APDP loop [1]. The EHM with APDP has some advantages that make it very attractive for millimeter-wave transceivers. These advantages are: (1) it can operate with halved LO frequency; (2) in direct conversion transmitter, it can suppress the virtual LO leakage ($2 f_{LO}$) that locates nearby a desired RF signal; (3) it suppresses DC offset in direct conversion receivers.

The paper is organized as follows: the even harmonic mixer structure and three methods to improve its behavior are introduced. Then, a direct conversion modulator is designed using even harmonic mixers. The modulator structure is reciprocal and can also be used as a direct conversion demodulator. Next, we consider the effects of I/Q imbalances and DC offsets on the bit-error-rate performance of the demodulator for M -ary QAM schemes. Finally, a communications link using direct 16-QAM modulator-demodulator with 110 Mbps data rate is successfully demonstrated.

2. EVEN HARMONIC MIXER

Figure 1(a) shows a circuit configuration of the even harmonic mixer (EHM). It includes open- and short-circuited stubs at each port of the APDP. Both of them have a quarter-wave length at LO frequency. Using these stubs, the BPF and the LPE, the leakage of each port at other ports is suppressed [2]. The BPF is designed to cover the RF band of 27.5-28.5 GHz. It is a third-order chebycheve filter with center frequency of 28 GHz. The filter insertion loss (S12) and also the filter S11 curves in dB are shown in Figure 2. As we can see from the filter insertion loss, the filter center frequency is 28 GHz and its 3-dB bandwidth is 1 GHz from 27.5 GHz to 28.5 GHz. In 28 GHz, the amount of S11 and S22 in dB is

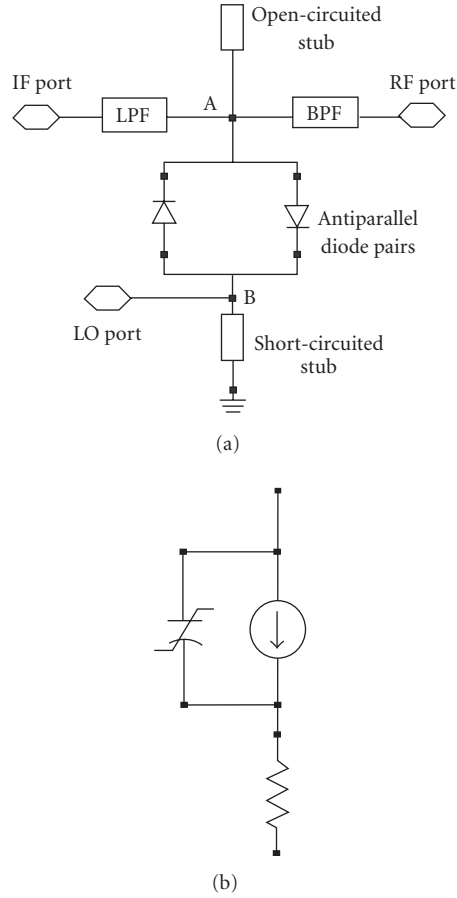


FIGURE 1: (a) Circuit configuration of the even harmonic mixer, (b) Schottky diode nonlinear model.

-28.674, so there is a good matching in filter input and output. The GaAs Schottky barrier APDP (agilent HSCH-9551) is used to realize the mixer. Table 1 shows its parameters.

This mixer is used to mix the baseband signal (at 100 MHz) with the second harmonic of the LO signal (at 13.95 GHz) to provide the RF signal at 28 GHz. Figure 3 shows the mixer conversion gain versus LO power [3]. This results are obtained from the harmonic-balance simulation. Figure 1(b) shows the Schottky diode nonlinear model. In continue, we introduce three ways to improve the mixer behavior and reduce its conversion loss.

2.1. Matching networks

In this section, matching networks in both sides of the APDP are included in an effort to reduce the mixer conversion loss and the LO power required for optimal mixer conversion loss [4]. LO matching network consists of a series delay line followed by a shunt short-circuited stub. RF matching network consists of a series delay line followed by a shunt open-circuited stub. These matching networks are designed to match the APDP impedance at the LO and RF ports to 50 ohm. The length of these stubs is iteratively tuned to

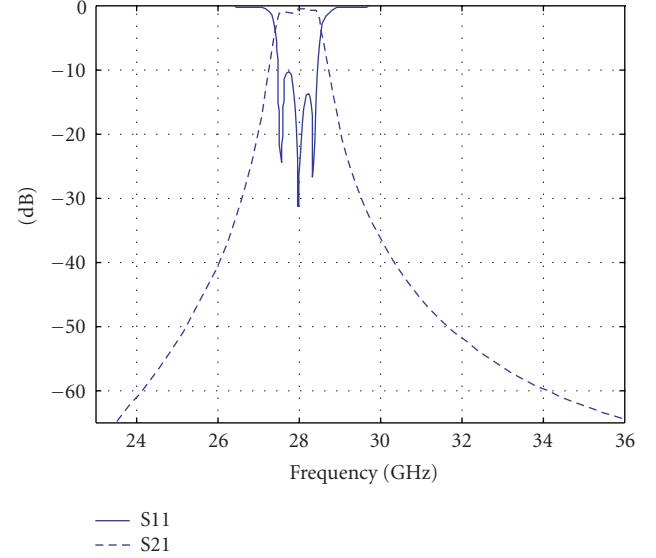


FIGURE 2: Filters S11 and S12 (dB).

TABLE 1: Diode parameters.

Junction capacitance (C_{j0})	0.04 pF
Series resistance (R_s)	6 Ω
Saturation current (I_s)	1.6E-13A
Ideality factor (N)	1.2

provide good conversion loss at a relatively low LO drive level. Figure 4 shows the mixer conversion gain versus LO power with and without the matching networks. As we can see from this figure, matching networks result in decrease of LO power required for optimal mixer conversion loss and a slight improvement in mixer conversion loss.

2.2. Parallel diodes

As we know, series resistance (R_s) of Schottky diodes is a major factor in diode mixer conversion loss. If two parallel Schottky diodes are substituted for each diode in APDP, effective R_s of the structure will be divided by an approximate factor of two and the conversion loss will be decreased [5]. Also use of three diodes instead of each diode causes more decrease in mixer conversion loss. For each of the above cases, matching networks should be designed again.

Figure 5 shows the mixer conversion loss with one, two, and three diodes.

2.3. Self-biased APDP

Another way to improve the conversion loss of our mixer is to use self-biased APDP [6]. In this case, RC networks in both sides of each diode are designed to flatten the conversion loss of the even harmonic mixer. The values of RC networks are $R = 150$ ohm, $C = 50$ pf. Figure 6 shows conversion gain versus LO power with self-biased APDP and conventional

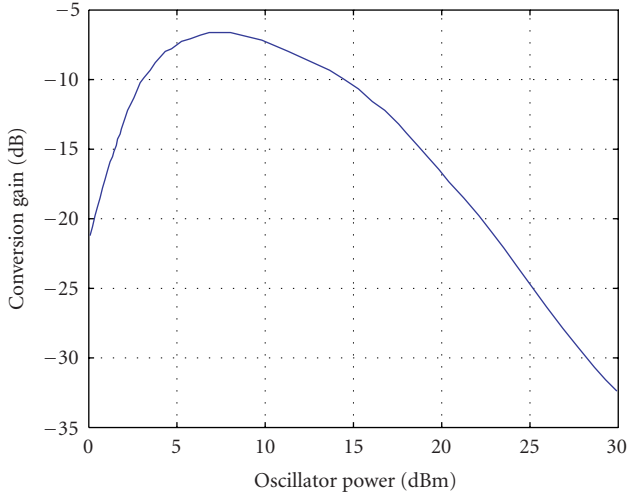


FIGURE 3: Conversion gain of the EHM.

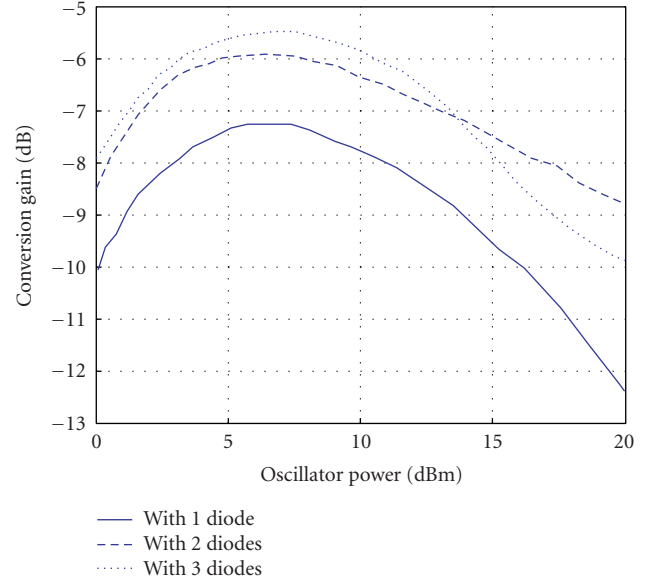


FIGURE 5: Mixer conversion gain.

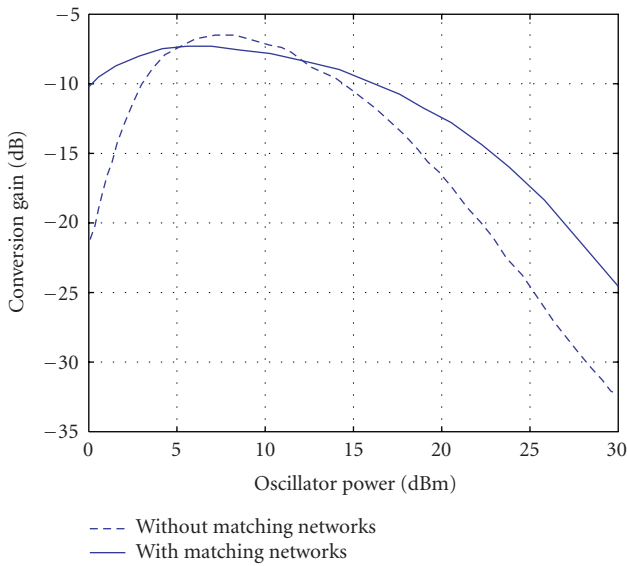


FIGURE 4: Mixer conversion gain.

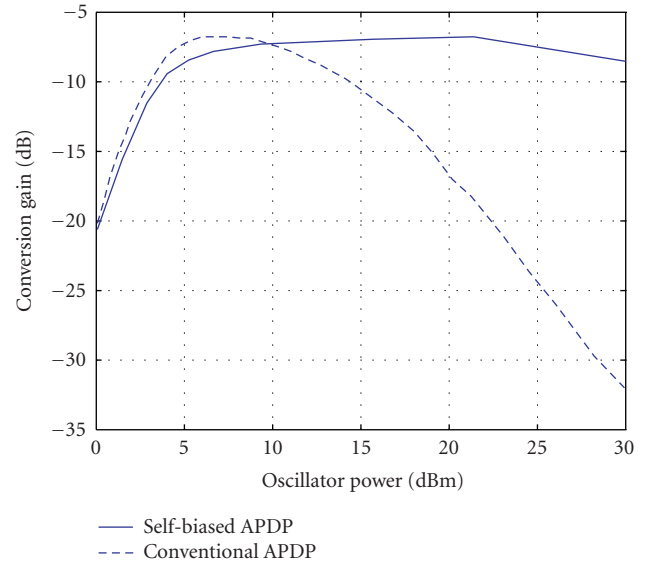


FIGURE 6: Conversion gain of the EHM using self-biased APDP and conventional APDP.

APDP. The conversion loss of EHM using self-biased APDP is almost constant from 10 dBm to 25 dBm of LO power.

2.3.1. Numerical results

We also write a program with Matlab software in order to calculate the conversion loss of the EHM using self-biased APDP by the harmonic-balance method. Diode parameters used for calculation are obtained from the agilent HSCH-9551 data sheet. We set the RF frequency to 28 GHz and the RF power to -75 dBm. The RF signal is mixed with second harmonic of the LO signal. Figure 7 shows calculated conver-

sion gain versus LO power. As may be seen, the calculated results agree well with the simulated results. In order to have the best mixer behavior, self-biased APDP is used and three diodes are substituted for each diode in APDP. In addition to this, matching networks are designed in both sides of the APDP. Figure 8 shows the mixer structure used in our design. In continue, we consider the third-order intermodulation results [7]. To do this, two sinusoidal signals at the same amplitude and little frequency difference (28.007 GHz, 27.93 GHz) are inserted at the RF port and input and output IP3 (third-order intercept point) are calculated. Figure 9 shows the results.

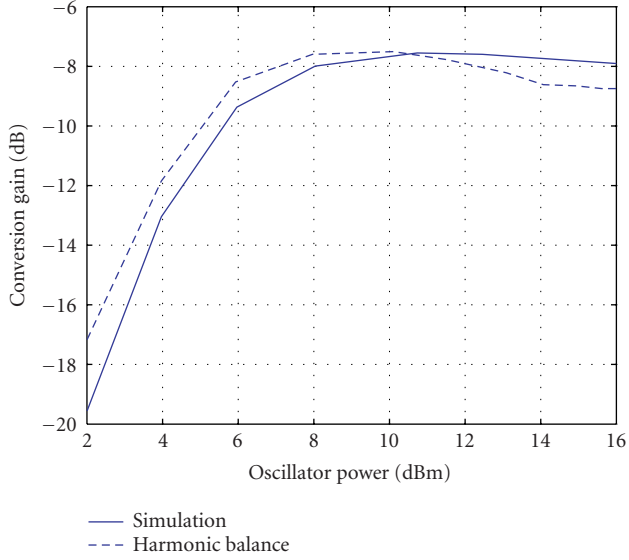


FIGURE 7: Conversion gain of the EHM using self-biased APDP calculated by the harmonic balance method and compared with simulated results.

3. MODULATOR STRUCTURE

The proposed I-Q modulator consists of two even harmonic mixers as shown in Figure 10. The LO signal is split by a Wilkinson power divider, and a 45° delay line is connected to one of Wilkinson power divider arms to provide 90° phase difference at the second harmonic of the LO [8]. The LO carriers are mixed with baseband modulating signals (I and Q) in even harmonic mixers. Finally, both mixed signals are combined in a Wilkinson power combiner and the modulated signal is produced.

The following formulas illustrate the modulator inputs:

$$\begin{aligned} v_{LO}(t) &= \cos \omega_{LO}t, \\ v_I(t) &= \cos \omega_{IF}t, \\ v_Q(t) &= \cos (\omega_{IF}t + 90). \end{aligned} \quad (1)$$

Then, the outputs of EHMs can be obtained as follows:

$$\begin{aligned} e_1(t) &= \cos 2\omega_{LO}t \times \cos \omega_{IF}t, \\ e_2(t) &= \cos (2\omega_{LO}t - 90) \times \cos (\omega_{IF}t + 90). \end{aligned} \quad (2)$$

Finally, using Wilkinson power combiner, the modulated signal is as follows:

$$e(t) = e_1(t) + e_2(t) = \cos (2\omega_{LO} + \omega_{IF})t. \quad (3)$$

As may be seen, the lower sideband component ($2f_{LO} - f_{IF}$) is suppressed without external filters.

In order to characterize the modulator performance, we insert two sinusoidal carriers at the same low frequency ($f_{IF} = 100$ MHz), same amplitude, and quadrature phase on the I and Q inputs. Figure 11 shows the RF spectrum of the modulator operating at LO power of 10 dBm and LO frequency of 13.95 GHz. The power of virtual LO leakage

($2f_{LO} = 27.9$ GHz) is -67 dBm. So, the suppression of the virtual LO leakage of 77 dB is obtained. The lower sideband component ($2f_{LO} - f_{IF} = 27.8$ GHz) is 25 dB lower than the desired component ($f_{RF} = 2f_{LO} + f_{IF} = 28$ GHz).

Figure 12 shows the conversion gain of the whole modulator using a self-biased APDP and a conventional APDP.

4. DEMODULATOR

As mentioned above, the modulator is realized with passive components and the mixer is based on Schottky diodes that do not need DC bias circuitry. Accordingly, the whole modulator has zero DC power consumption. This modulator is totally reciprocal and can be used as a demodulator [9]. To characterize this circuit as a demodulator, a sinusoidal signal is inserted on RF port and the power at I and Q outputs is measured. Figure 12 shows conversion gain of the demodulator versus RF frequency from 26 to 30 GHz. The figure shows that the demodulator has bandwidth better than 1.5 GHz. The average conversion loss is 7.5 dB around 28 GHz for both channels.

5. BER CALCULATIONS

In this section, we consider the impacts of I/Q imbalances and DC offsets on QAM detection in the demodulator. The input signal in the RF port is a QAM signal and can be written as follows:

$$X_{RF}(t) = \sqrt{\frac{2E_{\min}}{T_s}} (a_i \cos (2\pi f_c t) + b_i \sin (2\pi f_c t)), \quad (4)$$

where

$$\{a_i, b_i\} = \begin{bmatrix} (-L+1, L-1)(-L+3, L-1) \cdots (L-1, L-1) \\ (-L+1, L-3)(-L+3, L-3) \cdots (L-1, L-3) \\ \vdots \\ (-L+1, -L+1)(-L+3, -L+1) \cdots (L-1, -L+1) \end{bmatrix}, \quad (5)$$

$i = 1, 2, \dots, L; L = \sqrt{M}.$

M is restricted to 2^P so that each symbol can be represented by P bits. We will restrict our consideration to Gray code bit mapping [10]. The Gray code mapping has the property that two P -bit symbols corresponding to adjacent symbols differ in only a single bit. As a result, an error in an adjacent symbol is accompanied by one and only one bit error. Finally, we do our calculations under AWGN channel.

5.1. BER calculations in presence of I/Q imbalances

We assume that the I and Q paths of LO signal in the demodulator are equal to

$$\begin{aligned} X_{Lo,I}(t) &= \left(1 + \frac{\varepsilon}{2}\right) \cos \left(\omega_{Lo}t + \frac{\theta}{2}\right), \\ X_{Lo,Q}(t) &= \left(1 - \frac{\varepsilon}{2}\right) \cos \left(\omega_{Lo}t - \frac{\theta}{2}\right), \end{aligned} \quad (6)$$

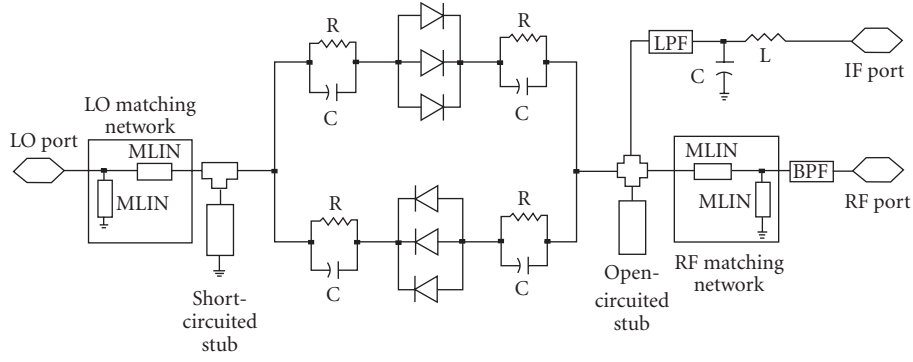


FIGURE 8: EHM structure used in our design.

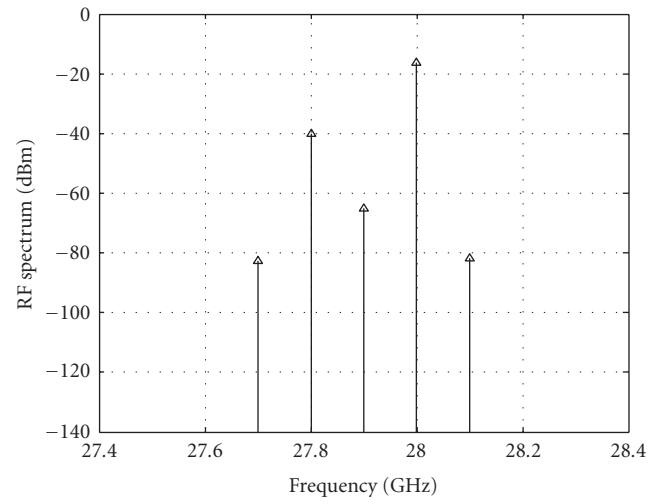
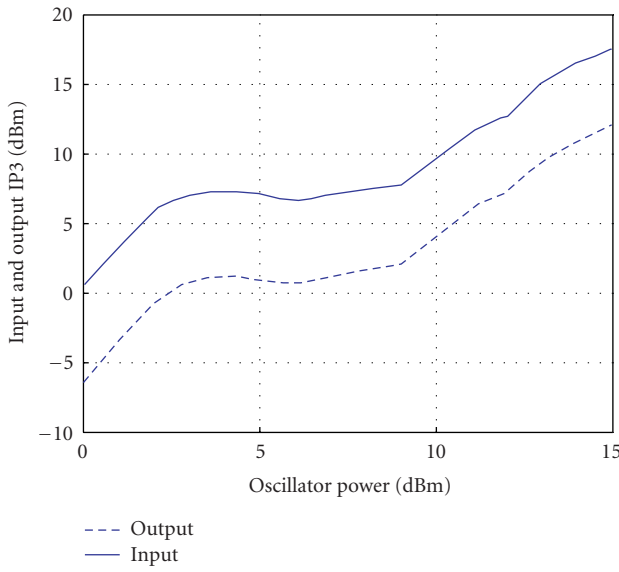


FIGURE 11: Spectrum at output of the modulator.

FIGURE 9: Input and output IP3 versus LO power for self-biased EHM.

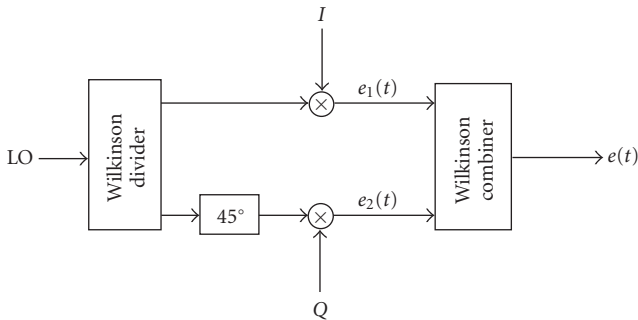


FIGURE 10: Modulator scheme.

where ε and θ represent gain and phase errors, respectively. As we know from [1], the conductance expression for an APDP can be written as follows:

$$g = 2\alpha i_s \cosh(\alpha V). \quad (7)$$

In this formula, α and i_s are the slope ($\alpha = q/kT$) and saturation current of diodes. For the usual case in which only the LO signal modulates the conductance of the diodes, we may substitute $V = X_{Lo}(t)$. So, conductances in I and Q paths may be expanded in the following series [1]:

$$\begin{aligned} g_I &= 2\alpha i_s \left[I_0 \left(\alpha \left(1 + \frac{\varepsilon}{2} \right) \right) \right. \\ &\quad \left. + 2I_2 \left(\alpha \left(1 + \frac{\varepsilon}{2} \right) \right) \cos(2\omega_{Lo}t + \theta) + \dots \right], \\ g_Q &= 2\alpha i_s \left[I_0 \left(\alpha \left(1 - \frac{\varepsilon}{2} \right) \right) \right. \\ &\quad \left. + 2I_2 \left(\alpha \left(1 - \frac{\varepsilon}{2} \right) \right) \sin(2\omega_{Lo}t - \theta) + \dots \right], \end{aligned} \quad (8)$$

where I_n are modified Bessel functions of the first kind. So, the output currents in I and Q ports after a lowpass filter are

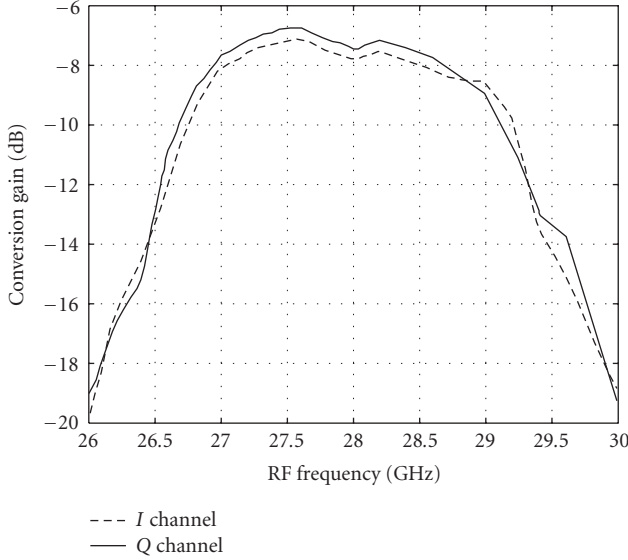


FIGURE 12: Conversion gain versus RF frequency for I and Q channels at LO power of 10 dBm.

equal to

$$\begin{aligned}\tilde{I} &= 2\alpha i_s \sqrt{\frac{2E_{\min}}{T_s}} I_2\left(\alpha\left(1 + \frac{\varepsilon}{2}\right)\right) [a_i \cos \theta - b_i \sin \theta], \\ \tilde{Q} &= 2\alpha i_s \sqrt{\frac{2E_{\min}}{T_s}} I_2\left(\alpha\left(1 - \frac{\varepsilon}{2}\right)\right) [b_i \cos \theta - a_i \sin \theta].\end{aligned}\quad (9)$$

It can be seen that in either case, the errors in the nominally 45° phase shifts and mismatches between the amplitudes of the I and Q signal corrupt the downconverted signal constellation, thereby rising the bit error rate. In continue, we calculate the BER for different levels of amplitude and phase imbalances. For this purpose, we use the signal space concepts described in [11]. We derive algorithms to do this calculations for 16, 64, and 256-QAM schemes. We also use approximate-closed-form formula in (10) to compare our results with

$$\text{BER} = \frac{4}{\log_2 M} \left(1 - \frac{1}{\sqrt{M}}\right) Q\left(\sqrt{\frac{3(Eb/N_0) \log_2 M}{(M-1)}}\right).\quad (10)$$

First, we assume amplitude imbalance. Figure 13 shows the BER of the 16-QAM signal for ε values of 0, 0.08, 0.16. It also illustrates the BER obtained from closed-form formula that is in agreement with our result for $\varepsilon = 0$. From the figure, it can be seen that as the amplitude error increases, the amount of E_b/N_0 required to have BER of 10^{-6} increases. In 16-QAM modulation, if the amplitude error in I and Q paths reaches 28 percent, the BER will be irreducible. This error for 64 and 256-QAM is 11 and 5 percent, respectively. Figure 14 illustrates BER of 16, 64, and 256-QAM schemes in permitted ranges of amplitude error. In continue, we consider phase errors. Like amplitude error, as phase error increases the

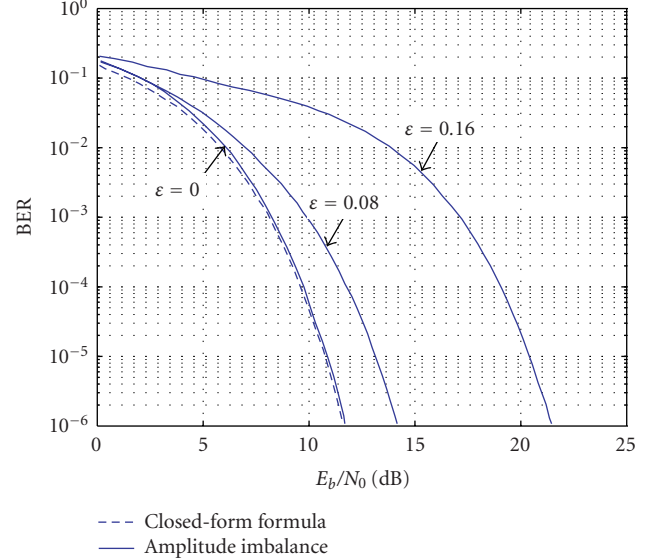


FIGURE 13: BER of the 16-QAM signal versus E_b/N_0 as a function of ε . From left to right $\varepsilon = 0, 0.08, 0.16$. Dashed line represents BER calculated-from the closed form formula.

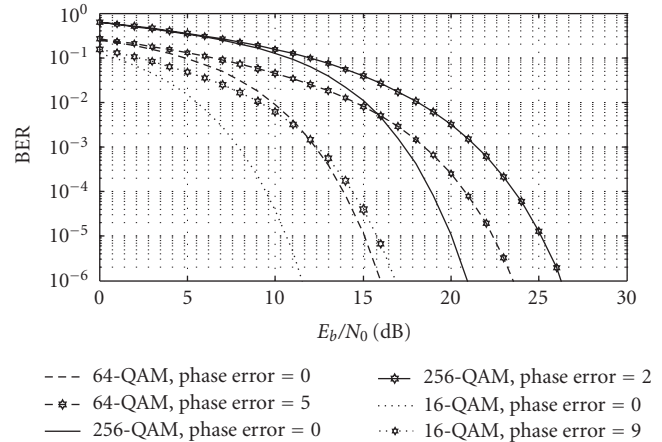


FIGURE 14: BER versus E_b/N_0 for 16, 64, 256-QAM in permitted ranges of amplitude error. From left to right: 16-QAM: $\varepsilon = 0, 0.12$, 64-QAM: $\varepsilon = 0, 0.03$, 256-QAM: $\varepsilon = 0, 0.014$.

amount of E_b/N_0 required to have BER of 10^{-6} increases. In 16-QAM modulation, if phase error in I and Q paths reaches 20 degree, the BER will be irreducible. This error for 64 and 256-QAM is 9 and 4 degrees, respectively. Figure 15 shows BER of 16, 64, and 256-QAM schemes in permitted ranges of phase error. So, in M -ary QAM, as M increases, the amount of permitted amplitude and phase errors reduces and the amount of BER increases.

5.2. BER calculations in presence of DC offsets

The unbalance effects in APDP created by mismatch in the IV characteristics of diodes causes DC offsets. If saturation currents i_s and slope parameters α are different for the two

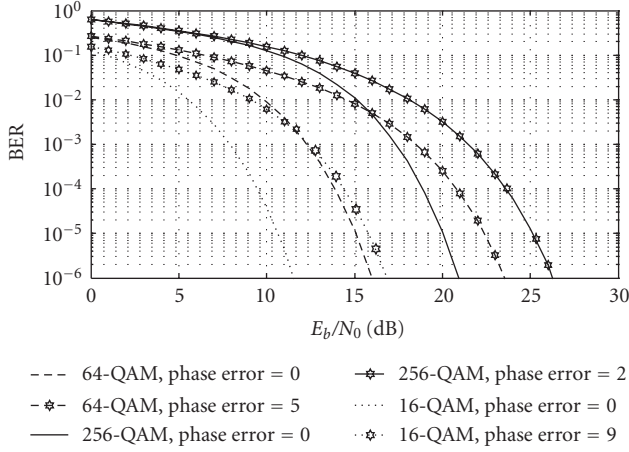


FIGURE 15: BER versus E_b/N_0 for 16, 64, 256-QAM in permitted ranges of phase error. From left to right: 16-QAM: $\theta = 0, 9$ degrees, 64-QAM: $\theta = 0, 5$ degrees, 256-QAM: $\theta = 0, 2$ degrees.

diodes of the APDP, we may assume that

$$\begin{aligned} i_{s1} &= i_s + \Delta i_s, & i_{s2} &= i_s - \Delta i_s, \\ \alpha_1 &= \alpha + \Delta \alpha, & \alpha_2 &= \alpha - \Delta \alpha. \end{aligned} \quad (11)$$

As we know from [4], the conductance expressions for i_s and α mismatches can be, respectively, written as follows:

$$\begin{aligned} g_{\Delta i_s} &= 2\alpha i_s \left[\cosh \alpha V + \frac{\Delta i_s}{i_s} \sinh \alpha V \right], \\ g_{\Delta \alpha} &= 2\alpha i_s e^{(\Delta \alpha)V} \left[\cosh \alpha V + \frac{\Delta \alpha}{\alpha} \sinh \alpha V \right]. \end{aligned} \quad (12)$$

Like in the previous section, we multiply these conductances to the applied voltage. The output current of the APDP has a DC offset that is equal to

$$\begin{aligned} i_{dc\text{-offset}} &= 2\alpha i_s V_{Lo} I_1(\Delta \alpha V_{Lo}) \times [I_0(\alpha V_{Lo}) + I_2(\alpha V_{Lo})] \\ &\quad \pm 2\alpha(\Delta i_s) V_{Lo} I_1(\alpha V_{Lo}). \end{aligned} \quad (13)$$

Current terms add constructively when one of the diodes has both a higher slope and higher saturation current. They add destructively otherwise. So the output currents in I and Q paths after a lowpass filter are equal to

$$\begin{aligned} \tilde{I} &= 2\alpha i_s \sqrt{\frac{2E_{min}}{T_s}} I_2(\alpha V_{Lo}) a_i + i_{dc\text{-offset}}, \\ \tilde{Q} &= 2\alpha i_s \sqrt{\frac{2E_{min}}{T_s}} I_2(\alpha V_{Lo}) b_i + i_{dc\text{-offset}}. \end{aligned} \quad (14)$$

$\Delta \alpha$ and Δi_s may be different in I and Q paths. So, the signal constellation is corrupted and the BER increases. In continue, we calculate the BER due to different levels of diode imbalances. As the mismatches increase, the amount of E_b/N_0 required to have BER of $10e-6$ increases. For example, in 16-QAM signal, we consider different cases of mismatch

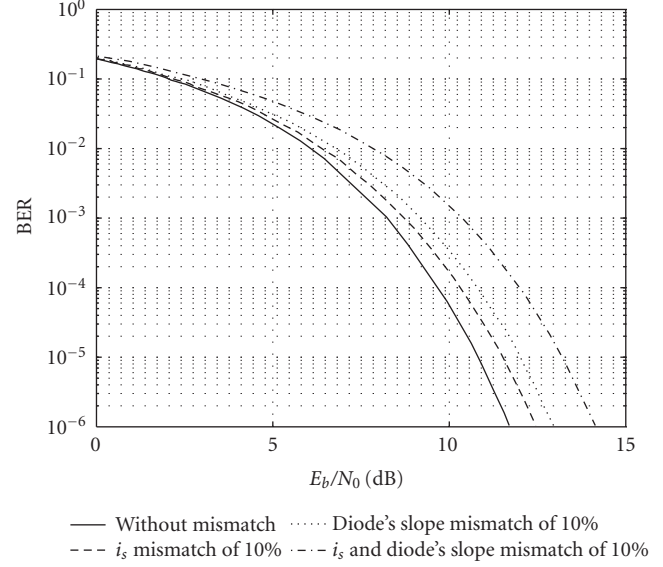


FIGURE 16: BER of 16-QAM signal for different levels of diodes mismatches. From left to right: without mismatch, i_s mismatch of 10%, α mismatch of 10%, both α and i_s mismatch of 10%.

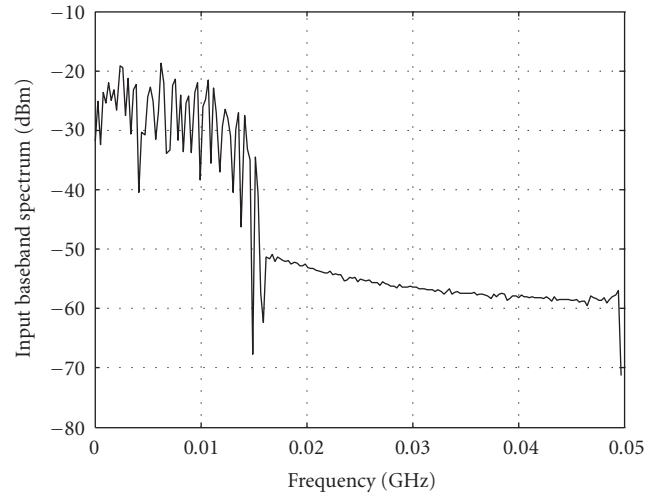


FIGURE 17: Input baseband signal spectrum.

that are shown in Figure 16. It can be seen that the effect of α mismatch on BER degradation is more than i_s mismatch [12].

6. COMMUNICATION LINK FOR 16-QAM SIGNAL

A communication link is constructed with the proposed modulator-demodulator. The link is simulated with baseband I and Q signals corresponding to 16-QAM modulation format with data rate 110 Mbps. We set the LO power to 10 dBm and its frequency to 14 GHz. Spectral response of input baseband signals is shown in Figure 17. Then, the modulated signal at the RF port of the modulator is sent to the demodulator input. The RF modulated signal spectrum

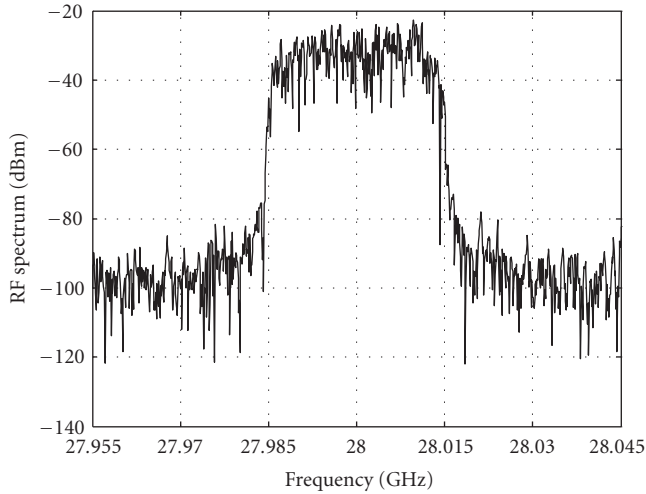


FIGURE 18: Output spectrum of the modulator at 28 GHz.

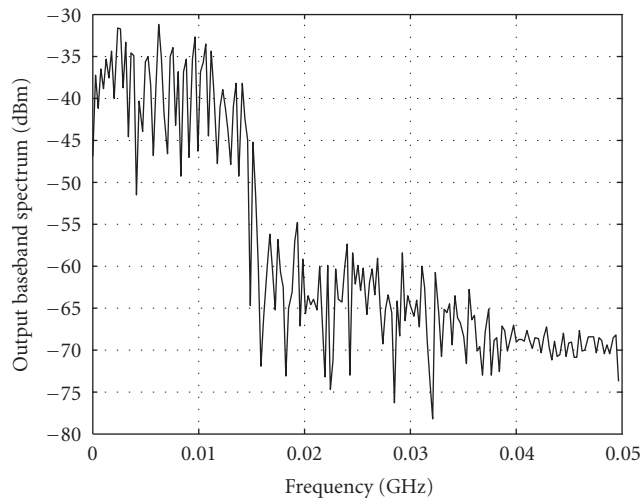


FIGURE 19: Output demodulated signal spectrum.

is depicted in Figure 18. As can be seen from this figure, the data rate of the system is 110 Mbps. Finally, the RF-modulated signal is demodulated with the LO signal. The output baseband signals are produced at the land demodulator's I and Q ports. Spectral response of these signals is drawn in Figure 19. As may be seen, the proposed structure efficiently transmits the modulated signal. In-phase and quadrature-phase signals at time domain are presented in Figures 20 and 21. The figures show a close agreement between input and output signals at time domain both in I and Q paths.

7. CONCLUSION

Direct conversion circuitry with even harmonic mixers based on antiparallel diode pair (APDP) was used to realize a Ka band even harmonic quadrature modulator-demodulator operating at 28 GHz. Self-biased APDP was used in order to

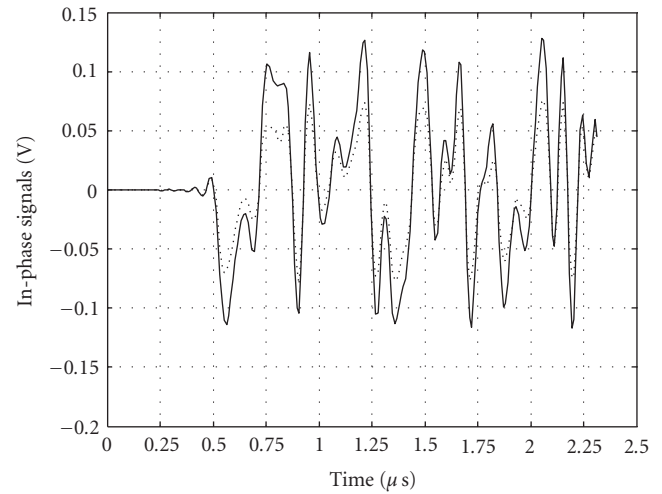


FIGURE 20: Input and output in-phase signals.

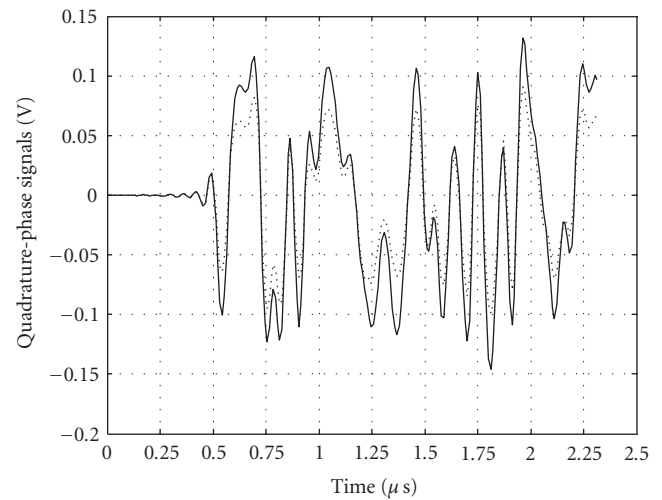


FIGURE 21: Input and output quadrature-phase signals.

flatten the conversion loss of the system versus LO power. The system structure is very attractive, because of reducing hardware complexity and cost. The impacts of I/Q imbalances and DC offsets on BER performance of the system was also considered. A communication link is built with the proposed modulator-demodulator. The experimental results show that this system can be a low-cost and high-performance 16-QAM transceiver for LMDS applications.

ACKNOWLEDGMENTS

The authors wish to thank the editor and the anonymous reviewers for their insightful comments and suggestions which greatly improved the presentation of this work. This work was supported in part by Iran Telecommunication Research Center (ITRC) and the Academic Research Section of Iran Management and Planning Organization (#102) under Contract 1721.

REFERENCES

- [1] M. Cohn, J. E. Degenford, and B. A. Newman, "Harmonic mixing with an antiparallel diode pair," *IEEE Transactions on Microwave Theory and Techniques*, vol. 23, no. 8, pp. 667–673, 1975.
- [2] K. Itoh, A. Iida, Y. Sasaki, and S. Urasaki, "A 40 GHz band monolithic even harmonic mixer with an antiparallel diode pair," in *Proceedings of IEEE MTT-S International Microwave Symposium Digest*, vol. 2, pp. 879–882, Boston, Mass, USA, June 1991.
- [3] M. R. Barber, "Noise figure and conversion loss of the schottky barrier diode," *IEEE Transactions on Microwave Theory and Techniques*, vol. 15, no. 11, pp. 629–635, 1967.
- [4] C. J. Verver, D. Drolet, M. G. Stubbs, and C. Pike, "Development of a Ka-band even harmonic modulator for a satellite briefcase terminal," in *Proceedings of Asia Pacific Microwave Conference (APMC '99)*, vol. 2, pp. 448–451, Singapore, November-December 1999.
- [5] M. W. Chapman and S. Raman, "A 60 GHz uniplanar MMIC 4X subharmonic mixer," in *Proceedings of IEEE MTT-S International Microwave Symposium Digest*, vol. 3, pp. 95–98, Phoenix, Ariz, USA, May 2001.
- [6] M. Shimozawa, T. Katsura, K. Maeda, et al., "An even harmonic mixer using self-biased anti-parallel diode pair," in *Proceedings of IEEE MTT-S International Microwave Symposium Digest*, vol. 1, pp. 253–256, Seattle, Wash, USA, June 2002.
- [7] P. Blount and C. Trantanella, "A high IP₃, subharmonically pumped mixer for LMDS applications," in *Proceedings of the 22nd Annual Gallium Arsenide Integrated Circuit (GaAs IC '00)*, pp. 171–174, Seattle, Wash, USA, November 2000.
- [8] J.-Y. Park, S.-S. Jeon, Y. Wang, and T. Itoh, "Integrated antenna with direct conversion circuitry for broad-band millimeter-wave communications," *IEEE Transactions on Microwave Theory and Techniques*, vol. 51, no. 5, pp. 1482–1488, 2003.
- [9] I. Telliez, A.-M. Couturier, C. Rumelhard, C. Versnaeyen, P. Champion, and D. Fayol, "A compact, monolithic microwave demodulator-modulator for 64-QAM digital radio links," *IEEE Transactions on Microwave Theory and Techniques*, vol. 39, no. 12, pp. 1947–1954, 1991.
- [10] P. J. Lee, "Computation of the bit error rate of coherent m-ary psk with gray code bit mapping," *IEEE Transactions on Communications*, vol. 34, no. 5, pp. 488–491, 1986.
- [11] L. Jianhua, K. B. Letaief, J. C.-I. Chuang, and M. L. Liou, "M-PSK and M-QAM BER computation using signal-space concepts," *IEEE Transactions on Communications*, vol. 47, no. 2, pp. 181–184, 1999.
- [12] F. Shayegh, A. Mohammadi, and A. Abdipour, "Characterization of EHM direct conversion transceivers in Ka-band," in *Proceedings of the 35th European Microwave Conference (EUMC '05)*, pp. 371–374, Paris, France, October 2005.

Research Article

V-Band Multiport Heterodyne Receiver for High-Speed Communication Systems

Serioja O. Tatu and Emilia Moldovan

*Institut National de la Recherche Scientifique, Énergie, Matériaux et Télécommunications (INRS-EMT),
800 de la Gauchetière Ouest, R 6900, Montréal, Canada H5A 1K6*

Received 20 April 2006; Revised 10 October 2006; Accepted 11 October 2006

Recommended by Kiyoshi Hamaguchi

A V-band receiver using a MHMIC multiport circuit is presented in this paper. The millimeterwave frequency conversion is performed using a passive circuit, the multiport, and related power detectors, avoiding the conventional millimeter-wave active costly mixers. Basically, the multiport circuit is an additive mixer in which the resulting sum of millimeter-wave signals is nonlinearly processed using millimeter-wave power detectors. This multiport heterodyne receiver is an excellent candidate for the future low-cost high-speed millimeter-wave wireless communication systems. The operating principle of the proposed heterodyne receiver and demodulation results of high-speed MPSK/QAM signals are presented and discussed in this paper. According to suggested datarate of 100–400 Mbps used to prove the operating principle, the IF of this receiver was chosen at 900 MHz. Therefore, this receiver is a possible alternative solution for WPAN applications

Copyright © 2007 S. O. Tatu and E. Moldovan. This is an open access article distributed under the Creative Commons Attribution License, which permits unrestricted use, distribution, and reproduction in any medium, provided the original work is properly cited.

1. INTRODUCTION

The modern communication receivers are more and more exigent in terms of wide-band, datarates, size, and costs [1]. The millimeter-wave technology has received increased attention in both academia and industry for very high-datarate wireless personal area network (WPAN) applications such as wireless data bus for cable replacement, high-speed wireless Internet access, wireless direct communication between notebooks and related devices, and wireless high-resolution TV and videoconferencing. The IEEE 802.15.3c industrial standard based on millimeter-wave technology has been recently introduced for WPAN.

The use of millimeter-wave frequencies enables the design of compact and low-cost wireless millimeter-wave communication front-ends, which can offer convenient terminal mobility and high-capacity channels. This wide range of applications requires low-cost equipment operating at hundreds of megabits per second. In the last decade initial research has been made, especially in terms of designing new millimeter wave components operating over the V-band [2–5].

In order to improve overall performances of the communication receivers, alternative wide-band architectures for

high-speed wireless communication systems have been explored in the past years [6–10].

This paper presents MPSK/QAM demodulation results of a V-band multiport heterodyne receiver suitable for very high-datarate WPAN applications.

2. THE MULTIPORT MIXER

The main purpose of this paper is to demonstrate that the multiport circuit together with related power detectors and two differential amplifiers can successfully replace a conventional mixer in a low-cost millimeter-wave heterodyne or homodyne architecture.

The multiport equivalent circuit of the heterodyne receiver uses four power detectors and two differential amplifiers operating at IF frequency. The multiport block diagram is shown in Figure 1. The circuit is composed of four 90° hybrid couplers and a 90° phase shifter.

Let us assume that there are two input normalized waves, a_5 from the LO and a_6 from the RF input, having different amplitudes and frequencies. The MPSK/QAM modulated signals can be expressed using the phase and the amplitude variation of the RF input signal, $\alpha(t)$ and $\varphi_6(t)$,

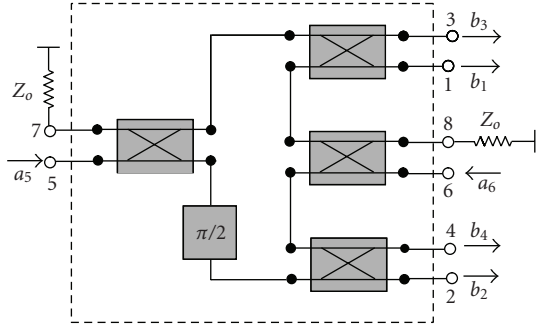


FIGURE 1: The multiport circuit block diagram.

respectively,

$$\begin{aligned} a_5 &= a \cdot \exp [j(\omega_0 \cdot t + \varphi_5)], \\ a_6 &= \alpha(t) \cdot a \cdot \exp [j(\omega \cdot t + \varphi_6(t))]. \end{aligned} \quad (1)$$

The output detected signals can be calculated based on the multiport block diagram and using the quadratic characteristic of the power detectors:

$$v_i(t) = K \cdot |b_i(t)|^2, \quad (2)$$

$$v_{1,3}(t) = K \frac{a^2}{4} \cdot \{1 + \alpha(t)^2 - / + 2 \cdot \alpha(t) \cdot \cos [-\Delta\omega \cdot t + \Delta\varphi(t)]\}, \quad (3)$$

$$v_{2,4}(t) = K \frac{a^2}{4} \cdot \{1 + \alpha(t)^2 - / + 2 \cdot \alpha(t) \cdot \sin [-\Delta\omega \cdot t + \Delta\varphi(t)]\}. \quad (4)$$

In the previous equation, $\Delta\omega = \omega_0 - \omega$ represents the frequency difference between the multiport inputs (superheterodyne), and $\Delta\varphi(t) = \varphi_6(t) - \varphi_5$ is the phase difference between the same signals.

Considering the sinusoidal antiphase signals in each equation (3) or (4), the DC offset is eliminated using a differential approach. Therefore the output I/Q signals are

$$\begin{aligned} i(t) &= v_3(t) - v_1(t) = K \cdot \alpha(t) \cdot |a|^2 \cdot \cos [-\Delta\omega \cdot t + \Delta\varphi(t)], \\ q(t) &= v_4(t) - v_2(t) = K \cdot \alpha(t) \cdot |a|^2 \cdot \sin [-\Delta\omega \cdot t + \Delta\varphi(t)]. \end{aligned} \quad (5)$$

The previous equations show that the multiport circuit with four power detectors and two differential amplifiers can successfully replace a conventional mixer.

Therefore the equivalence between the conventional I/Q mixer architecture and the multiport mixer, as presented in Figure 2, has been demonstrated.

It must be noted that conventional superheterodyne approach using a down-converter does not have a direct equivalence with the proposed multiport approach. This conventional receiver can be implemented using a V-band down-converter mixer (a balun and two Schottky diodes, e.g.) and a IF I/Q mixer.

In practice, for a multiport heterodyne receiver, the carrier frequency ω is close to the local oscillator frequency ω_0 .

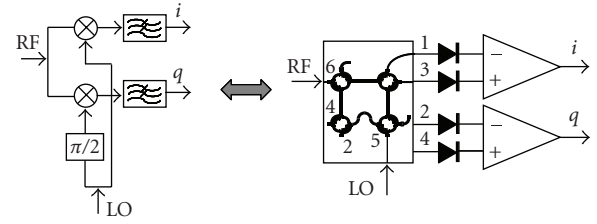


FIGURE 2: Equivalence between the conventional I/Q mixer and the multiport mixer.

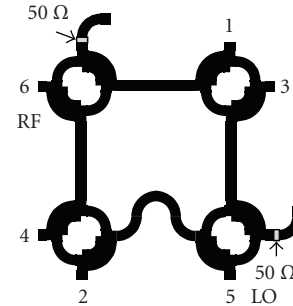


FIGURE 3: Layout of the V-band multiport circuit.

Therefore, these receivers are low IF heterodyne receivers. However, if $\omega_0 = \omega$, I/Q direct conversion is obtained in a homodyne architecture. This aspect can be considered as an important advantage of the proposed receiver compared to the conventional V-band down-conversion receiver. The same multiport front-end can be used for both heterodyne and homodyne architectures. In addition, signal to noise ratio is improved using a multiport circuit. The cost of additional hybrids and two Schottky diodes is compensated by the reduced cost of the IF stage (IF mixers instead of the conventional IF I/Q mixer).

A V-band multiport circuit was designed in MHEM technology using a $125 \mu\text{m}$ ceramic substrate having a relative permittivity of 9.9. Figure 3 shows the layout of the circuit having a size of approximately 3 mm by 3 mm. The circuit is composed of four 90° hybrid couplers connected by 50Ω microstrip transmission lines. In order to avoid reflections at the two unused ports of the multiport circuit, two 50Ω loads are connected to open circuited quarter-wave transmission lines (virtual RF short-circuits). The hybrid coupler connected to LO port together with the 90° phase shifter (made using an additional quarter-wave transmission line on a curved branch) is equivalent to an in-phase 3 dB power divider. The circuit was optimized to operate at the 60 GHz central frequency using ADS Momentum software.

In order to obtain the four output detected signals, as expressed by (3) and (4), power detectors, composed of Schottky diodes with related matching networks, must be connected at multiport outputs. The I/Q IF signals of the proposed V-band mixer will be finally obtained using two differential amplifiers.

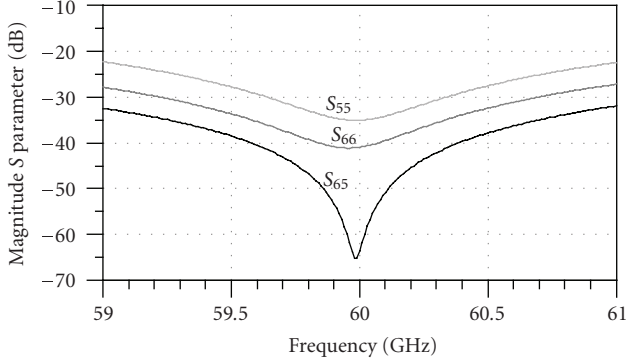


FIGURE 4: Simulation results of the return loss and isolation at RF inputs.

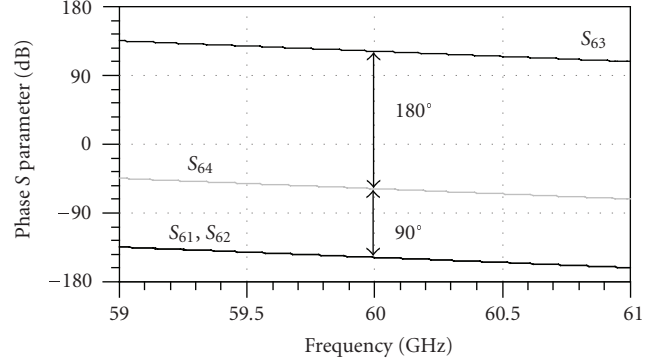


FIGURE 6: Simulation results of the transmission S parameter phase corresponding to the RF input.

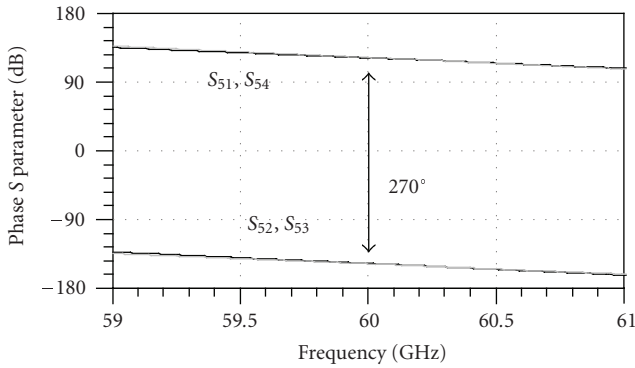


FIGURE 5: Simulation results of the transmission S parameter phase corresponding to the LO input.

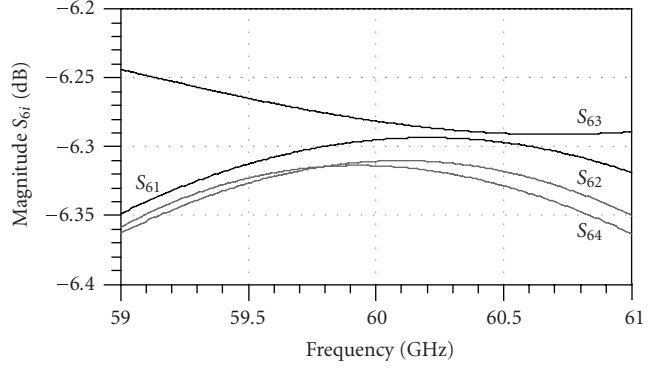


FIGURE 7: Simulation results of S_{6i} magnitudes at RF input.

Figure 4 shows simulation results of S parameters at RF input ports of the proposed multipoint circuit. Excellent return losses and isolation between RF inputs were obtained in a 2 GHz frequency band centered at the 60 GHz operating frequency (return loss less than 20 dB).

The phase and the magnitude of the transmission S parameters are also of main interest to obtain the requested four “ q_i points” of the multipoint circuit (see the block diagram of Figure 1). Figures 5 and 6 show the phase of transmission scattering parameters between inputs and outputs versus the frequency. The phases of these parameters are shifted by 90° multiples over the frequency band, as suggested in the block diagram.

As suggested in previous figures, the use of the V-band couplers allows 90° phase difference over a very wide band, suitable for a high-quality I/Q mixer.

Figure 7 shows the magnitude of transmission S parameters between the RF input port and the four outputs. Compared to the ideal multipoint model, a supplementary loss of around 0.3 dB appears at the central frequency. Similar results related to the magnitude of transmission S parameters between the LO input port and the four outputs are also obtained.

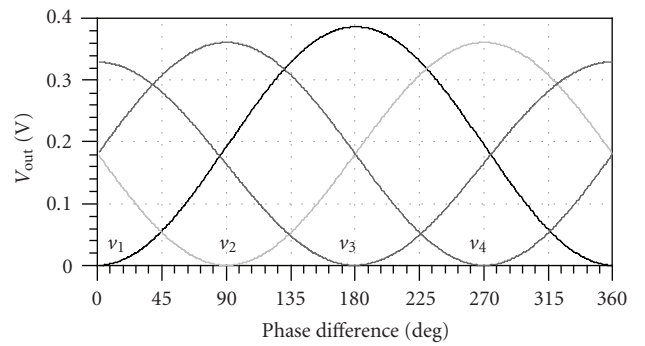


FIGURE 8: Simulation results of V_{out} versus inputs phase difference.

In order to demonstrate that the multipoint is a four “ q_i -point” circuit having all points spaced by 90° , a harmonic balance simulation was performed at 60 GHz using a multipoint model based on ADS momentum S parameter results. Power detectors were connected at the four outputs. The phase difference between millimeter-wave inputs was swept in a 360° range and the RF input signal power was set to 0 dBm. The multipoint output detected voltages versus the phase difference are shown in Figure 8.

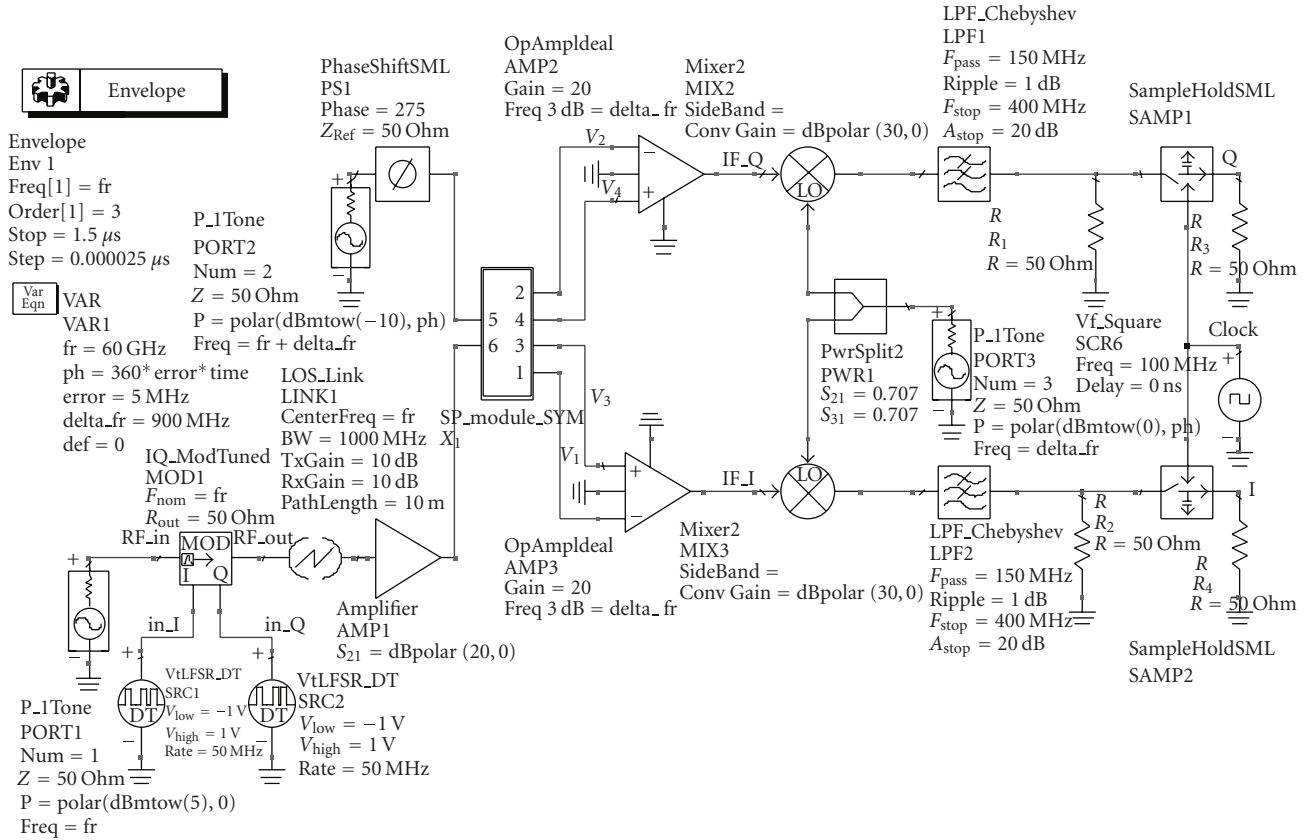


FIGURE 9: ADS simulation block diagram of the multiport heterodyne receiver.

As seen, the output voltage minimum values are shifted by 90° multiples as requested for this multiport architecture. In addition, the output voltages at ports 1 and 3 and at ports 2 and 4, respectively, are in antiphase, as demonstrated in the theoretical part (see (3) and (4)). Therefore I/Q output signals can be obtained according to (5) using two differential amplifiers.

3. DEMODULATION RESULTS

Demodulation results of the V-band multiport heterodyne receiver are presented in this section.

The multiport heterodyne receiver simulation block diagram, using ADS software, is presented in Figure 9. Simulations are performed using a 60 GHz carrier frequency of a MPSK/QAM modulated signal. According to the proposed datarate of 100–400 Mbps, the IF of the heterodyne receiver was chosen at 900 MHz. The second frequency conversion using conventional mixers is also implemented.

As presented in the same figure, the proposed multiport heterodyne receiver is composed, as usually, of RF, IF, and baseband stages. The V-band RF front-end contains the low-noise amplifier AMP1 and the V-band I/Q mixer (the V-band multiport module including four power detectors).

Excluding the IF differential amplifiers (AMP2 and AMP3), the IF and baseband stages have a conventional architecture: IF down-converters (MIX2, MIX3, LPF1, and

LPF2) and sample-and-hold circuits (SAMP1 and SAMP2). Baseband amplifiers can be used to improve the overall gain of the receiver.

In order to obtain the signal waveforms or spectrums, an ADS envelope simulation at the operating frequency of 60 GHz is performed using the simulation diagram of Figure 9. In this diagram a 100 Mbps QPSK pseudorandom signal is generated at the transmitter using two generators connected to the I/Q modulator.

Various MPSK/QAM modulations will be also analyzed in this work using the ADS vector modulator model. It is noted that a loss-link model based on Friis equation is used to simulate the free-space signal propagation.

Figure 10 shows the typical IF spectrum (IF_I or IF_Q signals) using the proposed architecture and the same QPSK signal of 100 Mbps. As well known, and as this spectrum suggested, a 400 Mbps QPSK signal can be demodulated using the same IF of 900 MHz. However, the bandwidth of the IF stage must be increased according to the new datarate.

The same architecture can also meet all high-speed requirements of the IEEE 802.15.3c wireless standard using an increased IF. For this purpose, the IF differential amplifiers based on operational amplifiers must be replaced by differential amplifiers using microwave transistors.

Figure 11 shows a typical spectrum of a baseband quadrature signal (I or Q) obtained after the second down-conversion and the sample-and-hold circuit (SHC). We note

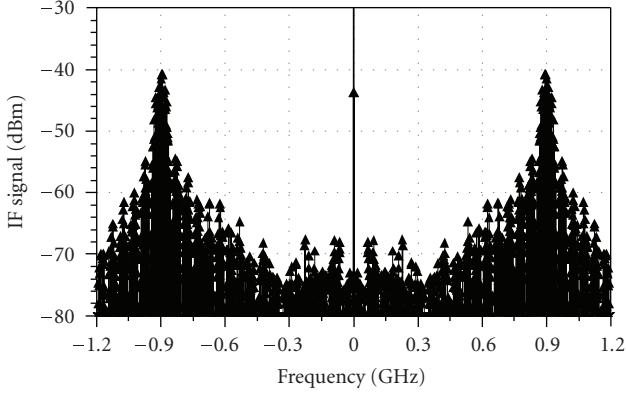


FIGURE 10: Typical spectrum of the IF signal.

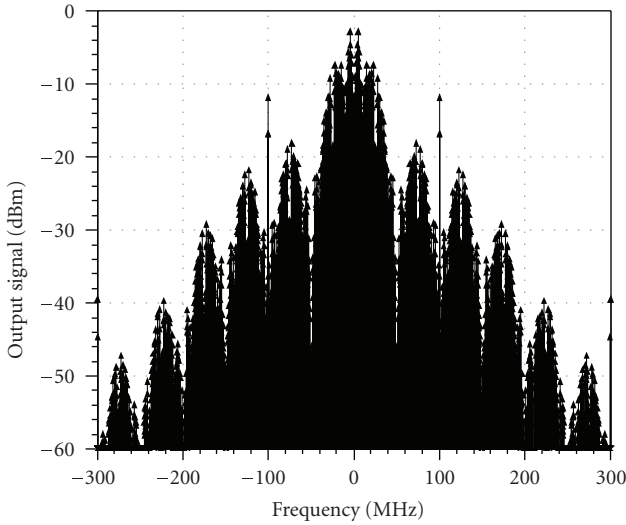


FIGURE 11: Typical spectrum of a baseband quadrature signal.

that the spectral lines of ± 100 MHz represent the clock signal of the SHC.

A pseudorandom bit sequence of 700 nanoseconds is represented in Figure 12. As seen, the demodulated output signals have the same bit sequence as those generated by the transmitter. The gray line corresponds to the baseband signal before the sample-and-hold circuit which dramatically improves the demodulated signal shape.

The demodulation results demonstrate the validity of the proposed heterodyne architecture. Bit error rate (BER) analysis is also performed in this work using an appropriated length pseudorandom bit-stream.

Figure 13 shows all possible 16 states of the I/Q output signals corresponding to a 16 QAM modulation. As seen, each signal has four different levels corresponding to the signal constellation. These levels are quasi-equidistant and symmetrical versus the zero voltage level. The gray line has the same signification as in the previous figure. Therefore, the SHC improves the demodulation results, as expected.

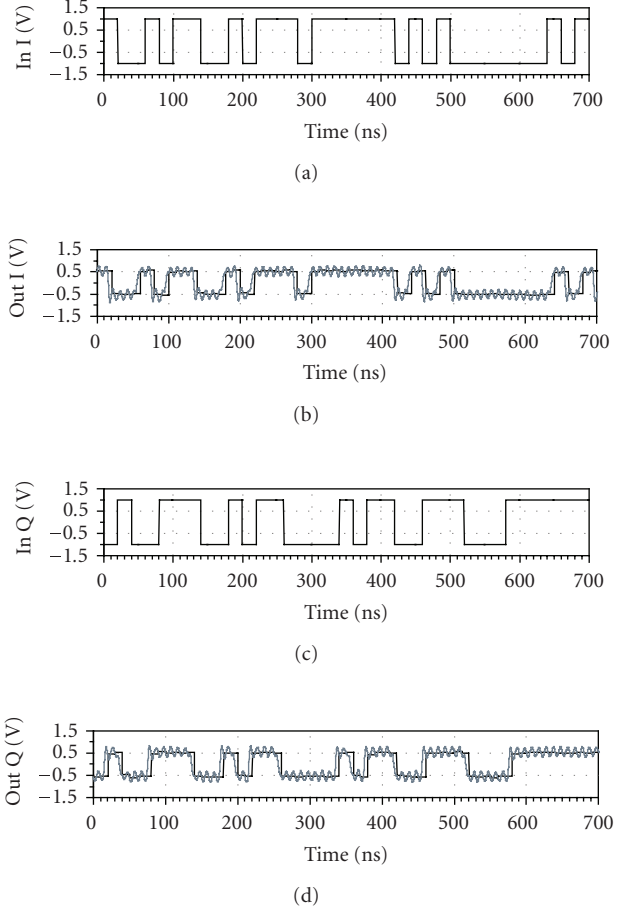


FIGURE 12: Demodulation results of 100 Mb/s QPSK pseudorandom bit sequence.

Supposing a perfect synchronism and no additional noise, Figure 14 shows various simulation results of demodulated constellations using the proposed heterodyne architecture for high-speed MPSK/QAM signals: 100 Mbps for QPSK, 200 Mbps for 8PSK and 16 QAM, and 400 Mbps for 16PSK.

As seen, all clusters of demodulated constellations are very well positioned and individualized. Due to the differential approach and the multiport design, the DC offset represented by the distance between the central point and the origin is almost zero.

Figure 15 shows the demodulation results of a 16 QAM signal for a low signal to noise ratio of 5 dB (a white noise was added in the transmission path). Simulation results show that all clusters remain well individualized and well positioned in the I/Q complex plan. Furthermore, signal processing techniques will allow to obtain improved demodulation results.

As known, a millimeter-wave oscillator does not have excellent frequency stability and is difficult to be controlled. If the difference between the carrier and the local oscillator is not exactly equal to IF, the demodulated constellation turns clockwise or anti-clockwise, depending on the sign of this

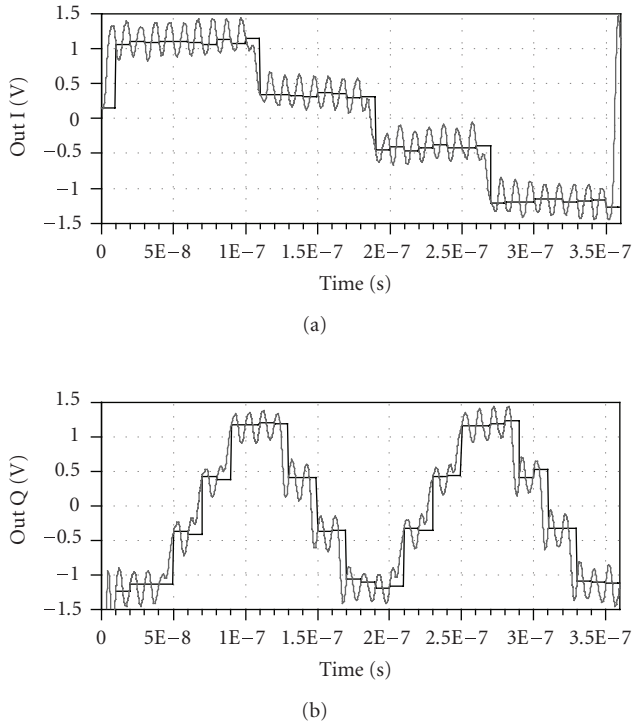


FIGURE 13: Demodulation results of 16 QAM signal.

difference [9]. Figure 16 shows a 16 QAM constellation in the case of 45° phase error of synchronism of the millimeter-wave oscillator. However, these frequency/phase errors can be successfully compensated using signal processing techniques. The second LO must be dynamically adjusted by a control loop.

Figure 17 shows the BER versus the energy per bit to the spectral noise density (E_b/N_0) for various millimeter-wave LO frequency errors (no error, 5 MHz, and 25 MHz, resp.). The frequency/phase error compensation technique of the second LO in the case of a 100 Mbps QPSK modulated signal is used. Simulation shows an excellent result for the proposed receiver. The BER is less than 10^{-6} for an E_b/N_0 ratio of 12 dB, considering the specified frequency errors of synchronism of the millimeter-wave oscillator.

The heterodyne architecture will allow an increased gain of the receiver for relatively high range applications compared to the homodyne architecture. Simulation results show more than 70 dB of the multiport heterodyne receiver overall gain, compared to 50 dB of gain, reported for the homodyne receivers [6, 7].

4. CONCLUSIONS

Simulation results of a V-band millimeter-wave multiport heterodyne receiver have been presented in this paper. The millimeter-wave frequency conversion is obtained using the specific properties of the multiport circuit, avoiding the use of a costly conventional active mixer.

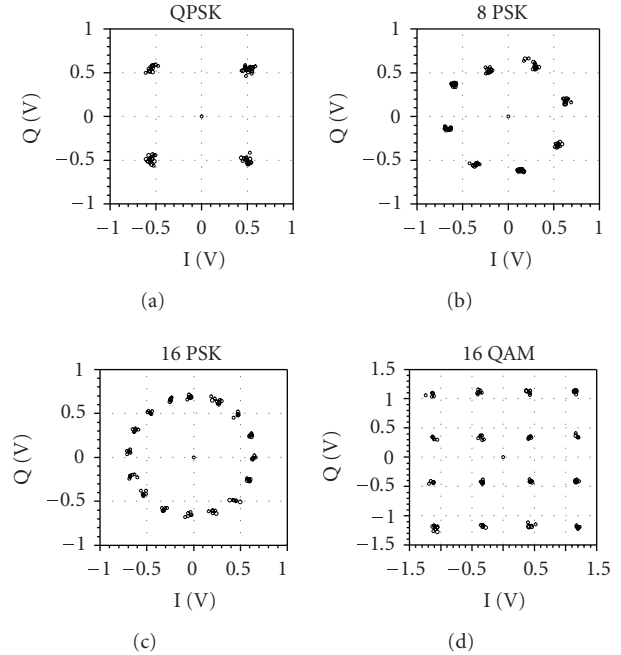


FIGURE 14: Demodulated high-speed MPSK/QAM signals.

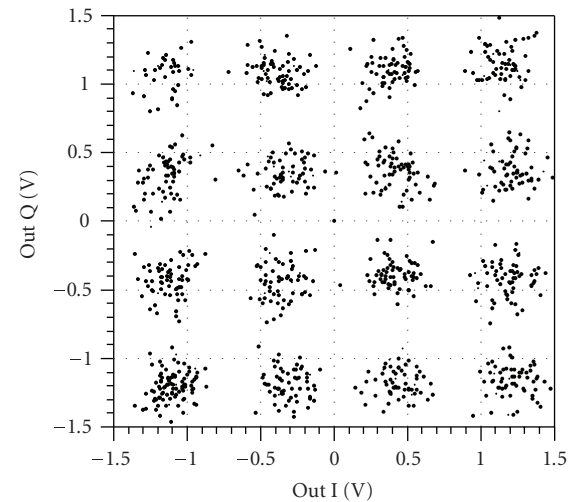


FIGURE 15: Constellation of demodulated 16 QAM signal in presence of a white noise.

Excellent demodulation results were obtained using high-speed V-band MPSK/QAM modulated signals. Simulated BER results, in the case of an important millimeter-wave LO frequency error from synchronism (dynamically compensated using the second LO), are excellent. Compared to the direct conversion, due to the heterodyne architecture, an improved overall gain was obtained.

The proposed multiport heterodyne architecture enables the design of compact and low-cost wireless millimeter-wave communication receivers for future high-speed wireless communication systems, according to the IEEE 802.15.3c wireless standard.

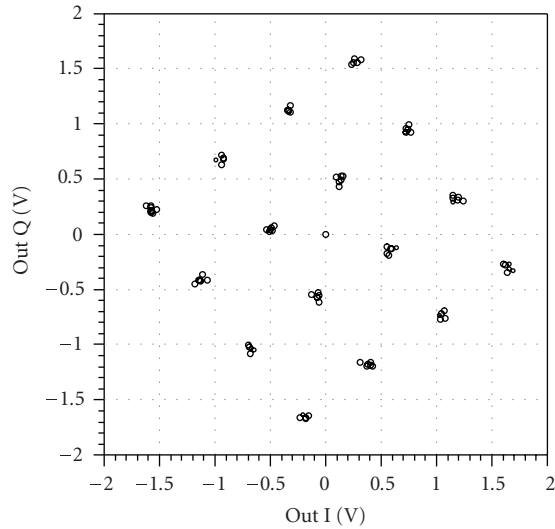


FIGURE 16: Constellation of demodulated 16 QAM signal in the case of 45° phase error of synchronism.

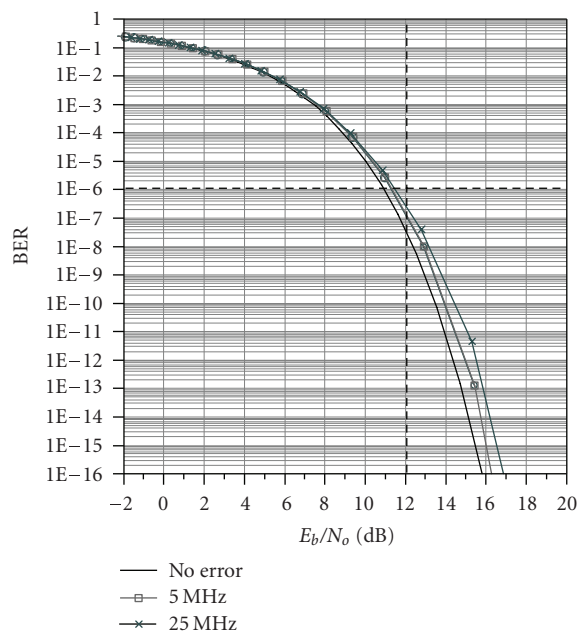


FIGURE 17: BER simulation results for various errors of synchronism of the millimeter-wave oscillator.

ACKNOWLEDGMENT

The financial support of the National Science Engineering Research Council (NSERC) of Canada is gratefully acknowledged.

REFERENCES

[1] P. Smulders, "Exploiting the 60 GHz band for local wireless multimedia access: prospects and future directions," *IEEE Communications Magazine*, vol. 40, no. 1, pp. 140–147, 2002.

- [2] J. Wenger and J. Splettstoesser, "Ka- and V-band MMIC components for personal communication networks," in *Proceedings of IEEE MTT-S International Microwave Symposium Digest*, vol. 2, pp. 491–494, San Francisco, Calif, USA, June 1996.
- [3] A. Nestic, I. Radnovic, and V. Brankovic, "Ultra-wide band printed antenna array for 60 GHz frequency range," in *Proceedings of IEEE Antennas and Propagation Society International Symposium Digest*, vol. 2, pp. 1272–1275, Montreal, Quebec, Canada, July 1997.
- [4] K. S. Ang, M. Chongcheawchamnan, and I. D. Robertson, "Monolithic resistive mixers for 60 GHz direct conversion receivers," in *Proceedings of IEEE Radio Frequency Integrated Circuits Symposium, Digest of Papers (RFIC '00)*, pp. 35–38, Boston, Mass, USA, June 2000.
- [5] T. Brabetz and V. Fusco, "Six-port receiver MMIC for V-band MBS applications," in *Proceedings of the 11th Gallium Arsenide Applications Symposium (GAAS '03)*, pp. 97–99, Munich, Germany, October 2003.
- [6] S. O. Tatu, E. Moldovan, K. Wu, and R. G. Bosisio, "A new direct millimeter-wave six-port receiver," *IEEE Transactions on Microwave Theory and Techniques*, vol. 49, no. 12, pp. 2517–2522, 2001.
- [7] S. O. Tatu, E. Moldovan, G. Brehm, K. Wu, and R. G. Bosisio, "Ka-band direct digital receiver," *IEEE Transactions on Microwave Theory and Techniques*, vol. 50, no. 11, pp. 2436–2442, 2002.
- [8] S. O. Tatu, E. Moldovan, K. Wu, R. G. Bosisio, and T. A. Denidni, "Ka-band analog front-end for software-defined direct conversion receiver," *IEEE Transactions on Microwave Theory and Techniques*, vol. 53, no. 9, pp. 2768–2776, 2005.
- [9] S. O. Tatu and T. A. Denidni, "Millimeter-wave six-port heterodyne receiver concept," in *Proceedings of IEEE Microwave Theory and Techniques Symposium Digest*, pp. 1999–2002, San Francisco, Calif, USA, June 2006, Conference CD, IEEE Catalogue Number 06CH37734C.
- [10] S. O. Tatu and E. Moldovan, "Alternative millimeter-wave communication receivers in six-port technology," in *Proceedings of Canadian Conference on Electrical and Computer Engineering (CCECE '06)*, Ottawa, Canada, May 2006.